Ride and Handling Analysis of an Urban Bus with Variable Tires Pressure

Mohammed Khair Al-Solihat

A Thesis

in

The Department

of

Mechanical and Industrial Engineering

Presented in Partial Fulfillment of the Requirements

for the Degree of Master of Applied Science (mechanical engineering) at

Concordia University

Montreal, Quebec, Canada

November, 2008

Your file Votre référence
ISBN: 978-0-494-63218-5
Our file Notre référence
ISBN: 978-0-494-63218-5

ABSTRACT

Ride and Handling Analysis of an Urban Bus with Variable Tires Pressure

Mohammed Khair Al-Solihat

The ride, handling and dynamic pavement loading properties of road vehicles are strongly influenced by the tire pressure. Although the central tire inflation systems (CTIS) have been implemented in many road and off-road vehicles, the assessments of variable tire pressure have been limited to field measurements in the context of ride and dynamic tire loads transmitted to the pavement. This dissertation research explored the role of variable tire pressure on the ride, pavement loading and handling dynamic characteristics through development and analysis of comprehensive three-dimensional models of an urban bus. The ride dynamic model was formulated based on nonlinear component models derived from the laboratory measured data, including the two-degrees-of-freedom driver-seat-suspension model. Considering that the passengers' load in an urban bus could vary from nearly none to the full passenger load, a tire pressure scheme in accordance with the passenger load was formulated and integrated in the model. The ride and dynamic pavement load properties of the vehicle were evaluated under random road roughness excitations corresponding to different tire pressures and passengers' loads. The influences of forward speed and road roughness conditions were also investigated. The results suggest that the use of nominal tire pressure under light passengers load would be detrimental to the ride vibration transmitted to the driver and the passengers, dynamic forces transmitted to the pavement and the forces transmitted to

the chassis structure. A variable tire pressure in accordance with the load would thus be highly beneficial, provided that the tire deflection is controlled to reduce the tire wear and heat buildup.

The limited available tire data on the cornering properties as a function of the pressure were analyzed to propose a regression-based tire cornering force model in conjunction with the widely used Magic tire formula. Two- and three-dimensional handling dynamic models of the vehicle were developed and analyzed to investigate the influence of tire pressure on steady-state and transient directional performance of the vehicle. The responses of the two models revealed reasonably good agreements in the steady-state handling, while the three-dimensional model accounted for the vehicle roll motion, which was observed to be considerably larger under lower tire pressures. The directional responses attained under different steering inputs and forward speeds suggested that a lower tire pressure increased the vehicle roll motions slightly due to reduced effective roll stiffness, while the high inflation pressure revealed greater oversteer tendency at higher tire pressures.

Acknowledgments

I am sincerely grateful to my supervisors, Dr. S. Rakheja and Dr. A. K. W. Ahmed for their constant guidance and support throughout my thesis work. This work was initially supported by Transportation Development center of Transport Canada and RTL Longueuil.

Special thanks also to all of my colleagues and friends for their help and cooperation. Last but not least I would like to thank my parents who have been encouraging and supporting me my whole life.

Table of Contents

List of Figures

List of Tables

CHAPTER 1

Introduction and Objective of Study

1.1 Introduction

Central tire inflation systems (CTIS) offer vehicle operations with variable tire pressure in response of changing speed and pavement surface conditions to achieve desired mobility performance with reduced pavement contact stresses. Such systems have been widely employed in military vehicles for enhancement of mobility over different terrains, and forestry products transport vehicles for preservation of unpaved roads [41]. A CTIS system offers considerable potential for: (*i*) improving vehicle ride performance over rough terrains by reducing the tire pressure and thus the tire stiffness; (*ii*) improved pavement load performance by distributing the tire loads over a greater contact area; (*iii*) improved operating efficiency by minimizing the unscheduled interruptions caused by tire leaks; (*iv*) possibly improved handling by ensuring identical pressure in all the vehicle tires; and (*v*) uniform tire wear. In recent years, such systems are increasingly being applied in highway freight and passenger transport vehicles.

Variation in tire pressure strongly influences nearly all the performance measures of road as well as off-road vehicles. The effective stiffness of tires in lateral, roll and vertical modes is directly related to the inflation pressure, which determines the handling roll stability and ride performances. A lower tire pressure can yield greater isolation of road-induced vibration and reduced road stresses but may also affect the cornering force in an adverse manner.

A number of concerns related to safety dynamic performance of CTIS systems have thus been expressed when vehicles operate with low pressure tires. These relate to: tire failures due to rapid overheating and wear of tires; increased rolling resistance and thus reduced fuel efficiency; adverse effects on handling performance and roll stability. The performance potentials of CTIS systems have been mostly evaluated through field measurements of ride vibration and tire force responses in agricultural, military and forestry vehicles [41]. The handling properties of vehicles operating with variable or lower tire pressure have not been evaluated. Moreover only minimal efforts have been made to develop simulation or analytical models to establish the performance characteristics of a CTIS system or to identify the optimal tire pressure for the ranges of vehicle speed and road roughness.

Urban buses operate with wide variations in passenger load and speeds on roads with varying surface roughness. A survey of number of passengers using city buses on different routes in Montreal and Longueuil regions has shown that buses mostly operate with only a few passengers, while they tend to be fully loaded over the short rush periods [1]. Moreover, their operation on city roads with greater surface roughness and abrupt irregularities causes comprehensive magnitudes of whole-body vibration to the passengers and the driver [1,5]. Considering the extreme variations in passengers loads and road roughness, the use of a variable tire pressure system in city buses could be beneficial. A CTIS system could help achieve desired controlled pressure depending on the passengers load, operating speed and road roughness. A recent study has conducted road measurements to assess the feasibility of a CTIS system for urban buses. It was shown that the low tire pressure is beneficial for enhancing shock and vibration ride

environment of vehicle, while the subjective judgments revealed negligible effect on handling [5].

The variations in tires pressure affect ride tire loads and handling performance of a vehicle in a highly complex and coupled manner. In this dissertation research, the influences of variations in the tire pressures of an urban bus on the dynamic ride, pavement loading and handling performances are systematically investigated through formulations and analyses of analytical models of the vehicle and its components. The analyses are performed for a wide range of variations in the passengers' load and road roughness. The results are used to identify optimal tires pressures as a function of the operating load.

1.2 Literature Review

An analytical study on the role of tire pressure on the vehicle performances involves thorough understanding of the vehicle components, particularly the tires and suspension and ride and handling dynamics analyses. The reported relevant studies are thus reviewed to build the essential knowledge and scope of the study. The reviewed studies grouped under relevant topics are briefly summarized below.

1.2.1 VERTICAL AND CORNERING PROPERTIES OF TIRES

The properties of tires, particularly the tire stiffness, are known to strongly influence all the performances of a vehicle. Identifying the effect of operating conditions on the tire stiffness properties and relating the effects of such conditions to the inflation pressures is an essential and challenging task. The dynamic behavior of vehicles is predominantly influenced by the tire dynamic properties, which are mainly represented

by cornering, braking and tractive characteristics. In addition, tire vertical stiffness and damping properties influence vehicle vibration characteristics and ride behavior. The tire dynamic properties, being characterized by forces and moments acting at the contact patch between the tire and the road surface result from tire deformations, which are functions of tire elastic properties and the tire-road interface adhesion [1].

Lateral deformations are produced by side-slip angle and/or inclination angle of the tire-wheel assembly. At small values of lateral slip, the tire dynamic characteristics are almost exclusively dependent on tire elastic properties and are nearly independent of tire–road friction. With increasing values of lateral slip, the contribution of elastic deformation decreases, while that of the tire–road friction increases. At large slip angles approaching the limits of tire performance, the tire–road friction becomes the major factor in determining the tire dynamic properties [6,13]. The dynamic characteristics of some tires have been mostly studied through laboratory and road tests, although some analytical models have been developed, which describe the tire dynamic properties in terms of tire deformation and tire elastic properties [1,2,12]. The vertical properties of tires are generally evaluated through measurement of static wheel-load deflection characteristics–which may not adequately describe the dynamic properties [14]. The rolling dynamic stiffness is usually determined by measuring the response of a rolling tire to a known harmonic excitation. Alternatively the dynamic vertical stiffness and damping properties of tires are derived from measurements of vibration transmission properties of tires on a rolling drum or a moving belt [6,15]. Although considerable attempts have been made to establish a definite relationship between the static and dynamic stiffness of tires, the findings seems to be contradictory. A few studies suggest

that the rolling dynamic stiffness of car tires may be 10–15% less than the static stiffness [6]. Other studies on heavy truck tires have established that the dynamic stiffness is approximately 5% less than the respective static value [6].

A number of regression-based models have been proposed to relate cornering and braking properties of tires to normal load, side-slip angle and slip ratio [6,21]. The 'magic formula' tire model, proposed by Pacejka et al. [21] is most widely used in vehicle dynamic studies. Earlier studies have formulated tire models by considering the tire tread as an elastic band [6]. Hewson [2] proposed a simple mathematical tire model for estimating the tire cornering stiffness, assuming negligible stiffness due to soft sidewalls. It has been suggested that the results predicted using this model is likely to be within 30 percent of the actual measured data [2].

The vertical, traction/braking and cornering properties of tires are greatly influenced by inflation pressure, apart from many other design factors. The role of inflation pressure, however has received relatively less attention particularly for heavy vehicle tires. Considering the evolutions in wide ranges of tires and the drive to operate vehicles with relative high pressure tires, the effects of tire pressure on the tire properties have been explored in a number of studies in the recent years. Kasprzak et al. [16] described the influences of inflation pressure on the lateral force and aligning torque through measurements of a racing car tire. The study showed that a lower inflation pressure could increase the lateral force capability of the tire under normal loads, while an opposite effect was observed under higher loads. Schmeitz et al. [18] investigated the influence of inflation pressure on the force and moment characteristics of five different passenger car tires of sizes ranging from 155/70 R13 to 225/55 R16. The study measured

pure lateral and longitudinal slip characteristics under four vertical loads and three different inflation pressures. The study concluded that a higher inflation pressure yields lower cornering stiffness under light normal loads but higher cornering stiffness under higher vertical loads as reported in study [16,17]. These effects where further incorporated in the analytical model of the tires. An increase in inflation pressure will also lead to higher carcass stiffness, leading to relatively lower side-slip angle experienced by the contact patch. Under light loads, the carcass side-slip is most likely attributed to relatively small deflection of the tread, which causes the lateral force to decrease. Under higher loads, the side-slip deformation is augmented by the deformation of the tread that most likely contributes to greater lateral force.

The vertical stiffness properties of tires have also been reported under different inflation pressure and normal loads [30]. These clearly illustrate increase in vertical stiffness of tires with increasing inflation pressure, which is mostly attributed to higher carcass stiffness. A regression model of the static truck tire stiffness has been proposed as a function of the normal load and inflation pressure on the basis of the reported measured data [1]. The braking/traction or longitudinal properties of tires are also dependent on the inflation pressure, although only minimal efforts have been made to characterize such properties as function of inflation pressure. The effect of inflation pressure changes on the slip deformation and peak friction coefficient has been experimentally investigated [30].

A few studies have further described the effects of variations in inflation pressure on the physical properties of tires. A change in inflation pressure tends to alter the size, shape and contact pressure distribution in the footprint of the tire and tire-road adhesion.

A higher inflation pressure will cause the size of the footprint to shrink leading to concentration of higher contact pressure near the center of the footprint and less tire distortion [16,17]. Furthermore, the distribution of contact stresses at the tire-road interface changes significantly with the inflation pressure [11]. Depending on the deformability of the ground, the changes in inflation pressure also affect the rolling resistance of the tire [6]. On hard surfaces, the rolling resistance generally decreases with an increase in the inflation pressure [6]. On soft deformable terrains, high inflation pressure would cause high sinkage of tire in soil and would thus lead to poor mobility [11]. The studies seem to suggest somewhat moderate effect of inflation pressure on the cornering properties of a tire. In general, the cornering stiffness of tires increases with an increase in the inflation pressure.

1.2.2 DYNAMIC WHEEL LOADS AND ROAD DAMAGE POTENTIAL

Heavy freight and passenger vehicles transmit higher dynamic loads to the highways, urban roads and bridge structures leading to their rapid deterioration. The magnitudes of dynamic wheel loads and stresses tend to be significantly higher than the static loads, and depend upon many factors, including vehicle weight and dimensions, axle loads, suspension and tire properties, road roughness, speed, etc. [5]. The magnitudes of dynamic tire loads distributed over pavement are strongly influenced by the tire inflation pressure. A higher inflation pressure imposes greater compressive pavement stress due to lower contact area, while a lower contact pressure may impose greater shearing at the pavement [11]. The dynamic tire loads transmitted to the pavement further depend on the dynamic properties of the vehicle in a highly complex manner.

The vertical tire load transmitted to the road surface comprises two components: the static load and a fluctuating component known as the dynamic tire force or dynamic wheel (axle) load. The static load depends on the geometry and mass distribution of the vehicle and the static load sharing properties of the suspension system [11]. The dynamic tire forces are attributed to motions of the moving sprung and unsprung masses of the vehicle excited by pavement surface roughness. It has been shown that the magnitudes of dynamic tire forces are also strongly influenced by the suspension properties [8]. Well-designed soft air suspensions with adequate damping generally cause lower dynamic loads than the mechanical suspensions [26]. The relative pavement loading aggressiveness of different vehicles and suspensions has been conveniently assessed in terms of a parameter referred to as the '*Dynamic Load Coefficient*' (DLC). The DLC is defined by the coefficient of variation of the tire force or the ratio of standard deviation of the dynamic tire force to the static tire force [27]. Although, the DLC serves as a convenient measure for assessing the relative pavement aggressiveness of different suspensions, tires and vehicles, the measure does not describe the compressive and shear stresses of the pavement surface. Furthermore, the measure is highly sensitive to the axle loads and may lead to misleading interpretations under varying loads [5].

Eisenmann [7] defined the '*road stress factor*' to assess pavement damage potential of dynamic tire forces. The approach employs the fourth-power low proposed in the early study by AASHTO [5] and a measure of DLC assuming even distribution of the damage along the pavement. The '*road stress factor*', ϕ, is related to static and instantaneous forces in the following manner:

$$\phi = E[F_t(t)^4] = (1 + 6\bar{s}^2 2 + 3\bar{s}^3)\,\bar{F}_t^4 \qquad (1.1)$$

Where $F_t(t)$ is the instantaneous tire force at time t, $\overline{F}_t$ is the static tire force, $\bar{s}$ is the coefficient of variation of the dynamic tire force or the *DLC*, and E[ ] is the expectation operator.

Deterioration of pavement structures and surfaces occurs as a result of many factors including the loads applied by the heavy vehicle tires, and the combined effects of traffic loads and environmental conditions [26]. The tire load and distribution of compressive stress in the "contact patch" or "footprint", are however, the most important indicators potential pavement responses, which are further dependent on the tire inflation pressure. A lower tire pressure would result in longer "footprint" and thus distribute the wheel loads over a greater pavement area [4,11]. Sweatman [8], however, reported that somewhat opposite was true for heavy vehicles employing some of the mechanical suspensions. For a given load, the dual tire assemblies generally yield a larger total contact area and thus lower compressive stresses than the wide-base single tires [11]. Cebon [11] concluded that the net road contact area of wide single tires is significantly smaller than dual tires for the same load, and the contact pressures are consequently higher. As a result the overall road damaging potential of wide– single tires is thought to be considerably higher than the dual pairs, despite the smaller dynamic tire force fluctuations. The design of modern wide-base single tires, however, can provide effectively larger contact area comparable to that of a dual-tire combination [11].

1.2.3 TIRE AND SUSPENSION MODELS

The nonlinear and linear models of various heavy vehicle mechanical suspensions have been widely reported in the literature [6,10], while the tire models are still evolving

partly due to complexities associated with the multilayer composite structure and partly due to constant changes that are being made to the materials or compounds [6]. The reported tire models are thus briefly discussed in this section.

Owing to the complexities associated with tire structure and material properties, the majority of the tire models seem to based on measured data and not on the structure or material properties [19]. The tire forces distributed over the tire-road contact patch are typically evaluated through simulations using the measured tire properties [11]. The distributed forces are generally expressed by two components in the plane of the contact attributed to braking/traction and cornering forces, and a normal force component distributed over the contact patch. The two tangential components in the plane of the road surface are usually modeled separately since they primarily depend on independent parameters, such as normal load, the longitudinal slip and the side-slip [20]. These are generally described by a range of regression models identified from the measured data. Of these, the *Magic tire formula* is most widely accepted for handling dynamic analyses of road vehicles [6,11]. This model permits for determination of all the force and moment components generated by the tire in pure cornering, pure longitudinal and combined cornering and braking analysis [10]. The *Magic Tire formula* is expressed in the following form:

$$\begin{aligned} Y &= y + S_v \\ y &= D\sin[C\ \tan^{-1}\{Bx - E(Bx - \tan^{-1}(Bx))\}] \\ x &= X - S_h \end{aligned} \tag{1.2}$$

Where Y is an output variable, such as longitudinal force or lateral force or aligning moment; X is the input variable, such as side-slip angle or longitudinal slip; parameters B, C and E represent stiffness, shape and curvature factors, respectively, while D denotes

the peak of the variable. The constants S_h and S_v are the horizontal and vertical shifts, respectively, in the force-slip or moment-slip relationships. This empirical formula is capable of producing characteristics that closely match the measured data in the lateral force F_y and the longitudinal force F_x, as functions of their respective slip quantities. The constants B, C, D, E, S_h and S_v are identified from measured data [10,21]. For small slip angles and small slip ratio values, the linear tire force relation between Y and X can be approximated by:

$$Y = (BCD)\,X \tag{1.3}$$

The quantity BCD thus represents the cornering stiffness or the longitudinal tire stiffness.

Nicolas and Comstock [20] proposed a regression model to predict the braking and cornering forces under combined braking and steering maneuvers. The model, however, resulted in relatively poor correlations with measured data under certain conditions. A *Modified Nicolas-Comstock model (MNC)* was subsequently proposed in [20], where the braking and cornering forces are related to side slip α and deformation slip i_s, as:

$$F_x(\alpha, i_s) = \frac{F_x(i_s)F_y(\alpha)\sqrt{(i_s C_\alpha)^2 + (1-s)^2(F_x(i_s)\cos(\alpha))^2}}{C_\alpha\sqrt{\left(i_s F_y(\alpha)\right)^2 + (F_x(i_s)\tan(\alpha))^2}} \tag{1.4}$$

$$F_y(\alpha, i_s) = \frac{F_x(i_s)F_y(\alpha)\sqrt{(C_s \sin(\alpha))^2 + (1-s)^2\left(F_y(\alpha)\cos(\alpha)\right)^2}}{C_s\cos(\alpha)\sqrt{\left(i_s F_y(\alpha)\right)^2 + (F_x(i_s)\tan(\alpha))^2}} \tag{1.5}$$

Where $F_x(i_s)$ is the longitudinal force corresponds to zero side-slip angle ($\alpha=0$) and $F_y(\alpha)$ is the lateral force corresponding to zero longitudinal slip ratio ($i_s=0$) . $F_x(\alpha, i_s)$ and $F_y(\alpha, i_s)$ are longitudinal and lateral forces, respectively in the presence of side-slip and

deformation slip ratio. C_s is the longitudinal stiffness and C_a is the cornering stiffness of the tire, and s is the deformation slip.

One of the simplest theories for predicting the cornering force available at a specific slip angle in the presence of a tractive or braking force is based on the *friction ellipse concept* [6]. The friction ellipse concept is based on the assumption that the tire may slide on the ground in any direction if the resultant of the longitudinal force (either tractive or braking) and lateral (cornering) force reaches the maximum value defined by limiting value of the coefficient of road adhesion and the normal load on the tire. However, the longitudinal and lateral force components may not exceed their respective maximum values Fx_{max} and Fy_{max}, which are generally identified from the measured tire data, and constitute the major and minor axis of the friction ellipse, respectively, as shown in Figure 1.1.

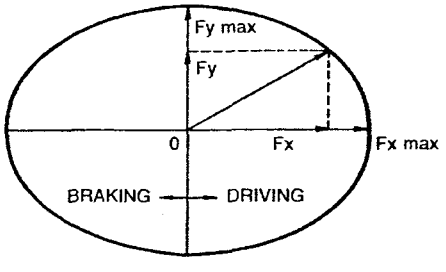

Figure 1.1: The friction ellipse concept relating the maximum cornering force to a given longitudinal force [6].

The available cornering force $F_y(\alpha, i_s)$ at a given slip angle, for any given tractive or braking force $F_x(\alpha, i_s)$, is then determined from the following relationship:

$$\left(\frac{Fx(\alpha, i_s)}{Fx(i_s)_{max}}\right)^2 + \left(\frac{Fy(\alpha, i_s)}{Fy(\alpha)}\right)^2 = 1 \tag{1.6}$$

1.2.4 HANDLING ANALYSES AND PERFORMANCE MEASURES

The handling characteristics of road vehicles have been extensively investigated using a wide range of analytical vehicle models. These include one-, two- and three-dimensional linear and nonlinear models involving linear and nonlinear component properties. A number of simulation models have been reviewed in a study by El-Gindy and Wong [31]. The one dimensional two-degrees-of-freedom (DOF) yaw-plane bicycle model, representing the lateral and yaw motions of the vehicle, is perhaps the simplest model that has been extensively used to obtain handling performance of road vehicles [6,10]. The model is valid for constant forward speed, assuming that braking forces do not greatly affect the lateral or yaw stability of the vehicle. Furthermore, the normal loads of the right-and left-track tires on each axle are assumed to be equal and thus no lateral load shift is considered. This model is thus inadequate to describe the roll motion of the sprung and unsprung masses associated with centrifugal acceleration excitation due to turning maneuver.

A number of two- dimensional yaw-plane handling dynamic models have been developed to describe the lateral and yaw motions of the vehicle subject to steering inputs similar to the bicycle model. These models consider lateral load shift influenced by the lateral vehicle acceleration, although the roll dynamics is neglected [10]. These models employ either linear or nonlinear properties of tires. The contributions due to roll dynamics of the sprung mass have also been incorporated by considering a limited roll-DOF of the sprung mass about the roll axis to the two-dimensional yaw-plane model [24,31]. Alternatively, comprehensive three-dimensional vehicle model, referred to yaw/roll model has been widely employed to study the lateral, yaw and roll motions of

the sprung and unsprung masses under steering inputs, while assuming constant forward speed [33]. The model includes nonlinear forces models due to suspension components and tires, and can be applied to different articulated vehicle combinations. A few studies have demonstrated the validity of this model using road-measured data. The model, however, is considered applicable for constant forward speed with negligible inter-axle load transfer. A more comprehensive vehicle model applicable for combined steering maneuvers has also been developed to investigate comprehensive directional dynamic performance of heavy vehicles subject to braking, or braking and steering input [31]. The model is referred to as phase-4.

A number of lumped-parameter and multi-body dynamic models of automobiles have also been reported in the literature with varying suspension and tire models [31,33]. Stone et al. [22] developed a full car model for simulating directional responses to cornering and braking maneuvers, as shown in Figure 1.2. The six-DOF vehicle sprung mass model was coupled with an analytical tire model capable of simulating the realistic cornering and braking behavior. Shim and Zhang [23] developed a 14-DOF vehicle model incorporating 6-DOF motions of the sprung mass and two-DOF of each of the four unsprung masses to investigate transient handling responses.

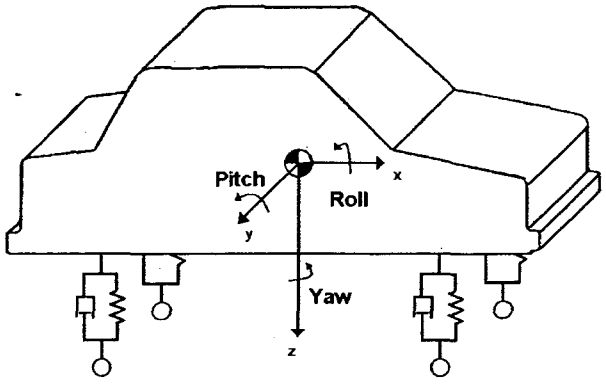

Figure 1.2: Vehicle coordinate system of the model [22].

The above reported models, however do not do not consider the effect of variations in the tire inflation pressure, which could be investigated by integrating an appropriate tire model or the tire data as a function of inflation pressure through a look-up table.

1.2.5 RIDE DYNAMIC MODELS

Since the vehicle dynamics is concerned with controllability and stability of the vehicle, the developments in reliable dynamic ride vehicle models is an important issue [29,37]. A large number of vehicle models of varying complexities have been reported in the literature for ride dynamic response analyses. The simplest model is the two-DOF quarter-car model, which comprises an equivalent suspension spring and a damper coupling the body (sprung mass) to a single wheel coupled to the ground via the tire spring. This model been widely used for preliminary analyses of bounce motion and different suspension design concepts [10,29,37,38]. The half-car model or pitch plane models have also evolved to study the vertical and pitch ride responses of the vehicle [10, 29,37]. Such models have also been developed for study of motions in roll plane [24]. The half-car models are relatively simple to analyze and yet can provide reasonably good prediction of responses to road inputs. A number of three-dimensional vehicle models have also been reported for more comprehensive ride dynamic analyses [38,39]. The number of DOF of such models may vary greatly depending on the modeling details of the suspension components. These models consider 7-DOF as minimum and include the bounce, pitch and roll motions of the sprung mass and bounce motion of the four unsprung masses [37,39], as shown in Figure 1.3. Such models also consider solid axles applicable to heavy vehicles which bounce and roll DOF, as shown in Figure 1.4 [5,29]. While the tires are modeled as nonlinear springs with viscous damping. The nonlinear

characteristics of the suspension components are modeled and validated based on the measured characteristics acquired under controlled conditions in the laboratory [1].

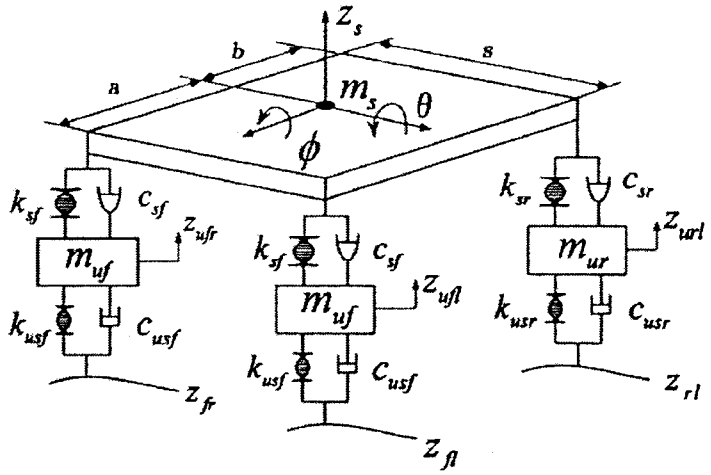

Figure 1.3: Three-dimensional ride dynamic model [37].

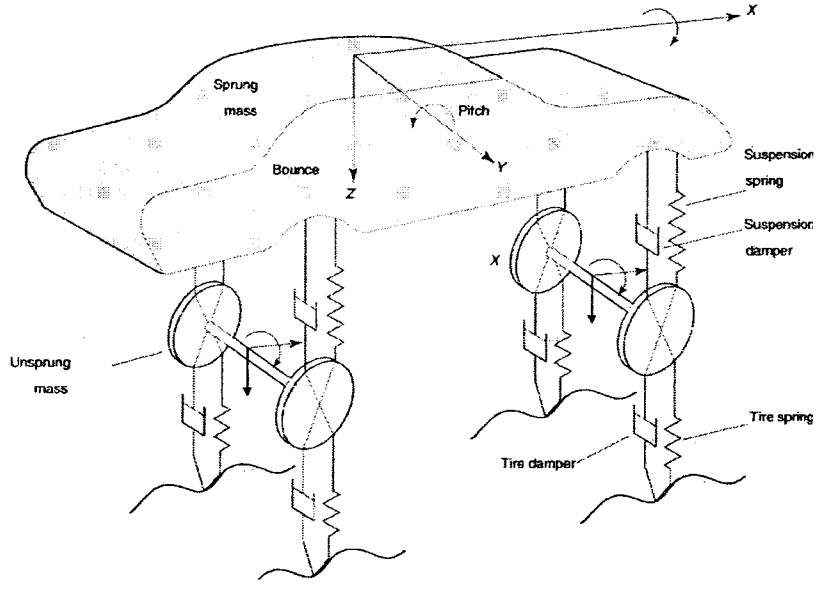

Figure 1.4: Modified three-dimensional ride dynamic model [29].

1.3 Scope of the Present Work

From the review of published studies, it is evident that the ride and handling dynamics of road vehicles have been extensively investigated through either road measurements or simulations of analytical models. The studies on role of tire pressure in

view of ride dynamics response have been limited mostly to off-road and military vehicles. These studies, however, are mostly based on field measurements. Furthermore, influence of tire pressure on the handling dynamics is mostly unknown. Considering the wide variations in passengers load in urban buses, the vehicle operation with rated pressure (110 psi/758 kpa) could be detrimental to vibration ride comfort and pavement loading performance of the bus. It would be desirable to reduce the operating tire pressure when only few passengers are present. This can be conveniently achieved through a central tire inflation system (CTIS) in a rapid manner, while the vehicle is in service. The use of CTIS will also reduce the frequency of unscheduled service interruptions due to leaky tires, which will be constantly inflated by the CTIS. Furthermore, a CTIS will ensure uniform pressure on all the vehicle tires and thereby yield some benefit in handling performance and tire service life. The vehicle operation with lower pressure tires, however, may lead to lower cornering force and effective roll stiffness which may reduce the handling quality and roll stability limits. A systematic study of handling properties of the bus with variable tire pressure is thus considered desirable.

The primary objective of this dissertation research is thus formulated to investigate the influence of variations in tire inflation pressure on the ride and handling dynamics of an urban bus. The specific objectives of this work can be summarized as follows:

- Study the urban bus ride and pavement loading dynamics under excitation arising from tire-road interactions through development and analysis of a low floor urban bus model integrating the nonlinear properties of the suspension components.

- Formulate performance measures related to ride dynamics and pavement loading performance and evaluate the influence of tire pressure on the measures.
- Investigate the effect of inflation pressure and normal load on cornering properties of tires through review of available data and develop an empirical model for predicting the cornering stiffness as a function of the inflation pressure and normal load.
- Develop a handling dynamic model incorporating the tire model and suspension characteristics, and investigate the influence of tire pressure on transient and steady state cornering properties of the vehicle.

1.4 Thesis Organization

Chapter 2 provides a detailed description of the three-dimensional ride dynamic model of the candidate urban bus comprising the 2-DOF suspension seat and driver model and nonlinear suspension component characteristics. The governing equations of motion of the ride dynamic model are derived based on the geometry, force-deflection and force-velocity characteristics of the suspension components

The free vibration responses of the ride dynamic model are evaluated about the nominal operating conditions in chapter 3 to identify the resonance frequencies of the model. The ride vibration responses to random road excitation and the performance measures related to ride dynamic wheel loads are assessed as a function of inflation pressure and normal load.

Two- and three-dimensional handling dynamic models of the vehicle are developed and presented in Chapter 4. Reported experimental data on tire cornering properties of the bus are reviewed and a cornering stiffness model is formulated to yield

the cornering properties as a function of the inflation pressure. The lateral tire force is computed based on the magic tire formula, while the model parameters are identified at each load and inflation pressure condition. The computed tire lateral force responses are compared with the measured data.

The response characteristics of the two- and three-dimensional handling dynamic models are compared in Chapter 5 under two different types of steering inputs. The relative merits of the models are discussed. The effect of inflation pressure on the handling dynamics is investigated using sinusoidal and step steer inputs. The steady-state handling characteristics are further evaluated under various inflation pressures and loading conditions.

The major conclusions together with key contribution of the study are finally summarized in Chapter 6.

CHAPTER 2

Ride Dynamic Model Development

2.1 Introduction

Urban buses exhibit complex ride vibration environment comprising comprehensive magnitudes of translational and rotational vibration and occasional intermittent shock motions arising from tire interactions with relatively rough surfaces and discontinuities in the urban roads. The magnitudes of ride vibration levels have been measured in a few studies for assessing potential health risks among the drivers, who are occupationally exposed to such vibration on a daily basis [5,11]. The ride dynamic models of the urban buses have also been developed in a few studies, which generally consider simplified tire and suspension component models [1,5]. Such models, however, can also be effectively applied to investigate the dynamic tire forces transmitted to pavements for assessing their road damaging potential. A recent feasibility study has shown that an urban bus operation under varying tire pressure with varying passengers load would be feasible for improved vehicle ride and operating efficiency [42]. The influence of inflation pressure on the selected ride measures and dynamic wheel load coefficients were also investigated to assess the feasibility of a CTIS for urban buses.

In this chapter, a comprehensive three-dimensional ride dynamic model of a *low floor unban bus* (LFS) is developed based on the laboratory-measured nonlinear properties of the vehicle components reported in [2]. The geometric and force-deflection nonlinearities of the suspension, tires as a function of the inflation pressure, are

specifically emphasized in the model. The governing equations of motion of the model are formulated and the excitations due to the road roughness are described.

2.2 Model Description

A 9-DOF model of the urban buss is formulated to investigate its ride dynamic and pavement load responses to random road excitations. Figure 2.1 illustrates the vehicle model in the pitch-plane, and the front-axle roll-plane model is shown in Figure 2.2. The front axle suspension consists of four identical air sprigs with two air springs on each side of the axle, and two inclined dampers as shown in Figures 2.2 and 2.4. A constant forward speed is assumed in the model formulation. The DOFs include vertical (z_{sb}), roll (φ_{sb}) and pitch (θ_{sb}) motions of the lumped sprung mass that is assumed to be rigid with negligible contribution due to bending and torsion of the chassis structure; vertical (z_{uf}) and roll (φ_{uf}) motions of the unsprung mass due to front axle, which is a solid beam axle; vertical (z_{ur}) and roll (φ_{ur}) motions of the unsprung mass due to the rear axle; and vertical motion of the suspension seat (z_s) and driver (z_l) represented by a rigid mass. Figure 2.3 illustrates the model in the roll-plane of the rear axle. The rear axle suspension also comprises four air springs as in case of the front-axle suspension. The air springs, however, are placed well-ahead and behind the axle shaft, as seen in the pitch plane in Figure 2.1. The rear axle suspension also employs four hydraulic dampers and an anti-roll bar. The dual tires are lumped together and represented by a single composite tire.

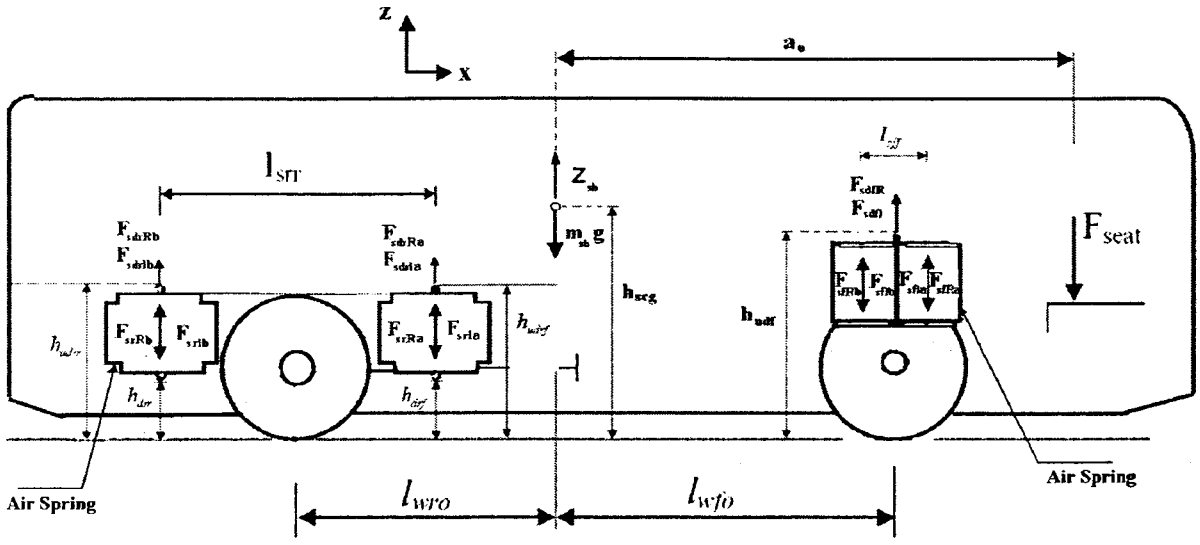

Figure 2.1: Illustration of ride dynamic model of the bus in the pitch-plane.

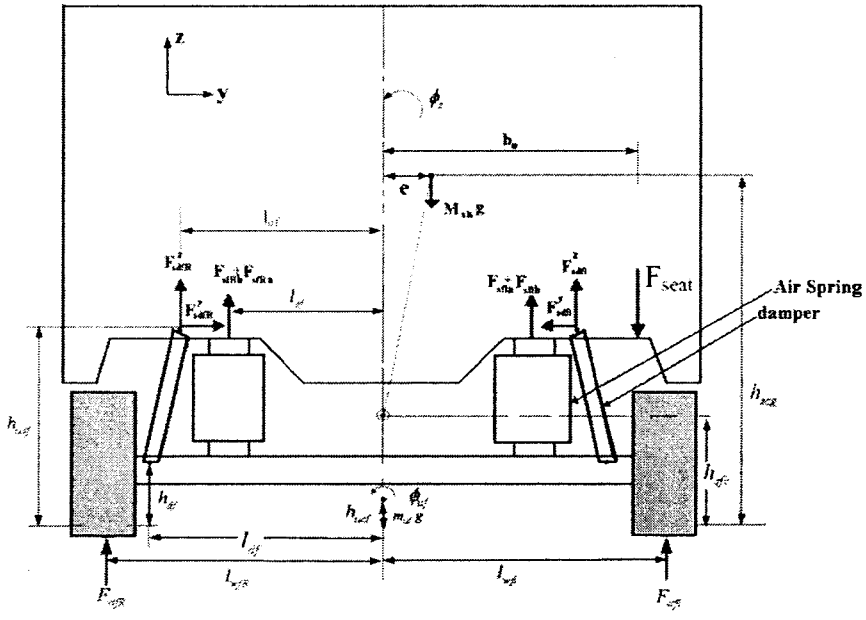

Figure 2.2: Illustration of ride dynamic model of the bus in the front axle roll-plane.

Figures 2.4 and 2.5 illustrate the layout of air springs and dampers in the front and rear-axles, respectively. The suspension dampers are indicated by a mere bold line link in each case. The detailed component models are described in the following subsections.

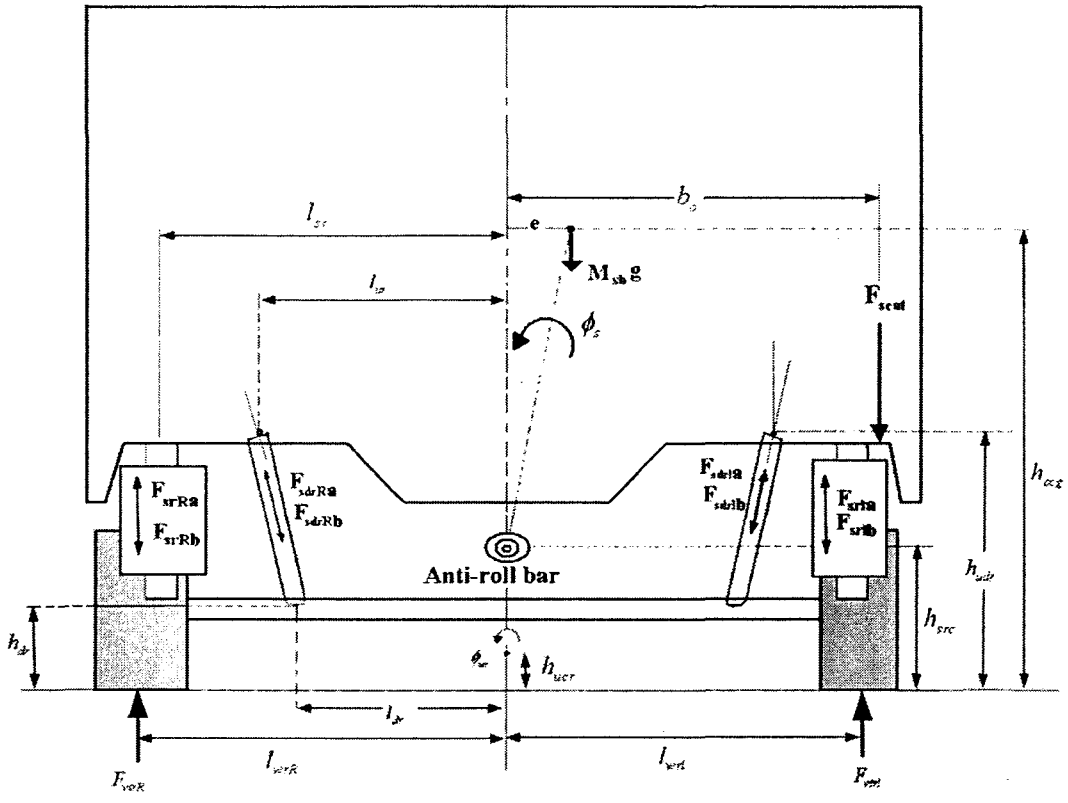

Figure 2.3: Illustration of ride dynamic model of the bus in the rear axle roll-plane.

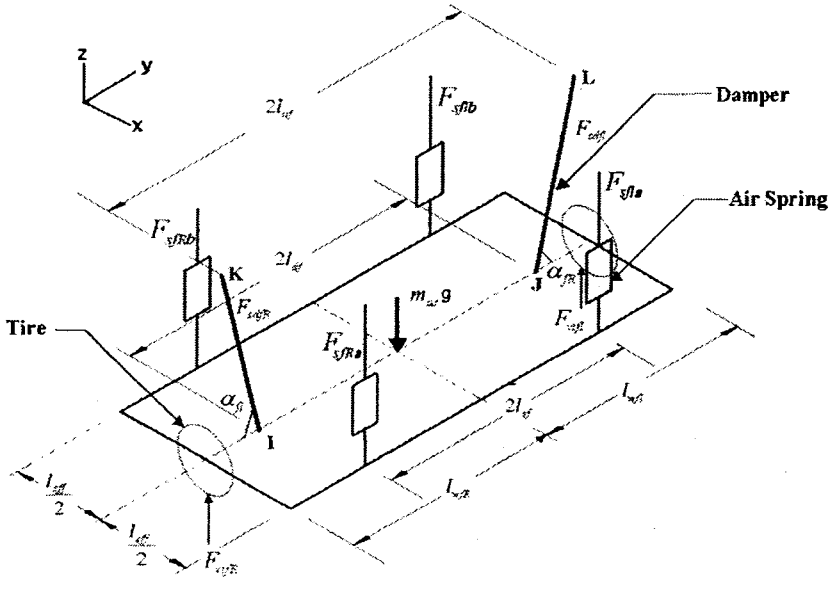

Figure 2.4: Front axle suspension configuration.

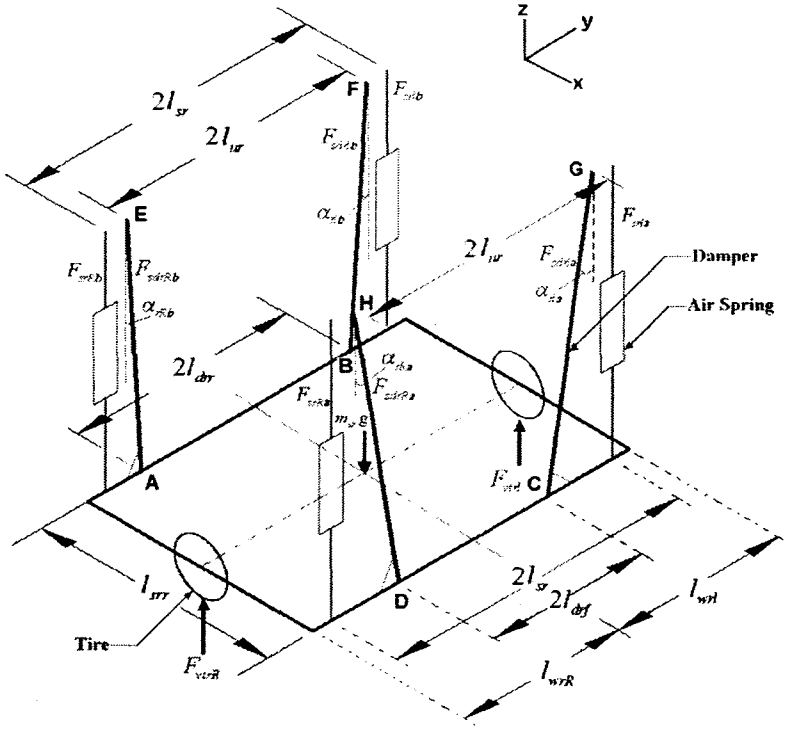

Figure 2.5: Rear axle suspension configuration.

2.2.1 DRIVER-SEAT-SUSPENSION MODEL

Urban buses generally employ a vertical suspension seat to reduce the transmission of road-induced shock and vibration to the seated driver and to provide essential seat adjustments. The development of a suspension seat model is thus essential to perform ride comfort or driver-friendliness analysis of the total vehicle. The contributions due to biodynamics of the human driver to the overall dynamics of the coupled-seat suspension, are known to be smaller for low natural frequency suspension seats [5]. Moreover, the modeling of the seated occupant is a complex task, particularly with regards to changes in the human driver mass and vibration levels [35]. The human mass in this study is represented by a rigid mass equal to the mass supported by the seat (approximately 80% of total body mass [5,35]), which is considered adequate for relative

analyses of the tire inflation pressure. The proposed driver-seat-suspension model consists of mass m_o representing the driver mass, suspension seat mass m_s, and cushion and suspension properties. The suspension seat model shown in Figure 2.6, employs linear stiffness and damping due to cushion material, linear stiffness properties of the air spring, nonlinear force-velocity characteristics of the damper, coulomb friction due to guides and bushings, and elastic properties of the motion limiter.

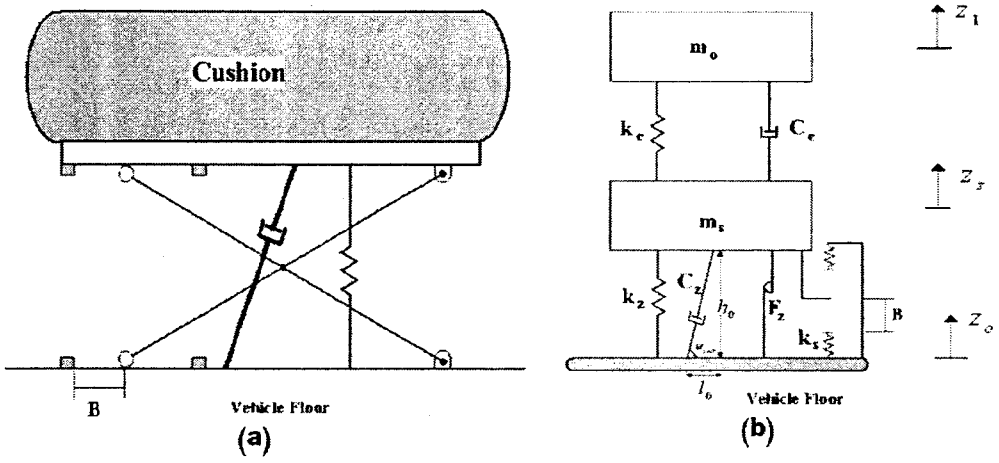

Figure 2.6: (a) Seat components; (b) Two-DOF model of the vertical driver-seat-suspension.

The equations of motion of the two-DOF driver-seat-suspension model are formulated as [35]:

$$m_o\ddot{z}_1 + k_c(z_1 - z_s) + C_c(\dot{z}_1 - \dot{z}_s) = 0 \tag{2.1}$$

$$m_s\ddot{z}_s + k_c(z_s - z_1) + C_c(\dot{z}_s - \dot{z}_1) + k_z(z_s - z_o) + F_c + F_d\sin\alpha_s + F_s = 0 \tag{2.2}$$

Where k_c, C_c and k_z are cushion stiffness, cushion damping coefficients and seat suspension stiffness respectively, and F_c is the coulomb friction force assumed to act along the axis of the damper and is expressed by its magnitude F_z as:

$$F_c = F_z\text{sign}(\dot{z}_s - \dot{z}_o) \tag{2.3}$$

Where α_s is the instantaneous inclination angle of the damper, expressed as:

$$\sin \alpha_s = \frac{h_0 + \delta_s}{\sqrt{(h_0 + \delta_s)^2 + {l_0}^2}} \tag{2.4}$$

Where h_o is the vertical damper height in static equilibrium, and l_o is the horizontal projection of the inclined damper (Figure 2.6) and $\delta_s = z_s - z_o$, z_o being the vertical displacement excitation at the base of the seat. F_d is the damping force developed along the axis of the damper as function of its damping characteristics, which is assumed to be symmetric in compression and rebound, and piecewise linear function of relative velocity in low and high velocity ranges [35], such that:

$$F_d = \begin{cases} C_A V_d & , |V_r| < V_s \\ C_A V_r \, sign(V_d) + C_B[V_d - V_s \, sign(V_d)] & , |V_r| > V_s \end{cases} \tag{2.5}$$

Where C_A and C_B are the damping coefficients corresponding to low and high velocities (Figure 2.7), V_s is the transition velocity and $V_d = \dot{\delta}_{so} \sin(\alpha)$ is the relative velocity along the damper axis.

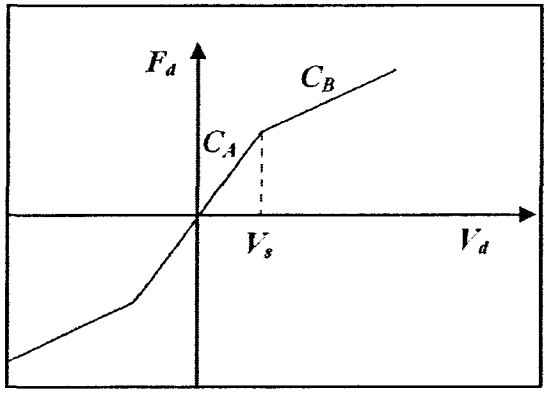

Figure 2.7: Symmetric force-velocity characteristics of seat-suspension damper.

In Eq. (2.2), F_s is the suspension force developed due to contacts with motion limiting stops, expressed as:

$$F_s = k_s S[\delta_s - B\text{sign}(\delta_s)] \tag{2.6}$$

Where B is half the suspension travel, k_s is spring rate of the motion limiting stops, and S is a nonlinear function used to describe the contact condition with the motion limiting stop, given by:

$$S = \begin{cases} 0 & ,|\delta_s| < B \\ 1 & ,|\delta_s| > B \end{cases}$$

The vertical excitation $z_o(t)$ at the driver seat location is derived from the motion of the sprung mass, such that:.

$$z_o = z_{sb} - a_o\theta_{sb} + b_o\phi_{sb} \tag{2.7}$$

Where a_o and b_o are longitudinal and lateral distances from the bus body cg to driver seat location, respectively, the resultant suspension force F_{seat} is also combined to act on the sprung mass and expressed as:

$$F_{seat} = -[k_z(z_s - z_o) + F_c + F_d \sin\alpha_s + F_s] + (m_s + m_o)g \tag{2.8}$$

2.2.2 EQUATIONS OF MOTION OF THE SPRUNG AND UNSPRUNG MASSES

Assuming negligible coupling with the longitudinal and lateral dynamics, the ride dynamics of the vehicle can be represented by 7 DOF motions comprising vertical (z_{sb}), roll (φ_{sb}) and pitch (θ_{sb}) motions of the sprung mass, and (z_{uf}, φ_{uf}) and (z_{ur}, φ_{ur}) of the unsprung masses. The equations of motion for the vehicle model are derived upon considering the nonlinear force-deflection relations for the air springs and the force–velocity relations for the dampers, while the DOFs due to seat occupant model are represented by the resultant force F_{seat}, as described in Eq. (2.8). The equations of motion derived for the sprung and unsprung masses are expressed below.

Bounce motion of the sprung mass:

$$m_{sb}\ddot{z}_{sb} = (F_{sfla} + F_{sflb} + F_{sfRa} + F_{sfRb}) + (F_{sdfl}\cos\alpha_{fl} + F_{sdfR}\cos\alpha_{fR}) + (F_{sdrla}\cos\alpha_{rla} + F_{sdrlb}\cos\alpha_{rlb} + F_{sdrRa}\cos\alpha_{rRa} + F_{sdrRb}\cos\alpha_{rRb}) (F_{srla} + F_{srlb} + F_{srRa} + F_{srRb}) - m_{sb}g - F_{seat} \quad (2.9)$$

Pitch motion of the sprung mass:

$$I_{sb\theta}\ddot{\theta}_s = -(F_{sfRb} + F_{sflb})(l_{wfo} - \frac{l_{sff}}{2}) - (F_{sfRa} + F_{sfla})(l_{wfo} + \frac{l_{sff}}{2}) - (F_{sdfl}\cos\alpha_{fl} + F_{sdfR}\cos\alpha_{fR})\, l_{wfo} + [F_{srRb} + F_{srlb} + F_{sdrRb}\cos\alpha_{rRb} + F_{sdrlb}\cos\alpha_{rlb}]\left(l_{wro} + \frac{l_{srr}}{2}\right) + (F_{srRa} + F_{srla} + F_{sdrRa}\cos\alpha_{rRa} + F_{sdrla}\cos\alpha_{rla})(l_{wro} - \frac{l_{srr}}{2}) + F_{seat}a_o \quad (2.10)$$

Roll motion of the sprung mass:

$$I_{sb\phi}\ddot{\phi}_{sb} = (F_{sfla} + F_{sflb})l_{sf} - (F_{sfRa} + F_{sfRb})l_{sf} + (F_{sdfl}\cos\alpha_{fl} - F_{sdfR}\cos\alpha_{fR})l_{uf} + (F_{sdfl}\cos\alpha_{fl} - F_{sdfR}\cos\alpha_{fR})l_{uf} + (F_{sdfl}\sin\alpha_{fl} - F_{sdfR}\sin\alpha_{fR})(h_{udf} - h_{sfc}) + [F_{srla} + F_{srlb} - (F_{srRa} + F_{srRb})]l_{sr} + [(F_{sdrla}\cos\alpha_{rla} - F_{sdrRa}\cos\alpha_{rRa}) + (F_{sdrlb}\cos\alpha_{rlb} - F_{sdrRb}\cos\alpha_{rRb})]l_{ur} + (F_{sdrRa}\sin\alpha_{rRa} - F_{sdrla}\sin\alpha_{rla})(h_{udrf} - h_{src}) + (F_{sdrRb}\sin\alpha_{rRb} - F_{sdrlb}\sin\alpha_{rlb})(h_{udrr} - h_{src}) + M_{\phi sur} - F_{seat}b_o - m_{sb}(g - \ddot{z}_{sb})\left[e - \left(h_{scg} - \frac{l_{wro}h_{sfc} + l_{wfo}h_{src}}{l_{wro} + l_{wfo}}\right)\phi_{sb}\right] \quad (2.11)$$

Bounce motion of the front-axle unsprung mass:

$$m_{uf}\ddot{z}_{uf} = F_{vtfl} + F_{vtfR} - (F_{sfla} + F_{sflb} + F_{sfRa} + F_{sfRb}) - (F_{sdfl}\cos\alpha_{fl} + F_{sdfR}\cos\alpha_{fR}) - m_{uf}g \quad (2.12)$$

Roll motion of the front-axle unsprung mass:

$$I_{uf}\ddot{\phi}_{uf} = F_{vtfl}l_{wfl} - F_{vtfR}l_{wfR} + [(F_{sfRa} + F_{sfRb}) - (F_{sfla} + F_{sflb})]l_{sf} - (F_{sdfl}\cos\alpha_{fl} - F_{sdfR}\cos\alpha_{fR})l_{df} - (F_{sdfl}\sin\alpha_{fl} - F_{sdfR}\sin\alpha_{fR})(h_{df} - h_{ucf}) - m_{uf}(g + \ddot{z}_{uf})(h_{uf} - h_{ucf})\phi_{uf} \quad (2.13)$$

Bounce motion of the rear-axle unsprung mass:

$$m_{ur}\ddot{z}_{ur} = F_{vtrl} + F_{vtrR} - (F_{srla} + F_{srlb} + F_{srRa} + F_{srRb}) - (F_{sdrla}\cos\alpha_{rla} + F_{sdrlb}\cos\alpha_{rlb} + F_{sdrRa}\cos\alpha_{rRa} + F_{sdrRb}\cos\alpha_{rRb}) - m_{ur}g \quad (2.14)$$

Roll motion of the rear-axle unsprung mass:

$$I_{ur}\ddot{\phi}_{ur} = F_{vtrl}l_{wrl} - F_{vtrR}l_{wrR} - [F_{srla} + F_{srlb} - (F_{srRa} + F_{srRb})] - (F_{sdrla}\cos\alpha_{rla} - F_{sdrRa}\cos\alpha_{rRa})l_{drf} - (F_{sdrlb}\cos\alpha_{rlb} - F_{sdrRb}\cos\alpha_{rRb})l_{drr} - (F_{sdrRa}\sin\alpha_{rRa} - F_{sdrla}\sin\alpha_{rla})(h_{drf} - h_{ucr}) - (F_{sdrRb}\sin\alpha_{rRb} - F_{sdrlb}\sin\alpha_{rlb})(h_{drr} - h_{ucr}) - M_{\phi sur} + m_{ur}(g - \ddot{z}_{ur})(h_{ur} - h_{ucr})\phi_{ur} \quad (2.15)$$

In the above equations m_{sb}, m_{uf} and m_{ur} are the masses of the body and chassis, front axle assembly and rear axle assembly, respectively. $I_{sb\varphi}$ and $I_{sb\theta}$ are the roll and pitch mass moments of inertia of the sprung mass, respectively about its mass center (c.g), and I_{uf} and I_{ur} are the roll mass moments of inertia of the front and rear axle assemblies, respectively, about their respective mass centers. The nonlinear forces due to tires and suspension are derived from the component models established in [1], which are described in the following sections.

2.2.3 SUSPENSION FORCES

The forces due to suspension springs and dampers are integrated within the total vehicle model through appropriate considerations of the kinematic and dynamic motions of the sprung and unsprung masses [5]. In Eqs. (2.9) to (2.15), F_{sijk} ($i=f$, r; $j=l$, R; $k=a$, b) are the forces developed by the air springs, where f and r refer to front and rear axle, R and l refer to right and left track, and a and b refer to location of the spring ahead or behind the axle shaft. F_{sdfj} ($j=l$, R) represents the damper forces of the front axle, and F_{sdijk} ($i=f$, r; $j=l$, R; $k=a$, b) are the forces due to dampers of the rear axle suspension. F_{vtfl}, F_{vtfR}, F_{vtrl} and F_{vtrR} represent the vertical tire forces, where the subscripts f and r refer to front or rear axle tires, and R and l refer to left or right tire. α_{fl} and α_{fR} are the inclination angles of left and right dampers of the front axle in the roll plane, respectively, as shown in Figure 2.4. The angles α_{rjk} ($j=l$, R; $k=a$, b) are inclination

angles of the rear-axle dampers in the roll plane, as show in Figure 2.5. The parameters l_{sff}, l_{srr}, l_{sf}, l_{sr}, l_{uf}, l_{df}, l_{drr}, l_{ur} and l_{drf} represent the coordinates of the air springs and dampers mounts on the sprung and unsprung masses assemblies, and l_{wfR}, l_{wfl}, l_{wrR} and l_{wrl} denote coordinates of the tire-ground contacts with respect to the roll plane vertical geometric centerline, as shown in Figures 2.1 to 2.5.

The dynamic force generated by air springs employed in the front and rear axle suspension systems are modeled based on the experimental data reported in [9]. The air springs are coupled with height leveling valve, and maintain constant ride irrespective of the bus loading condition. The dynamic force developed by an air spring can be expressed as a function of instantaneous air pressure and effective piston area, which are further related to instantaneous dynamic spring deflection. The instantaneous dynamic deflections of the front axle suspension springs δ_{fjk} (j=l, R; k=a, b), are derived from:

$$\begin{aligned}
\delta_{fla} &= z_{sb} + l_{sf}\phi_{sb} - \left(l_{wfo} + \frac{l_{sff}}{2}\right)\theta_{sb} - \left(z_{uf} + l_{sf}\phi_{uf}\right) \\
\delta_{flb} &= z_{sb} + l_{sf}\phi_{sb} - \left(l_{wfo} - \frac{l_{sff}}{2}\right)\theta_{sb} - \left(z_{uf} + l_{sf}\phi_{uf}\right) \\
\delta_{fRa} &= z_{sb} - l_{sf}\phi_{sb} - \left(l_{wfo} + \frac{l_{sff}}{2}\right)\theta_{sb} - \left(z_{uf} - l_{sf}\phi_{uf}\right) \\
\delta_{fRb} &= z_{sb} - l_{sf}\phi_{sb} - \left(l_{wfo} - \frac{l_{sff}}{2}\right)\theta_{sb} - \left(z_{uf} - l_{sf}\phi_{uf}\right)
\end{aligned} \tag{2.16}$$

Where l_{sf} is half the front-axle suspension spring track width, l_{wfo} is the distance from bus c.g to front axle and l_{sff} is the distance between the front-axle air springs mounted at the same track. The deflections of the rear axle springs δ_{rjk} (j=l, R; k=a, b) are derived in a similar manner, as:

$$\begin{aligned}
\delta_{rla} &= z_{sb} + l_{sr}\phi_{sb} + \left(l_{wro} - \frac{l_{srr}}{2}\right)\theta_{sb} - (z_{ur} + l_{sr}\phi_{ur}) \\
\delta_{rlb} &= z_{sb} + l_{sr}\phi_{sb} + \left(l_{wro} + \frac{l_{srr}}{2}\right)\theta_{sb} - (z_{ur} + l_{sr}\phi_{ur}) \\
\delta_{rRa} &= z_{sb} - l_{sr}\phi_{sb} + \left(l_{wro} - \frac{l_{srr}}{2}\right)\theta_{sb} - (z_{ur} - l_{sr}\phi_{ur}) \\
\delta_{rRb} &= z_{sb} - l_{sr}\phi_{sb} + \left(l_{wro} + \frac{l_{srr}}{2}\right)\theta_{sb} - (z_{ur} - l_{sr}\phi_{ur})
\end{aligned} \tag{2.17}$$

Where l_{sr} is half the rear-axle suspension spring track width, l_{wro} is the distance from bus c.g to rear axle, and l_{srr} is the distance between the rear-axle air springs mounted at the same track. The dynamic force generated by air springs is generally expressed as:

$$F_s = (P_s - P_a)A_E \tag{2.18}$$

Where P_s is instantaneous air pressure, P_a is atmospheric pressure and A_E is effective area of the air spring. It has been shown that the effective area and the instantaneous pressure are nonlinear functions of dynamic spring deflection [9]. Assuming polytropic process of the gas, the instantaneous pressure is related to deflection, as:

$$P_s = \frac{P_o V_o^{\gamma}}{(V_o + A_E\,\bar{\delta})^{\gamma}} \tag{2.19}$$

Where P_o and V_o are the static air pressure and volume, respectively, γ is polytropic constant taken as 1.1 [9], and $\bar{\delta}$ is the spring deflection. On the basis of the measured data the effective area of the air springs employed in bus suspension have been related to spring deflection by a 6th order polynomial function [9]:

$$A_E = k_0 + k_1\bar{\delta} + k_2\bar{\delta}^2 + k_3\bar{\delta}^3 + k_4\bar{\delta}^4 + k_5\bar{\delta}^5 + k_6\bar{\delta}^6 \tag{2.20}$$

The coefficients of the polynomial function are presented in
Table 2.1 for the front and rear axle air springs. The static forces on the front and rear springs, F_{sijko} (i=f, r; j=l, R; k=a, b) are derived from the sprung mass distribution, eccentricity e of the LFS, as:

$$F_{sflfo} = F_{sflro} = \frac{m_{sbf}(l_{sf}+e)g}{4l_{sf}}; F_{sfRfo} = F_{sfRro} = \frac{m_{sbf}(l_{sf}-e)g}{4l_{sf}}$$
$$F_{srlfo} = F_{srlro} = \frac{m_{sbr}(l_{sr}+e)g}{4l_{sr}}; F_{srRfo} = F_{srRro} = \frac{m_{sbr}(l_{sr}-e)g}{4l_{sr}} \quad (2.21)$$

Where m_{sbf} and m_{sbr} are the proportions of the sprung mass supported by the front and rear axles, respectively, given by:

$$m_{sbf} = \frac{l_{wro}m_{sb}}{l_{wro}+l_{wfo}}; \; m_{sbr} = \frac{l_{wfo}m_{sb}}{l_{wro}+l_{wfo}} \quad (2.22)$$

Table 2.1: Coefficients of the 6th order polynomial functions for the effective area of the air springs.

Air Spring Model	Coefficient						
	k_0	k_1	k_2	k_3	k_4	k_5	k_6
Front Axle (IR08-036)	29.8	0.429	-0.3941	-0.06762	0.042	-0.002678	-0.00094
Rear Axle (IR11-130)	75.92	-1.608	-0.0233	0.14998	0.0043	-0.007893	0.00054

Automotive dampers, in general, exhibit asymmetric multi-stage damping in compression and rebound, while the rebound damping force tends to be considerably larger than compressive damping force. Furthermore, damper force tends to vary rapidly at lower velocities due to flows through bleed valves, the rate of change of damper force with velocity vanishes at higher velocities, as large flows occur through blow-off valves. Such damping properties are often represented by piecewise linear functions in velocity [1]. The total force developed by a hydraulic damper comprises components due to gas, seal friction and hydraulic flows, while the gas force is often assumed negligible. The total damper force F_{sd} can thus be expressed as:

$$F_{sd} = F_{sdv} + F_{sdF} \tag{2.23}$$

Where F_{sdv} is the damper force due to hydraulic flows and F_{sdF} is the seal friction force. The measured data revealed different magnitudes of seal friction force in compressive and rebound, which are modeled as coulomb friction forces.

The hydraulic damping characteristics can be presented by the generalized piecewise linear curve shown in Figure 2.8 illustrating two-stage compression damping and three-stage rebound damping. The generalized characteristics show that the dampers yield high damping coefficients in rebound and compression (C_{e1} and C_{c1}) at low velocities than those at higher velocity (C_{c2} and C_{e2} or C_{e3}). The damping force can thus be expressed as:

$$\begin{aligned}
&F_{sdv} = C_{c1}V\ ; && V_{c1} \le V \le 0\\
&F_{sdv} = C_{c1}V_{c1} + \gamma_c C_{c1}(V - V_{c1})\ ; && V \le V_{c1}\\
&F_{sdv} = p\, C_{c1}V\ ; && 0 \le V \le V_{e1}\\
&F_{sdv} = p\, C_{c1}V_{e1} + p\, C_{c1}\gamma_{e1}\ (V - V_{e1})\ ; && V_{e1} \le V \le V_{e2}\\
&F_{sdv} = p\, C_{c1}V_{e1} + p\, C_{c1}\gamma_{e1}\,(V_{e2} - V_{e1}) + p\, C_{c1}\gamma_{e2}(V - V_{e2}); && V \ge V_{e2}
\end{aligned} \tag{2.24}$$

Where F_{sdv} is the hydralic damping force across the damper,V is the relative vlocity across the damper, C_{c1} and C_{c2} are high and low speed compression damping coefficients, V_{c1} is transition velocity in the compression mode. C_{e1}, C_{e2} and C_{e3} are low, medium and high speed damping coefficients in the rebound mode, respectively, and V_{e1} and V_{e2} are transition velocities corresponding to the three-stage rebound damping. The damper model is expressed in terms of its compression mode damping coefficient, by defining $p = C_{e1}/C_{c1}$ as the damping asymmetry factor, $\gamma_c = C_{c2}/C_{c1}$ as the compression damping reduction factor, and $\gamma_{e1} = C_{e2}/C_{e1}$ and $\gamma_{e2} = C_{e3}/C_{e1}$ as the rebound damping reduction factors.

Table 2.2: Damping coefficients of the damper models.

Damper Model	Damping Coefficient (Ns/m)					Transition Velocity (m/s)		
	Compression		Rebound			Compression	Rebound	
	C_{cl}	γ_c	p	γ_{el}	γ_{e2}	V_{cl}	V_{el}	V_{e2}
Arvin T801	624.6	1.0	19.399	0.378	0.378	0.0	0.315	0.315
Arvin T712	1972.8	1.0	15.668	0.166	0.166	0.0	0.1499	0.1499

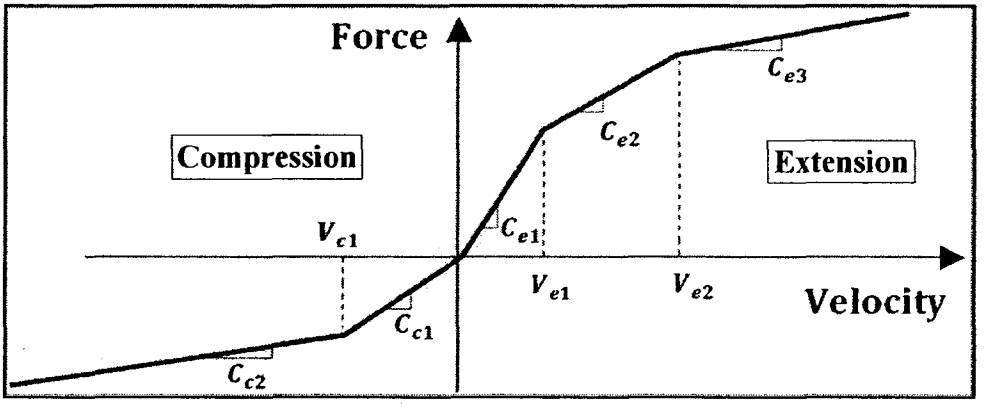

Figure 2.8: Generalized piecewise linear force-velocity characteristics of multi-stage asymmetric hydraulic dampers.

As mentioned earlier the bus suspension system comprising six dampers, two of which are located at the front axle and four in the rear axle suspension, as shown in Figures 2.4 and 2.5. The front axle dampers are inclined in the roll plane with angles α_{fl}, α_{fR}. The leading dampers in the rear axle suspension are inclined at angles α_{rla} and $\alpha_{rRa,}$, while the inclination angles of the trailing rear dampers are α_{rlb} and α_{rRb} (Figure 2.5). The front-axle dampers are inclined toward the geometric roll plane vertical centerline, while the rear-axle dampers are inclined outward. The instantaneous inclination angles can be derived from the geometry. The angles of the front axle dampers are derived as:

$$\alpha_{fl} = \tan^{-1}\left(\frac{l_{uf} - l_{df}}{h_{udf} - h_{df} + \delta_{dfl}}\right)$$
$$\alpha_{fR} = \tan^{-1}\left(\frac{l_{uf} - l_{df}}{h_{udf} - h_{df} + \delta_{dfR}}\right) \quad (2.25)$$

$$\alpha_{rla} = \tan^{-1}\left(\frac{l_{ur} - l_{drf}}{h_{udrf} - h_{drf} + \delta_{drlf}}\right)$$
$$\alpha_{rRa} = \tan^{-1}\left(\frac{l_{ur} - l_{drf}}{h_{udrf} - h_{drf} + \delta_{drRf}}\right)$$
$$\alpha_{rlb} = \tan^{-1}\left(\frac{l_{ur} - l_{drr}}{h_{udrr} - h_{drr} + \delta_{drlr}}\right) \quad (2.26)$$
$$\alpha_{rRb} = \tan^{-1}\left(\frac{l_{ur} - l_{drr}}{h_{udrr} - h_{drr} + \delta_{drRr}}\right)$$

δ_{dfl}, δ_{fR}, δ_{drla}, δ_{drl}, δ_{drRa} and δ_{drRb} are the vertical displacement across the front and rear-axle dampers, respectively, which can be expressed as :

$$\delta_{dfl} = z_{sb} + l_{uf}\phi_{sb} - l_{wfo}\theta_{sb} - (z_{uf} + l_{df}\phi_{uf})$$
$$\delta_{dfR} = z_{sb} - l_{uf}\phi_{sb} - l_{wfo}\theta_{sb} - (z_{uf} - l_{df}\phi_{uf}) \quad (2.27)$$

$$\delta_{drla} = z_{sb} + l_{ur}\phi_{sb} + \left(l_{wro} - \frac{l_{srr}}{2}\right)\theta_{sb} - (z_{ur} + l_{drf}\phi_{ur})$$
$$\delta_{drlb} = z_{sb} + l_{ur}\phi_{sb} + \left(l_{wro} + \frac{l_{srr}}{2}\right)\theta_{sb} - (z_{ur} + l_{drr}\phi_{ur})$$
$$\delta_{drRa} = z_{sb} - l_{ur}\phi_{sb} + \left(l_{wro} - \frac{l_{srr}}{2}\right)\theta_{sb} - (z_{ur} - l_{drf}\phi_{ur}) \quad (2.28)$$
$$\delta_{drRb} = z_{sb} - l_{ur}\phi_{sb} + \left(l_{wro} + \frac{l_{srr}}{2}\right)\theta_{sb} - (z_{ur} - l_{drr}\phi_{ur})$$

The relative velocities across the dampers are derived from the damper mounts velocities and the inclination angles of the dampers, such that:

$$V_{dfl} = (\dot{z}_L - \dot{z}_J)cos\ \alpha_{fl}$$
$$V_{dfR} = (\dot{z}_K - \dot{z}_I)cos\ \alpha_{fR}$$
$$V_{drla} = (\dot{z}_G - \dot{z}_C)\cos\ \alpha_{rla} \quad (2.29)$$
$$V_{drRa} = (\dot{z}_H - \dot{z}_D)\cos\ \alpha_{rRa}$$
$$V_{drlb} = (\dot{z}_F - \dot{z}_B)\cos\ \alpha_{rlb}$$
$$V_{drRb} = (\dot{z}_E - \dot{z}_A)\cos\ \alpha_{rRb}$$

Where velocity subscripts *A*, *B*, *C*, *D*, *E*, *F*, *G*, *H*, *J* and *K* refer to the damper mount locations, as shown in Figures 2.4 and 2.5. The velocity of the damper mounts $\dot{z}_i$ (*i=A, B, C,...., K*) can be derived from the motions of the sprung and unsprung masses. The relative velocities across the front axle dampers are thus expressed as:

$$\begin{aligned} V_{dfl} &= [\dot{z}_{sb} + l_{uf}\dot{\phi}_s - l_{wfo}\dot{\theta}_s - (\dot{z}_{uf} + l_{df}\dot{\phi}_{uf})]cos\,\alpha_{fl} \\ V_{dfR} &= [\dot{z}_{sb} - l_{uf}\dot{\phi}_s - l_{wfo}\dot{\theta}_s - (\dot{z}_{uf} - l_{df}\dot{\phi}_{uf})]\,cos\,\alpha_{fR} \end{aligned} \tag{2.30}$$

In a similar manner, the velocities across the rear axle suspension dampers are expressed as:

$$\begin{aligned} V_{drla} &= \left[\dot{z}_{sb} + l_{ur}\dot{\phi}_{sb} + \left(l_{wro} - \frac{l_{srr}}{2}\right)\dot{\theta}_{sb} - (\dot{z}_{ur} + l_{drf}\dot{\phi}_{ur})\right] cos\,\alpha_{rlf} \\ V_{drRa} &= \left[\dot{z}_{sb} - l_{ur}\dot{\phi}_{sb} + \left(l_{wro} - \frac{l_{srr}}{2}\right)\dot{\theta}_{sb} - (\dot{z}_{ur} - l_{drf}\dot{\phi}_{ur})\right]\,cos\,\alpha_{rRf} \\ V_{drlb} &= \left[\dot{z}_{sb} + l_{ur}\dot{\phi}_{sb} + \left(l_{wro} + \frac{l_{srr}}{2}\right)\dot{\theta}_{sb} - (\dot{z}_{ur} + l_{drr}\dot{\phi}_{ur})\right] cos\,\alpha_{rlr} \\ V_{drRb} &= \left[\dot{z}_{sb} - l_{ur}\dot{\phi}_{sb} + \left(l_{wro} + \frac{l_{srr}}{2}\right)\dot{\theta}_{sb} - (\dot{z}_{ur} - l_{drr}\dot{\phi}_{ur})\right]\,cos\,\alpha_{rRr} \end{aligned} \tag{2.31}$$

2.2.4 TIRE FORCES

The static force-deflection characteristics of a tire are strongly related to the tire design, static load and inflation pressure. Urban buses encounter considerable variations in the static load due to extreme changes in the number of passengers while in service, it is thus essential to characterize the tire properties over a wide range of loads. In the context of scope of the present study, it is also vital to characterize the force-deflection characteristics as function of the inflation pressure. The measured force-deflection properties of bus tires under various load and inflation pressures were applied to derive a bus tire regression model in inflation pressure and tire deflection in an earlier study [1]. The reported model; given below, is applied in this study:

$$F_t = K_t\, P^a\, \delta_t^b \tag{2.32}$$

Where F_t is the static tire force, P is tire pressure, and K_t, a and b are coefficients derived from the experimental data. The reported study [1] proposed these coefficients as: K_t =2.1666×10^5, a=0.88234591 and b=1.1190674. This model showed good agreements with the experimental data over wide ranges of loads and inflation pressures [1]. The dynamic deflections of the front and rear tires are evaluated from the vertical and roll motions of the unsprung masses, and formulated as:

$$\begin{aligned}
\delta_{tfl} &= -\left(z_{uf} + l_{wfl}\phi_{uf}\right) + z_{gfl} + \delta_{tflo} \\
\delta_{tfR} &= -\left(z_{uf} - l_{wfR}\phi_{uf}\right) + z_{gfR} + \delta_{tfRo} \\
\delta_{trl} &= -\left(z_{ur} + l_{wrl}\phi_{ur}\right) + z_{grl} + \delta_{trlo} \\
\delta_{trR} &= -\left(z_{uf} - l_{wrR}\phi_{ur}\right) + z_{grR} + \delta_{trRo}
\end{aligned} \tag{2.33}$$

Where δ_{tfl}, δ_{tfR}, δ_{trl} and δ_{trR} represent the deflection of the front-left, front-right, rear-left and rear-right tires, respectively. δ_{tflo}, δ_{tfRo}, δ_{trlo} and δ_{trRo} denote static deflection of the front-left, front-right, rear-left and rear-right tires corresponding to a static load supported by the tire, which would vary with the number of passengers. The static deflections are derived from Eq. (2.32), and expressed as:

$$\begin{aligned}
\delta_{tflo} &= e^{\left(\frac{lnF_{tflo} - lnK_t - a\, lnP}{b}\right)} \\
\delta_{tfRo} &= e^{\left(\frac{lnF_{tfRo} - lnK_t - a\, lnP}{b}\right)} \\
\delta_{trlo} &= e^{\left(\frac{lnF_{trlo} - lnK_t - a\, lnP}{b}\right)} \\
\delta_{tfRo} &= e^{\left(\frac{lnF_{trRo} - lnK_t - a\, lnP}{b}\right)}
\end{aligned} \tag{2.34}$$

Where F_{tflo}, F_{tfRo}, F_{trlo} and F_{trRo} are the static tire forces derived from the static equilibrium of the front and rear axle unsprung masses, as:

$$
\begin{aligned}
F_{trlo} &= \frac{m_{sbr}g(l_{wrR}+e)+m_{ur}gl_{wrR}}{l_{wrR}+l_{wrl}} \\
F_{trlo} &= \frac{m_{sbr}g(l_{wrl}-e)+m_{ur}gl_{wrl}}{l_{wrR}+l_{wrl}} \\
F_{tflo} &= \frac{m_{sbf}g(l_{wfR}+e)+m_{uf}gl_{wfR}}{l_{wfR}+l_{wfl}} \\
F_{tfRo} &= \frac{m_{sbf}g(l_{wfl}-e)+m_{uf}gl_{wfl}}{l_{wfR}+l_{wfl}}
\end{aligned}
\tag{2.35}
$$

2.2.5 ANTI-ROLL BAR MOMENT

The rear axle employs an anti-roll bar to enhance the roll stiffness of the vehicle. The roll bar is modeled as a torsional spring constrained between the sprung mass and the rear-axle unsprung mass. The restoring roll moment generated by the anti-roll bar can be expressed as:

$$M_{\phi sur} = k_{\phi}(\phi_{ur} - \phi_{sb}) \tag{2.36}$$

Where k_{φ} is the torsional stiffness of the anti-roll bar.

2.2.6 ROAD PROFILE CHARACTERIZATION

The roughness profiles of various urban roads in Montreal are measured and reported in [5]. The measured profiles describe the elevation in the vicinity of both left and right wheel tracks, including the local grades and abrupt variations. The elevations of the road profiles have been reported at discrete locations with identical intervals of 0.0762 m. The road profiles have been classified under smooth, medium-rough and rough roads on the basis of their roughness index value [1,5]. The measured elevations were filtered to eliminate the contributions of local grades. The nonlinear model simulations in this study are performed in the time-domain employing time-histories of the

displacements of the filtered road profiles. The spatial power spectral densities of these road profiles at right- and left-tracks are reproduced in Figure 2.9.

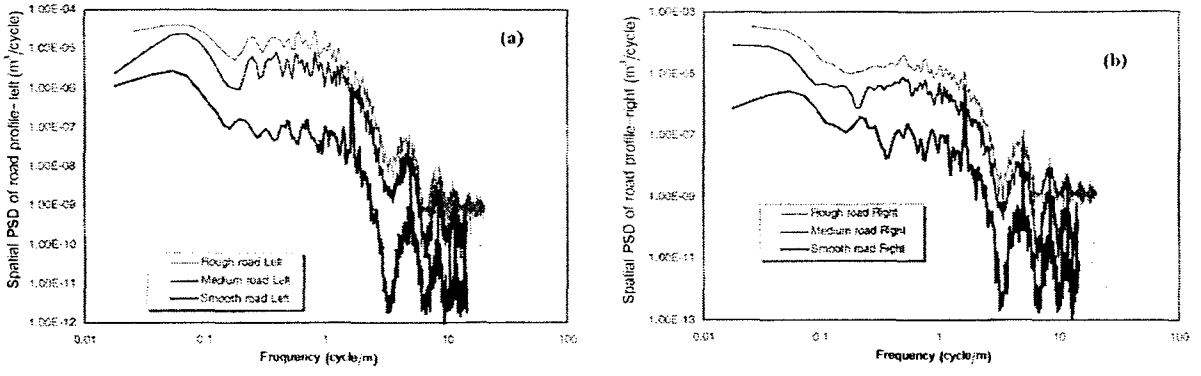

(a) (b)

Figure 2.9: Spatial power spectral density (PSD)of roughness profiles of smooth, medium-rough and rough roads in Montreal: (a) left track and (b) right track [1].

2.3 Simulation Parameters

The dimensional and inertial parameters required to analyze the analytical model of the *Low Floor* bus are identified from the design drawings supplied by the *Nova Bus Corporation* [5]. The estimated inertial parameters are summarized in Table 2.3, while the geometric parameters are presented in Table 2.5, the driver-seat-suspension parameters, reported in [35], are considered in the study, which are summarized in Table 2.4.

Table 2.3: Urban bus inertial parameters according to empty and full loading conditions [1,5].

Parameter	Empty	Full
m_{sb} (kg)	10575	16231
m_{uf} (kg)	575	575
m_{ur} (kg)	1200	1200
$I_{sb\theta}$ ($kg.m^2$)	124194	175034
$I_{sb\varphi}$ ($kg.m^2$)	41370	44163
I_{uf} ($kg.m^2$)	315	315
I_{ur} ($kg.m^2$)	657	657

Table 2.4: Driver-seat-suspension model parameters [35].

Parameter	Value	Parameter	Value
m_o (kg)	50	B (m)	0.05
m_s (kg)	15	K_z (N/m)	4900
k_c (N/m)	40000	V_s (m/s)	0.032
C_c (Ns/m)	150	K_s (N/m)	75000
C_A (Ns/m)	710	F_z (N)	20
C_B (Ns/m)	592		

Table 2.5: Dynamic ride model geometric parameters.

Parameter	Description	Value (m)
l_{sf}	Half the front-axle suspension spring track width	0.663
l_{sr}	Half the rear-axle suspension spring track width	0.86
l_{sff}	Distance between front-axle air springs mounted at same track	0.24
l_{srr}	Distance between rear-axle air springs mounted at same track	1.391
l_{wfo}	Distance from bus c.g to front axle	4.105
l_{wro}	Distance from bus c.g to rear axle	2.095
e	Bus body eccentricity	0.0073
l_{uf}	Lateral distance from front axle c.g to front damper mount fixed to bus body	0.8008
l_{ur}	Lateral distance from rear axle c.g to rear-axle damper mount fixed to bus body	0.7352
l_{df}	Lateral distance from front axle c.g to front-axle damper mount fixed to axle	0.7852
l_{drf}	Lateral distance from rear axle c.g to ahead rear-axle damper mount fixed to axle	0.4651
l_{drr}	Lateral distance from rear axle c.g to behind rear-axle damper mount fixed to axle	0.6435
h_{udf}	Front axle damper mount (to body) height from ground	1.093
h_{df}	Front axle damper mount (to axle) height from ground	0.6072
h_{udrf}	Rear axle damper (ahead) mount (to body) height from ground	0.6797
h_{udrr}	Rear axle damper (rear) mount (to body) height from ground	0.7493
h_{drf}	Rear axle damper (front) mount (to axle) height from ground	0.2269
h_{drr}	Rear axle damper (rear) mount (to axle) height from ground	0.2388
l_{wfl}	Front axle c.g to left-tire contact point	1.0933
l_{wfR}	Front axle c.g to right-tire contact point	1.0933
l_{wrl}	Rear axle c.g to left-tire contact point	0.971
l_{wrR}	Rear axle c.g to right-tire contact point	0.971
h_{sfc}	Front body roll center height with respect to ground	0.508
h_{src}	Rear body roll center height with respect to ground	0.508
h_{ucf}	Front axle roll center height with respect to ground	0.508
h_{ucr}	Rear axle roll center height with respect to ground	0.508
h_{scg}	Bus body c.g height with respect to ground	1.1725
h_{uf}	Front axle c.g height with respect to ground	0.508
h_{ur}	Rear axle c.g height with respect to ground	0.508
a_o	Longitudinal distance from bus body c.g to driver seat location	5.285
b_o	Lateral distance from bus body c.g to driver seat location	0.819

CHAPTER 3

Ride Analysis and Performance Measures

3.1 Introduction

This chapter implements the ride model developed in Chapter 2. Frequency response analysis has been carried out to identify the bounce, roll, and pitch mode natural frequencies of the sprung mass, and the bounce and roll mode natural frequencies of the front and rear axle unsprung masses. For this purpose, the suspension component properties are linearized corresponding to the static loading condition. The ride dynamic responses of the model due to road roughness are derived corresponding to different constant forward speeds, inflation pressures and loading conditions. The influences of variations in tire pressure and passenger load are investigated on the bounce, roll and pitch motions of the sprung and unsprung masses and ride performance measures. The model validity is also examined using experimental data reported in recent study [5].

3.2 Evaluating System Natural Frequencies

The forced response of a dynamic system is directly related to its natural frequencies, which can be evaluated from the free vibration responses of the system. The equations of motion derived in Chapter 2 can be generally as:

$$[M]\{\ddot{q}\} + [K]\{q\} + [C]\{\dot{q}\} = \{0\} \tag{3.1}$$

Where q represents the generalized coordinate vector, M, K and C are the mass, stiffness and damping matrices. The undamped system frequencies are computed from the solution of the following eigen value problem:

$$[[M]^{-1}[K] - \lambda_j I]\{Q\} = \{0\} \tag{3.2}$$

Where I is the identity matrix, λ_j ($j=1,....,N$) denote the eigenvalues, N is the number of DOF and Q denote the corresponding eigen vector. The frequencies of damped oscillations of the model are determined in a similar manner from the eigenvalues of the modified mass matrix [29]:

$$\begin{bmatrix} -M^{-1}C & -M^{-1}K \\ I & 0 \end{bmatrix} \begin{Bmatrix} \dot{q} \\ q \end{Bmatrix} \tag{3.3}$$

The solution of the above (14×14) dynamic matrix yields complex conjugate pairs of eigenvalues of the form:

$$s_i = \alpha_j \mp i\beta_j \tag{3.4}$$

Which yields the frequencies of damped oscillations ω_{dj}, the natural frequency ω_{nj} and the corresponding damping ratios, as:

$$\begin{aligned} \omega_{nj} &= \sqrt{{\alpha_j}^2 + {\beta_j}^2} \\ \omega_{dj} &= |\beta_j| \\ \zeta_j &= -\frac{\alpha_j}{\omega_{nj}} = \sqrt{1 - \left(\frac{\omega_{dj}}{\omega_{nj}}\right)^2} \end{aligned} \tag{3.5}$$

The nonlinear equations of motion, described in Chapter 2, are linearized by considering equivalent stiffness due to suspension and tire at the static equilibrium and damping coefficients at low velocities. The linearized equations are subsequently solved for the unloaded and fully loaded bus models are summarized in Tables 3.1 and 3.2, respectively. It should be noted that linearized suspension and tire properties change with

passengers load. Furthermore, the tire inflation pressure is varied with passenger load, which influences the natural frequencies of the model.

Table 3.1: Natural and damped natural frequencies and damping ratios of the model with no passenger load.

Dominant mode	Natural frequency (Hz)	Damped frequency (Hz)	Damping ratio
Sprung mass bounce Z_s	1.16	1.13	0.198
Sprung mass roll φ_s	0.51	0.51	0.079
Sprung mass pitch θ_s	0.84	0.80	0.290
Front axle unsprung mass bounce Z_{uf}	8.85	8.56	0.254
Front axle unsprung mass roll φ_{uf}	12.95	12.69	0.200
Rear axle unsprung mass bounce Z_{ur}	8.93	8.75	0.199
Rear axle unsprung mass roll φ_{ur}	11.80	11.68	0.145

The results show that the sprung mass bounce mode frequency decreases from 1.16 to 1.1 Hz as the load is increased, while those of unsprung masses increase. The pitch and roll frequencies of the unsprung masses also increase with load, which can be attributed to higher air springs and tire pressures under higher loads. The pitch and roll mode frequencies of the sprung mass vary only slightly with the load, which is attributed to greater mass moments of inertia of the loaded sprung mass and higher suspension stiffness. The damping ratios associated with each mode decreases with increase in the sprung mass since the damping coefficients are held fixed.

Table 3.2: Natural and damped frequencies and damping ratios with corresponding eigenvalues for fully loaded bus.

Dominant Mode	Natural Frequency (Hz)	Damped Frequency (Hz)	Damping Ratio
Sprung mass bounce Z_s	1.10	1.09	0.124
Sprung mass roll φ_s	0.56	0.56	0.064
Sprung mass pitch θ_s	0.82	0.80	0.196
Front axle unsprung mass bounce Z_{uf}	9.27	9.00	0.243
Front axle unsprung mass roll φ_{uf}	13.39	13.13	0.194
Rear axle unsprung mass bounce Z_{ur}	9.41	9.24	0.188
Rear axle unsprung mass roll φ_{ur}	12.32	12.20	0.139

3.3 Frequency Response Characteristics

The frequency response characteristics of the nonlinear ride dynamic model are analyzed to obtain dominant ride frequencies and damping properties of the nonlinear models under two extreme loading conditions: empty and fully loaded. The equations of motion were solved under harmonic excitations at the tire-road interface at several discrete frequencies in the 0.2-16 Hz range. The frequency responses evaluated in terms of rms acceleration transmissibility characteristics in the vertical mode ($\ddot{z}_{sb}/\ddot{z}_o$; $\ddot{z}_{uf}/\ddot{z}_o$; $\ddot{z}_{ur}/\ddot{z}_o$), ($\ddot{\phi}_{sb}/\ddot{z}_o$; $\ddot{\phi}_{uf}/\ddot{z}_o$; $\ddot{\phi}_{ur}/\ddot{z}_o$) and the pitch mode ($\ddot{\theta}_{sb}/\ddot{z}_o$). The harmonic excitations are applied to the four tires with delays in the pitch (τ_p) and roll (τ_r) planes, such that all the vehicle modes are excited:

$$z_{gfl} = z_o sin\omega(t + \tau_p)$$
$$z_{gfR} = z_o sin\omega(t + \tau_p + \tau_r)$$
$$z_{grl} = z_o sin\omega(t) \quad (3.6)$$
$$z_{grR} = z_o sin\omega(t + \tau_r)$$

Where z_o is the amplitude of the input, ω is the frequency of excitation, and z_{gfl}, z_{gfR}, z_{grl} and z_{grR} are displacements of the tire-road interfaces at the left-front, right-front, left-rear and right-rear tires, respectively, as illustrated in Chapter 2. The displacement amplitude z_o is selected to insure continuous contact between the tire and road by inspecting the potential wheel hop near the resonances. The results attained through preliminary simulations revealed presence of wheel hop at excitation amplitudes exceeding 0.009 m. the frequency response analyses were thus performed at z_o=0.008 m, while the delay functions, τ_p and τ_r, were derived from the forward speed V_x, as:

$$\tau_p = \frac{L}{V_x};\ \tau_r = \frac{T_w}{V_x} \quad (3.7)$$

Where L and Tw denote wheel base and track width, respectively.

Figure 3.1 compares the rms vertical acceleration transmissibility of the sprung mass with those of the front and rear unsprung masses in the absence of passenger load. The sprung mass response exhibits dominant peaks near its roll and bounce natural frequency (1.1 Hz) and a small peak near the unsprung masses bounce mode frequencies (approximately 8.4 Hz). While the sprung mass dominant frequencies are close to the natural frequencies of the linearized model, the dominant frequencies of the unsprung masses responses are lower than the identified natural frequencies. The roll and pitch acceleration transmissibility responses of the sprung mass clearly show peaks near the respective resonance frequencies in Figure 3.2, while coupling between the vertical and pitch mode is also evident. The unsprung masses roll responses clearly show dominant peaks near the

sprung and unsprung masses roll frequencies and vertical modes of unsprung masses, as seen in Figure 3.3. Figures 3.4 and 3.5 illustrate the vertical, pitch and roll mode transmissibility responses of the model with full passenger load, and Figures 3.4 and 3.6 show the corresponding vertical and roll responses of unsprung masses. The results suggest that a greater sprung mass causes considerably higher peak transmissibility in all modes, which can be attributed to lower damping ratios under higher sprung mass. It is further seen that the bounce and roll responses of the rear unsprung mass are greater than those of the front unsprung mass, which is again attributable to lower damping properties of the rear axle. The frequency response characteristics, particularly those in the roll and pitch modes are also strongly dependent upon the nature of inputs. Correlations between the inputs at the four wheels, which are related to τ_p and roll τ_r. As an example, Figure 3.7 illustrates comparison of vertical acceleration transmissibility responses of the sprung and unsprung masses to purely vertical excitations (τ_p=τ_r=0).

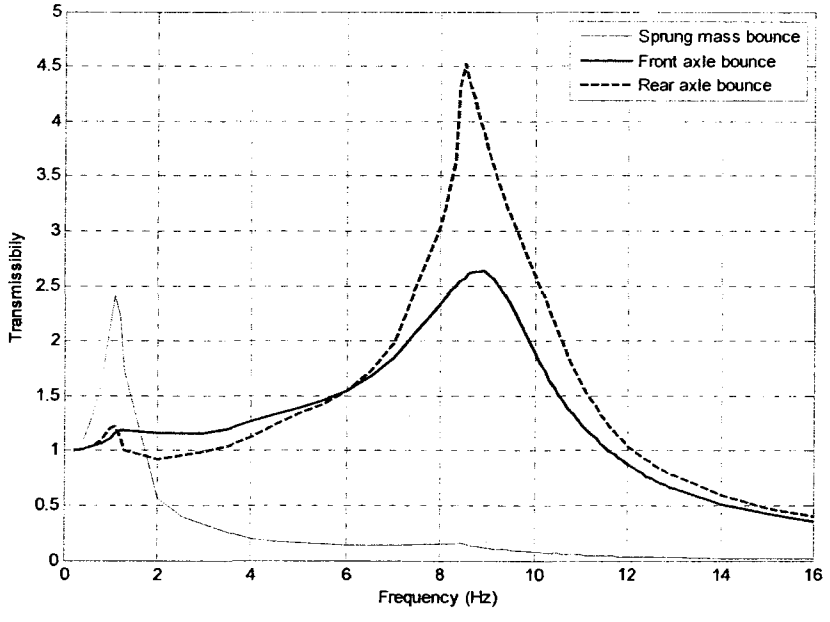

Figure 3.1: Vertical mode acceleration transmissibility of sprung mass ($\ddot{z}_{sb} / \ddot{z}_o$), front axle unsprung mass ($\ddot{z}_{uf} / \ddot{z}_o$) and rear axle unsprung mass ($\ddot{z}_{ur} / \ddot{z}_o$) with no passenger load.

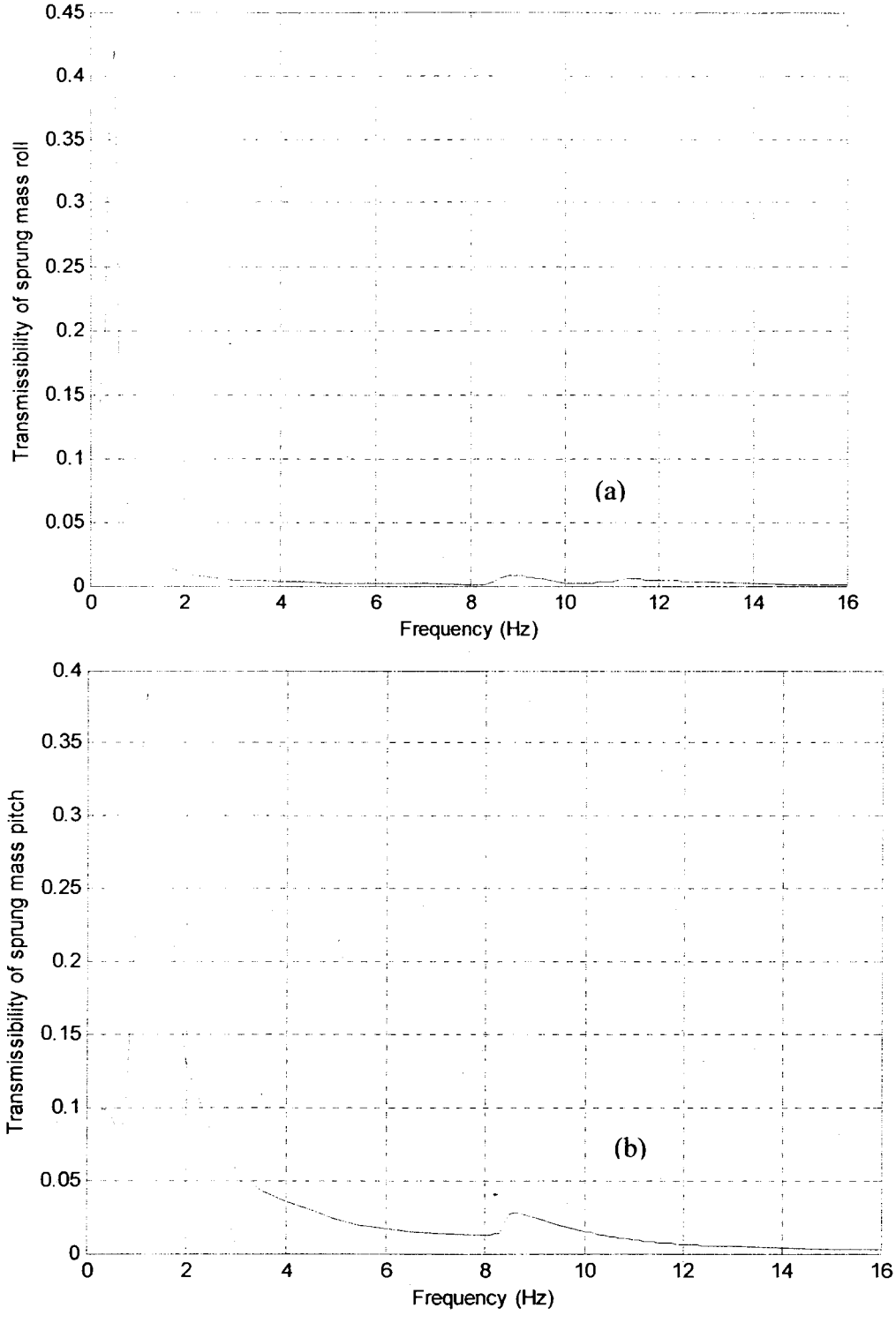

Figure 3.2: The roll and pitch mode acceleration transmissibility of the sprung mass under no passenger load: (a) roll ($\ddot{\phi}_{sb} / \ddot{z}_o$); and (b) pitch acceleration ($\ddot{\theta}_{sb} / \ddot{z}_o$).

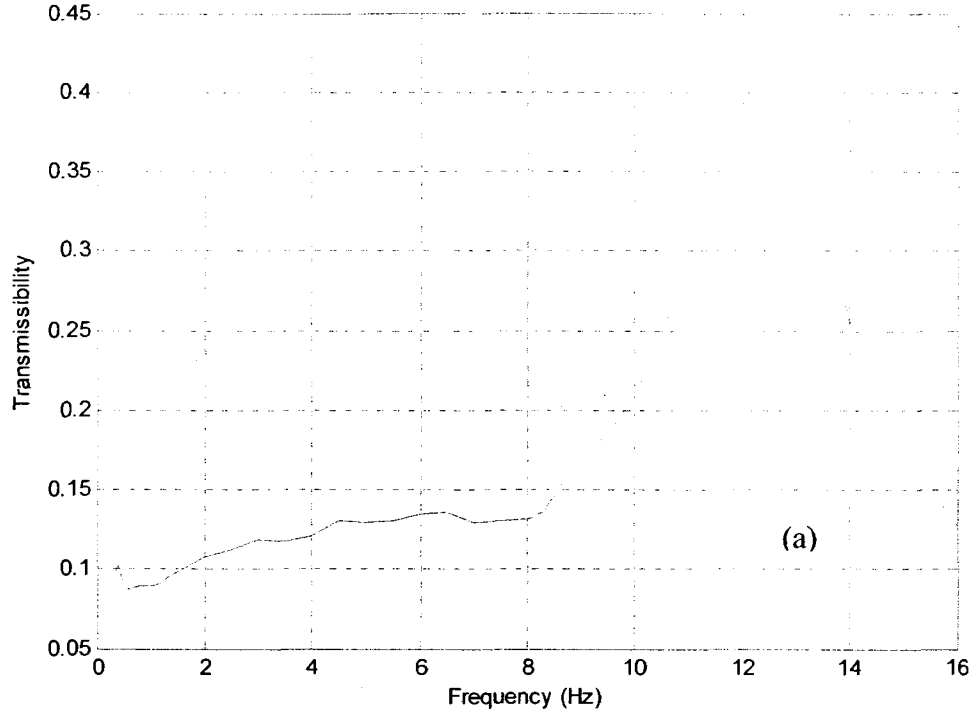

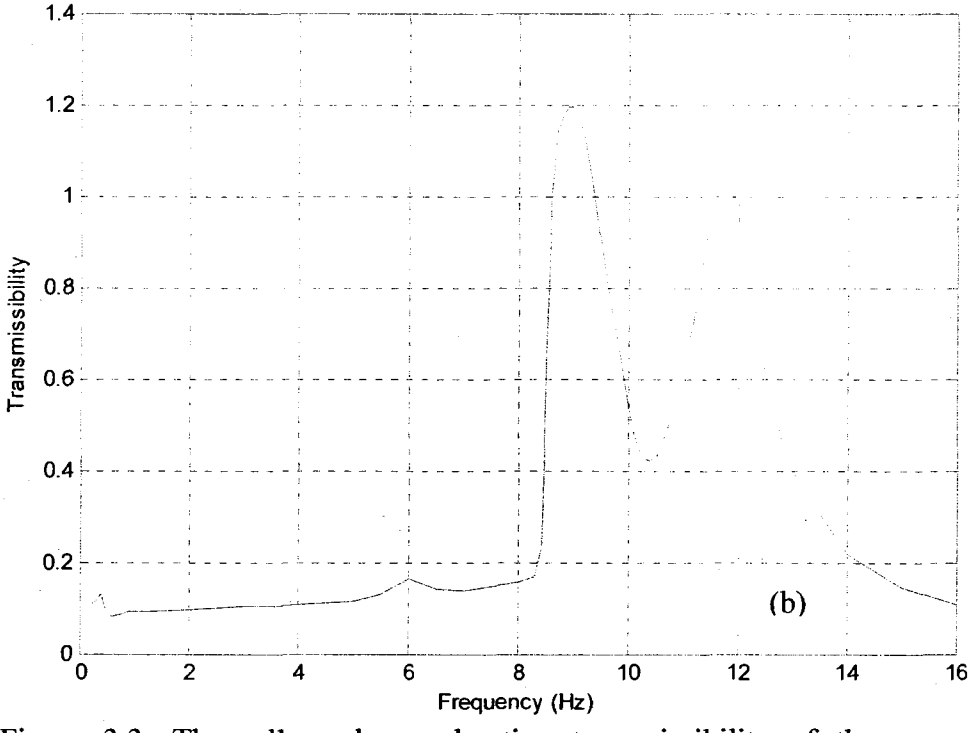

Figure 3.3: The roll mode acceleration transmissibility of the unsprung under no passenger load: (a) front axle $(\ddot{\phi}_{uf} / \ddot{z}_o)$; (b) rear axle $(\ddot{\phi}_{ur} / \ddot{z}_o)$.

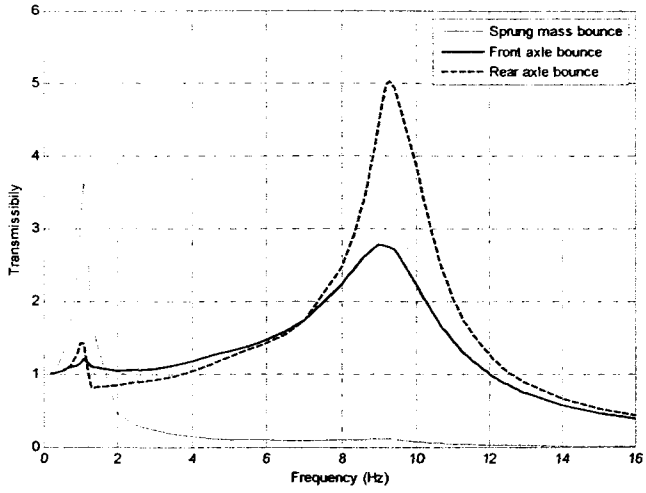

Figure 3.4: Vertical mode acceleration transmissibility of sprung mass $(\ddot{z}_{sb} / \ddot{z}_o)$, front axle unsprung mass $(\ddot{z}_{uf} / \ddot{z}_o)$ and rear axle unsprung mass $(\ddot{z}_{ur} / \ddot{z}_o)$ with full passenger load.

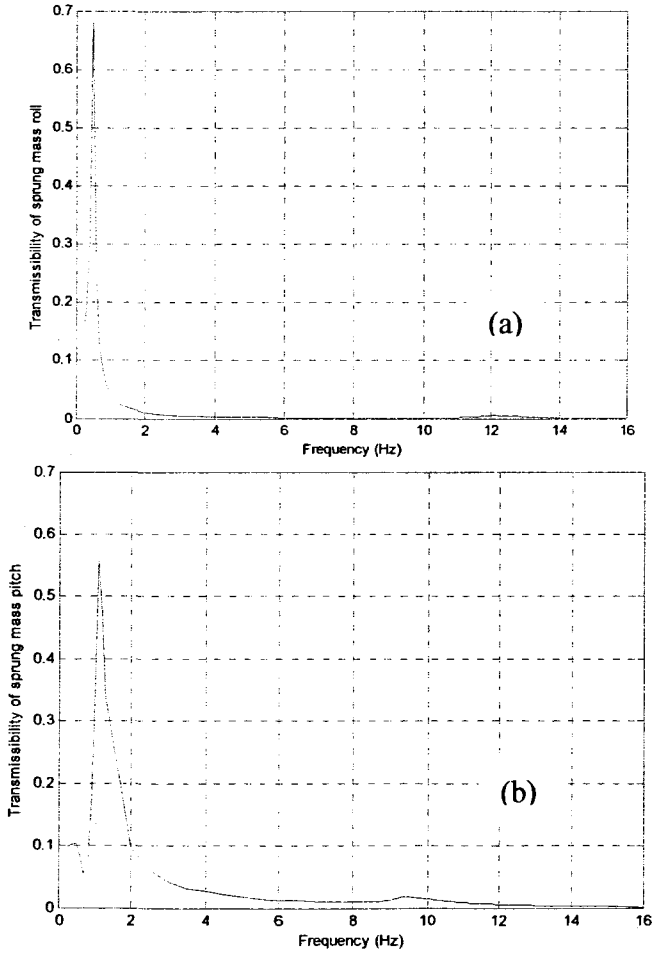

Figure 3.5: The roll and pitch mode acceleration transmissibility of the sprung mass under full passenger load: (a) roll $(\ddot{\phi}_{sb} / \ddot{z}_o)$; and (b) pitch acceleration $(\ddot{\theta}_{sb} / \ddot{z}_o)$.

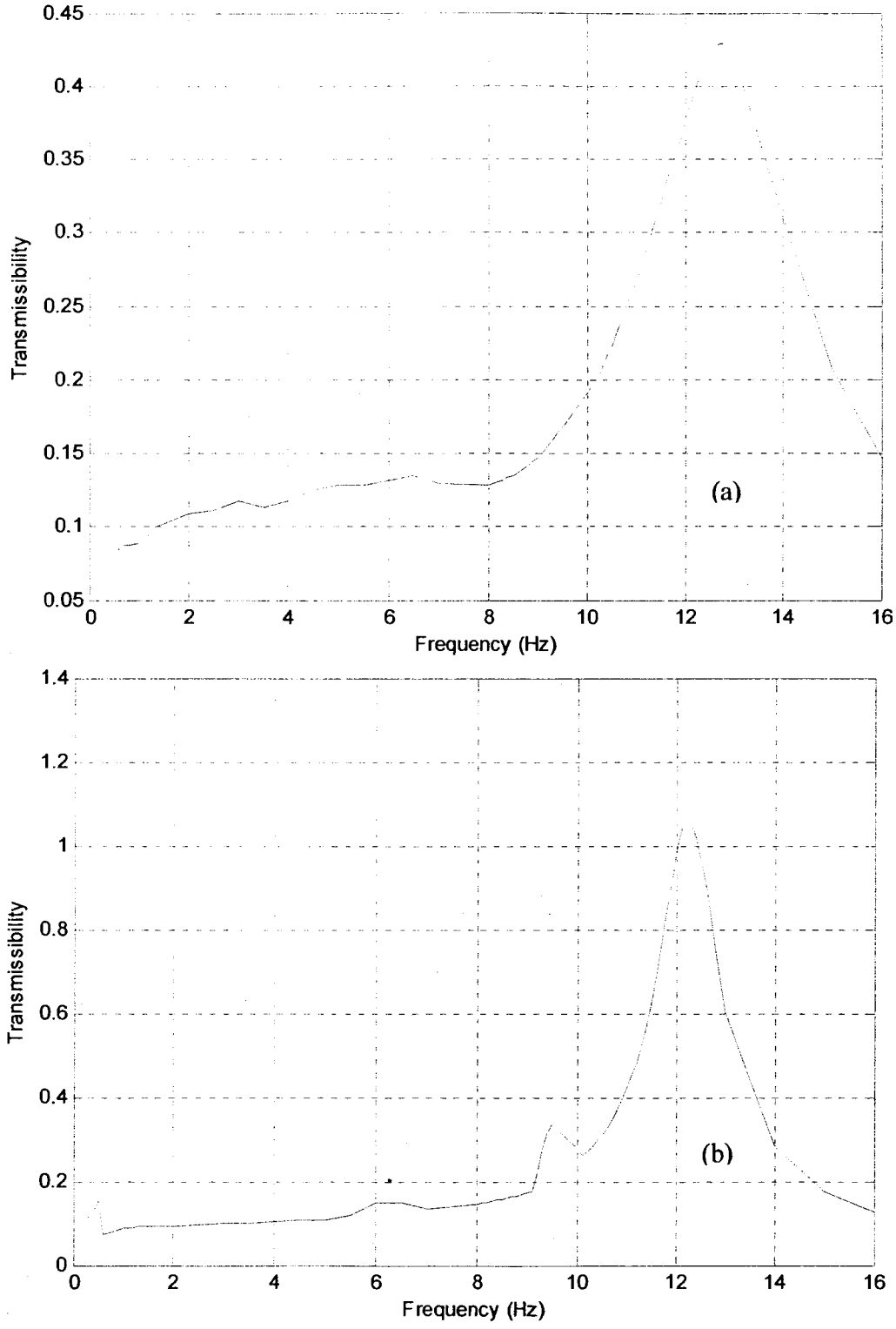

Figure 3.6: The roll mode acceleration transmissibility of the unsprung under full passenger load: (a) front axle $(\ddot{\phi}_{uf} / \ddot{z}_o)$; (b) rear axle $(\ddot{\phi}_{ur} / \ddot{z}_o)$.

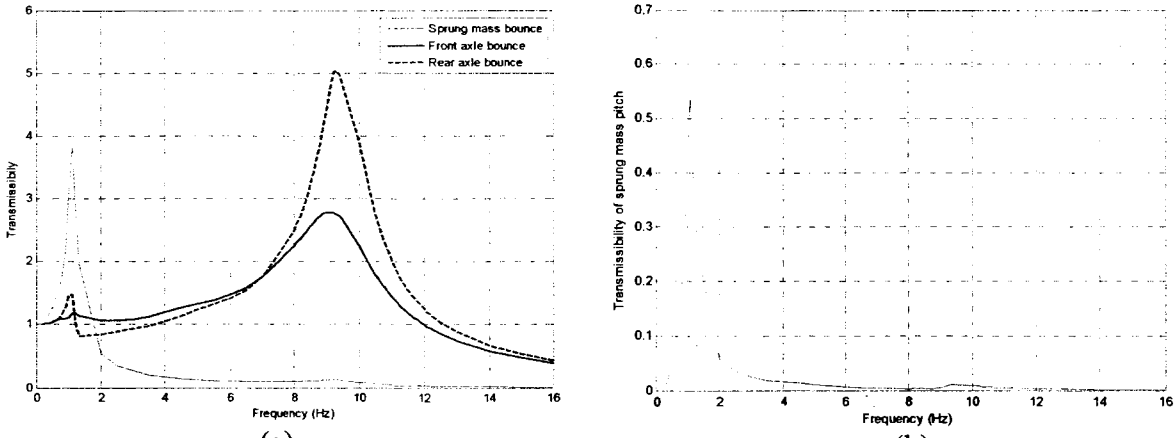

(a) (b)

Figure 3.7: Acceleration transmissibility under full passenger load due to pure bounce excitation of: (a) Vertical mode of sprung mass $(\ddot{z}_{sb} / \ddot{z}_o)$, front axle unsprung mass $(\ddot{z}_{uf} / \ddot{z}_o)$ and rear axle unsprung mass $(\ddot{z}_{ur} / \ddot{z}_o)$; and (b) sprung mass pitch $(\ddot{\theta}_{sb} / \ddot{z}_o)$.

3.4 Performance Measures

The performance measures are defined in view of ride and dynamic pavement loading responses of the vehicle. The ride dynamic responses to excitations arising from randomly distributed road surfaces are evaluated through solutions of differential equations of motion. The Fast Fourier Transform (FFT) is subsequently performed to derive the power spectral density (PSD) of ride and suspension related to selected performance measures are briefly described below.

Dynamic tire force transmitted to the pavement is a key foctor affecting the road damage potential which are evaluated in terms of two measures: (*i*) dynamic load coefficient (DLC) and road stress factor (RS); (*ii*) peak tire forces. The ride dynamic responses are evaluated in terms of rms accelerations of the sprung mass in accordance with ISO-2631-1 [1,5], although the frequency-waitings are not attempted. Those performance measures are briefly described below.

3.4.1 MEASURES RELATED TO TIRE/SUSPENSION FORCES

The dynamic Load Coefficient (*DLC*) is a convenient measure for assessing relative road damage potential of different vehicles configurations, suspension designs and operating conditions [11,26]. The *DLC* describes a statistical measure of variations in the tire force from the mean or static load, such that [5,11]:

$$DLC_j = \frac{\sigma_{Ftj}}{\bar{F}_{FTj}} \tag{3.8}$$

Where σ_{FTj} is the standard deviation of the force due to the tire j and $\bar{F}_{FTj}$ is the mean tire force. The *DLC* is strongly dependent on the road roughness, vehicle speed, vehicle configuration, geometry and mass distribution, axle loads, properties of suspension and tires and vehicle vibration modes. Under normal operating conditions *DLC* typically lies in the 0.1–0.3 range are typical [11], although, Sweatman [8] has reported *DLC* values up to 0.4 for particularly poor tandem suspensions.

The *DLC* has also been related to the road stress factor (*RSF*), the *RSF* is computed assuming that road damage depends on the fourth power of the instantaneous (dynamic) wheel force at a point on the road. Assuming that dynamic wheel forces are normally distributed, Eisenmann [7] showed that the expected value of the fourth power of the instantaneous wheel force can be related to the *RS*, ϕ. For typical highway conditions of roughness and speed, Sweatman [8] has reported the dynamic road stress factor in the 1.11 to 1.46 range depending on the type of suspension system.

The Peak tire force could serve as a good measure for assessing the road damage potential of a vehicle and suspension when the road surface exhibits local discontinuities. Apart from transmitted large magnitude forces to the pavement, the tire-road interactions transmit large magnitudes of dynamic loads to the vehicle chassis leading to fatigue

damage of the structure. The suspension performance is thus defined by its chassis load properties in terms of the chassis load coefficient (*CLC*). The (*CLC*) can serve as a measure of assessing the variation of dynamic loads transmitted to the chassis in a manner similar to the *DLC*. The *CLC* is defined as the ratio of the rms dynamic suspension force transmitted to the chassis at its support to the static load supported by the suspension and expressed as:

$$CLC = \frac{P_{sd}}{P_{so}} \tag{3.9}$$

Where P_{sd} is the rms variation in the dynamic suspension force and P_{so} is the static load supported by suspension springs.

3.4.2 MEASURES RELATED TO RIDE PERFORMANCE

The vibration comfort of human occupants in a vehicle has been directly related to magnitudes of transmitted vibration [5,11]. The ride performance of the vehicle model is thus evaluated in terms of rms values of vertical, pitch and roll accelerations of the bus (sprung mass), formulated as:

$$(\ddot{z}_{sb})_{rms} = \sqrt{\frac{1}{T}\int_0^T \ddot{z}_{sb}{}^2\, dt} \;;\; (\ddot{\phi}_{sb})_{rms} = \sqrt{\frac{1}{T}\int_0^T \ddot{\phi}_{sb}{}^2\, dt}$$
$$(\ddot{\theta}_{sb})_{rms} = \sqrt{\frac{1}{T}\int_0^T \ddot{\theta}_{sb}{}^2\, dt} \tag{3.10}$$

Where $(\ddot{z}_{sb})_{rms}$, $(\ddot{\phi}_{sb})_{rms}$ and $(\ddot{\theta}_{sb})_{rms}$ are the vertical, roll and pitch rms accelerations, respectively, and T is the observation period.

3.5 Ride Dynamic Responses of the Vehicle Model

The ride and pavement load responses of the vehicle model are evaluated under different loads and the tire pressures to study their influences on the responses. The responses are evaluated under excitations from a rough urban road (CDN) and forward speed of 50 km/h, while the nominal tire pressure is taken as (100 psi). The influences of variations in operating load and tire pressure are presented and discussed in the following subsections.

3.5.1 INFLUENCE OF OPERATING LOAD

Table 3.3 summarizes the effect of variations in operating passenger load on the ride and tire force performance measures. The analyses are performed for three load conditions: (*i*) empty-no passenger load (m_{sb}=10575 kg); (*ii*) half-full-40passengers (m_{sb}=13403 kg); and (*iii*) full load-80 passengers (m_{sb}=16231 kg). The tire pressure is held constant at 689.48 kPa (100 psi) under all three load conditions, which represents the current operating practice. The ride responses are presented in terms of vertical, roll and pitch rms accelerations, while the tire forces are expressed in terms of *DLC* due to all four tires (DLC_{fl}, DLC_{fR}, DLC_{rl}, DLC_{rR}) and peak forces due to individual tires. The rms vertical and roll acceleration responses of the front and rear axles are also presented together with the chassis load coefficient (*CLC*) due to front and rear right track suspensions. The results show that rms values of body vertical and pitch accelerations increase when the passenger load diminishes, while the body roll acceleration decrease slightly.

Table 3.3: Influence of operating load on the ride and tire force related performance measures (CDN road; 100 psi; 50 km/h).

Performance Measure	Operating load		
	Empty	Half	Full
$(\ddot{z}_{sb})_{rms}$ m/s^2	0.72	0.69	0.69
$(\ddot{\phi}_{sb})_{rms}$ rad/s^2	0.10	0.11	0.13
$(\ddot{\theta}_{s})_{rms}$ rad/s^2	0.19	0.19	0.19
$(\ddot{z}_{uf})_{rms}$ m/s^2	8.46	8.65	8.81
$(\ddot{\phi}_{uf})_{rms}$ rad/s^2	13.63	13.99	14.27
$(\ddot{z}_{ur})_{rms}$ m /s^2	11.49	11.81	12.01
$(\ddot{\phi}_{ur})_{rms}$ rad/s^2	22.76	23.19	23.49
DLC_{fl}	0.15	0.13	0.11
DLC_{fR}	0.20	0.16	0.14
DLC_{rl}	0.23	0.20	0.18
DLC_{rR}	0.26	0.22	0.19
CLC_{fR}	0.13	0.11	0.10
CLC_{rR}	0.14	0.13	0.13
$(Ft_{fl})_{max}$ kN	25.37	27.32	28.61
$(Ft_{fR})_{max}$ kN	36.28	36.06	35.68
$(Ft_{rl})_{max}$ kN	64.10	62.56	64.97
$(Ft_{rR})_{max}$ kN	84.20	88.39	90.68

3.5.2 INFLUENCE OF VEHICLE SPEED

The ride and pavement load responses to rough load excitations are strongly influenced by the vehicle speed. The effect of vehicle speed is thus investigated by considering three different speeds: 30, 50 and 70 km/h. The model analysis in this case is limited to half-full passenger load and nominal tire pressure (689.48 kPa). Table 3.4 summarizes the effect of vehicle speed on the responses in terms of ride and tire load measures. The results clearly show that the most significant effect of vehicle speed on all the response measures. The rms vertical, roll and pitch accelerations responses of the bus

body increase considerably with increasing vehicle speed. It is observed that the rms vertical and pitch acceleration nearly double when vehicle speed is increased from 30 to 70 km/h, while the corresponding increase in roll acceleration is quite small. The magnitudes of vertical and roll rms accelerations of the axles also increase considerably with increasing vehicle speed. The dynamic load coefficients for all tires at 70 km/h are nearly twice those at 30 km/h, although the relative effect on peak tire forces is relatively small. It should be noticed that the peak dynamic tire forces are higher for right side of the track since the right track of the road was relatively more rough compared to the left track.

Table 3.4: Influence of operating speed on the ride and tire force related performance measures (CDN road; half load; 100 psi).

Performance Measure	Operating Speed (km/hr)		
	30	50	70
$(\ddot{z}_{sb})_{rms}$ m/s^2	0.49	0.69	1.00
$(\ddot{\phi}_{sb})_{rms}$ rad/s^2	0.10	0.11	0.12
$(\ddot{\theta}_{s})_{rms}$ rad/s^2	0.11	0.19	0.24
$(\ddot{z}_{uf})_{rms}$ m/s^2	5.57	8.65	11.46
$(\ddot{\phi}_{uf})_{rms}$ rad/s^2	8.71	13.99	19.84
$(\ddot{z}_{ur})_{rms}$ m /s^2	7.67	11.81	15.00
$(\ddot{\phi}_{ur})_{rms}$ rad/s^2	14.12	23.19	29.88
DLC_{fl}	0.08	0.13	0.17
DLC_{fR}	0.10	0.16	0.21
DLC_{rl}	0.13	0.20	0.26
DLC_{rR}	0.14	0.22	0.28
CLC_{fR}	0.08	0.11	0.13
CLC_{rR}	0.09	0.13	0.17
$(Ft_{fl})_{max}$ kN	22.69	27.32	27.59
$(Ft_{fR})_{max}$ kN	33.77	36.06	39.08
$(Ft_{rl})_{max}$ kN	56.54	62.56	62.96
$(Ft_{rR})_{max}$ kN	69.50	88.39	89.79

3.5.3 INFLUENCE OF ROAD ROUGHNESS

Road roughness is one of the most important factors influencing the vehicle performance measures. Urban roads generally exhibit greater roughness than the highway surfaces. Furthermore, urban road surfaces may comprise distinct irregularities due to drain covers and pot holes. The road roughness effect on the performance measures is investigated by considering excitations due to three different road roughness profiles termed as smooth, medium-rough and rough, as described in section 2.2. The analyses are performed assuming no passenger load, forward speed of 50 km/hr and nominal tire pressure of 689.48 kPa. The ride and tire-force related measures illustrating the effect of road roughness are summarized in Table 3.5. These results clearly show that all the response measures increase considerably with increasing road roughness. The results suggest that the road and the vehicle form a closed-loop coupled system. Vehicle vibration contributes to determination of road roughness due to large magnitude of dynamic wheel loads. The resulting greater roughness of the road surface causes even large magnitudes of vibration leading to further increase in the surface roughness.

Table 3.5: Influence of road roughness on the performance measures (empty load,50 km/hr, 100 psi).

Performance Measure	Road Roughness		
	Smooth	Medium	Rough
$(\ddot{z}_{sb})_{rms}$ m/s^2	0.4089	0.6198	0.7195
$(\ddot{\phi}_{sb})_{rms}$ rad/s^2	0.0734	0.0822	0.1039
$(\ddot{\theta}_s)_{rms}$ rad/s^2	0.1113	0.1584	0.1948
$(\ddot{z}_{uf})_{rms}$ m/s^2	4.0035	5.1979	8.4566
$(\ddot{\phi}_{uf})_{rms}$ rad/s^2	4.4538	8.4610	13.6254
$(\ddot{z}_{ur})_{rms}$ m /s^2	5.328	7.1537	11.4889
$(\ddot{\phi}_{ur})_{rms}$ rad/s^2	6.836	13.3065	22.7562
DLC_{fl}	0.0761	0.1156	0.1546
DLC_{fR}	0.091	0.1234	0.1953
DLC_{rl}	0.1047	0.1614	0.2294
DLC_{rR}	0.1105	0.1632	0.2561
CLC_{fR}	0.0714	0.0970	0.1291
CLC_{rR}	0.0779	0.1091	0.1361
$(Ft_{fl})_{max}$ kN	21.9762	22.8137	25.3666
$(Ft_{fR})_{max}$ kN	29.3173	31.6312	36.2789
$(Ft_{rl})_{max}$ kN	41.9124	48.7225	64.1045
$(Ft_{rR})_{max}$ kN	65.3298	43.3465	84.1982

3.5.4 INFLATION PRESSURE EFFECT ON THE PERFORMANCE MEASURES

The vehicle ride responses are related to stiffness properties of the tires apart from many other design and operating factors. The Vertical tire stiffness is strongly dependent on the inflation pressure as previously discussed in Section 2.2. A lower inflation pressure would yield lower vertical tire stiffness and thus lower dynamic tire force arising from tire-pavement interaction and lower contact pressure as a result of increased length of the contact patch. A lower pressure, however, may cause rapid tire wear. Considering

that the tire pressure ratings are designed for peak operating load, a lower operating pressure may be selected under lighter passenger load that causes comparable tire deformation and thus the wear rate. The influence of inflation pressure variations on the vehicle performance measures are thus analyzed by carefully selecting the tire pressure corresponding to different load conditions: empty and half-full the analyses are performed for one road-roughness excitations (CDN), while the forward speed is taken as 50 km/h. The effects of inflation pressure on the smooth and medium rough roads are analyzed only under medium loading condition at the same forward speed. Tables 3.6 and 3.7 summarize the effects of inflation pressure on the ride and tire force related measures of the vehicle subject to rough road excitation, and empty and half loading conditions, respectively. The results show that the magnitudes of rms vertical acceleration of the bus body increased by 10 and 7.78 % as the pressure increased from 75 to 120 psi at empty and half loading conditions, respectively. The rms roll and pitch accelerations of the bus body also increases slightly, around 6%, as the tire pressure increases from 75 to 120 psi. The dynamic load coefficients of the front-left, front-right, rear-left and rear-right also increase by 31.2, 28.1, 34.1 and 34.1%, respectively, under the considered pressure increase (75 to 120 psi) for the empty bus. The corresponding percentage increase in the dynamic load coefficients at half loading condition are 30.6, 27.98, 32.05 and 32.6%, respectively.

Table 3.6: Influence of inflation pressure on the vehicle performance measures of the bus (CDN road; empty load; 50 km/h).

Performance Measure	Inflation Pressure (psi)				
	75	90	100	110	120
$(\ddot{z}_{sb})_{rms}$ m/s^2	0.68	0.70	0.72	0.73	0.74
$(\ddot{\phi}_{sb})_{rms}$ rad/s^2	0.10	0.10	0.10	0.10	0.11
$(\ddot{\theta}_{s})_{rms}$ rad/s^2	0.19	0.19	0.19	0.20	0.20
$(\ddot{z}_{uf})_{rms}$ m/s^2	6.82	7.79	8.46	9.12	9.76
$(\ddot{\phi}_{uf})_{rms}$ rad/s^2	11.54	12.84	13.63	14.35	15.08
$(\ddot{z}_{ur})_{rms}$ m /s^2	9.02	10.56	11.49	12.25	12.94
$(\ddot{\phi}_{ur})_{rms}$ rad/s^2	19.13	21.24	22.76	23.88	24.65
DLC_{fl}	0.13	0.15	0.15	0.16	0.17
DLC_{fR}	0.17	0.18	0.20	0.21	0.22
DLC_{rl}	0.19	0.21	0.23	0.24	0.25
DLC_{rR}	0.21	0.24	0.26	0.27	0.28
CLC_{fR}	0.12	0.13	0.13	0.13	0.13
CLC_{rR}	0.13	0.13	0.14	0.14	0.14
$(Ft_{fl})_{max}$ kN	18.34	22.50	25.37	27.97	30.37
$(Ft_{fR})_{max}$ kN	30.23	33.50	36.28	39.05	42.08
$(Ft_{rl})_{max}$ kN	52.07	60.07	64.10	65.76	73.80
$(Ft_{rR})_{max}$ kN	62.61	69.73	84.20	93.73	93.19

Table 3.7: Influence of inflation pressure on the vehicle performance measures of the bus (CDN road; half load; 50 km/h).

Performance Measures	Inflation Pressure (psi)				
	75	90	100	110	120
$(\ddot{z}_{sb})_{rms}$ m/s^2	0.66	0.68	0.69	0.70	0.71
$(\ddot{\phi}_{sb})_{rms}$ rad/s^2	0.11	0.11	0.11	0.12	0.12
$(\ddot{\theta}_{s})_{rms}$ rad/s^2	0.18	0.19	0.19	0.19	0.19
$(\ddot{z}_{uf})_{rms}$ m/s^2	6.96	7.96	8.65	9.33	9.98
$(\ddot{\phi}_{uf})_{rms}$ rad/s^2	11.83	13.18	13.99	14.80	15.64
$(\ddot{z}_{ur})_{rms}$ m /s^2	9.35	10.90	11.81	12.56	13.31
$(\ddot{\phi}_{ur})_{rms}$ rad/s^2	19.49	21.81	23.19	24.30	25.43
Driver body rms vertical acceleration m/s^2	0.81	0.83	0.85	0.86	0.88
DLC_{fl}	0.11	0.12	0.13	0.14	0.14
DLC_{fR}	0.14	0.15	0.16	0.17	0.18
DLC_{rl}	0.17	0.19	0.20	0.21	0.22
DLC_{rR}	0.18	0.21	0.22	0.23	0.24
CLC_{fR}	0.10	0.10	0.11	0.11	0.11
CLC_{rR}	0.12	0.13	0.13	0.13	0.13
$(Ft_{fl})_{max}$ kN	19.41	24.35	27.32	30.20	32.52
$(Ft_{fR})_{max}$ kN	29.38	33.06	36.06	38.91	42.07
$(Ft_{rl})_{max}$ kN	53.18	58.40	62.56	71.85	78.65
$(Ft_{rR})_{max}$ kN	61.65	75.78	88.39	92.69	87.85

Tables 3.8 and 3.9 summarize the effects of the inflation pressure on selected vehicle responses to excitations arising from medium-rough (SAP) and smooth (RTS) roads, respectively. The results are obtained under half loading conditions and forward speed of 50 km/h. The results show the same trend where all the performance measures increase with tire pressure. The sprung mass acceleration responses increase by nearly 3.30 and 0.6 %, when the tire pressure is increased from 75 to 120 psi for the SAP and RTS roads, respectively. The corresponding increases in the DLC are most notable, for the medium-rough (SAP) road. The results clearly suggest that operating under constant tire inflation

pressure is detrimental to both driver/passenger ride comfort and dynamic loads transmitted to urban roads, when the bus is slightly loaded.

Table 3.8: Influence of inflation pressure on the vehicle performance measures of the bus (SAP road; half load; 50 km/h).

Performance Measures	Inflation Pressure (psi)				
	75	90	100	110	120
$(\ddot{z}_{sb})_{rms}$ m/s^2	0.60	0.61	0.61	0.61	0.62
$(\ddot{\phi}_{sb})_{rms}$ rad/s^2	0.09	0.09	0.09	0.09	0.10
$(\ddot{\theta}_s)_{rms}$ rad/s^2	0.15	0.16	0.16	0.16	0.16
$(\ddot{z}_{uf})_{rms}$ m/s^2	4.27	4.89	5.30	5.71	6.10
$(\ddot{\phi}_{uf})_{rms}$ rad/s^2	7.02	8.02	8.69	9.38	10.09
$(\ddot{z}_{ur})_{rms}$ m /s^2	5.97	6.79	7.32	7.84	8.38
$(\ddot{\phi}_{ur})_{rms}$ rad/s^2	11.79	12.71	13.53	14.50	15.56
Driver body rms vertical acceleration m/s^2	0.62	0.63	0.64	0.65	0.65
DLC_{fl}	0.08	0.09	0.10	0.10	0.11
DLC_{fR}	0.09	0.10	0.10	0.11	0.11
DLC_{rl}	0.13	0.14	0.14	0.15	0.16
DLC_{rR}	0.13	0.14	0.14	0.15	0.16
CLC_{fR}	0.08	0.08	0.08	0.08	0.08
CLC_{rR}	0.10	0.11	0.11	0.11	0.11
$(Ft_{fl})_{max}$ kN	12.67	14.14	14.70	15.78	17.36
$(Ft_{fR})_{max}$ kN	19.33	21.12	22.18	23.90	25.68
$(Ft_{rl})_{max}$ kN	33.81	41.20	43.67	45.59	50.45
$(Ft_{rR})_{max}$ kN	44.72	48.01	49.15	48.77	52.13

Tables 3.6 to 3.9 also present the influence of variations in tire pressure on the rms vertical acceleration transmitted to the driver mass. This measure directly related to the driver exposure to vertical vibration when the recommended w_k frequency-weighting is applied [1]. This study focuses on un-weighted rms vertical acceleration in order to assess

relative effects of the tire inflation pressure on the magnitudes of transmitted vibration. It also needs to be emphasized that magnitude of diver mass acceleration will also depend on properties of suspension at the seat. The results suggest that lowering tire pressure would help reduce the rms vertical acceleration of the drive mass. The lower tire pressure may yield grater benefit in attenuating the shock motion caused by irregularities in the road surface, which are not investigated in the study.

Table 3.9: Influence of inflation pressure on the vehicle performance measures of the bus (RTS road; half load; 50 km/h).

Performance Measure	Inflation Pressure (psi)				
	75	90	100	110	120
$(\ddot{z}_{sb})_{rms}$ m/s2	0.41	0.41	0.41	0.41	0.41
$(\ddot{\phi}_{sb})_{rms}$ rad/s^2	0.09	0.09	0.09	0.09	0.09
$(\ddot{\theta}_{s})_{rms}$ rad/s^2	0.11	0.11	0.11	0.11	0.11
$(\ddot{z}_{uf})_{rms}$ m/s2	3.33	3.77	4.05	4.33	4.61
$(\ddot{\phi}_{uf})_{rms}$ rad/s^2	3.88	4.28	4.53	4.78	5.01
$(\ddot{z}_{ur})_{rms}$ m /s^2	4.45	5.03	5.40	5.75	6.10
$(\ddot{\phi}_{ur})_{rms}$ rad/s^2	6.09	6.58	6.92	7.31	7.78
Driver body rms vertical acceleration m/s^2	0.49	0.50	0.50	0.50	0.50
DLC_{fl}	0.06	0.06	0.06	0.07	0.07
DLC_{fR}	0.07	0.07	0.08	0.08	0.08
DLC_{rl}	0.09	0.09	0.10	0.10	0.10
DLC_{rR}	0.09	0.10	0.10	0.10	0.11
CLC_{fR}	0.06	0.06	0.06	0.06	0.06
CLC_{rR}	0.08	0.08	0.08	0.08	0.08
$(Ft_{fl})_{max}$ kN	17.98	20.35	22.08	23.88	25.77
$(Ft_{fR})_{max}$ kN	28.56	32.63	35.21	37.68	40.13
$(Ft_{rl})_{max}$ kN	36.79	40.37	43.49	47.53	52.00
$(Ft_{rR})_{max}$ kN	51.78	60.06	65.52	70.86	76.44

The effect inflation pressure on the driver body vertical acceleration is thoroughly investigated under excitations arising from the three classified roads at half loading

conditions while the forward speed is taken as 50 km/h. For the CDN road, the driver body vertical acceleration rises from 0.81 to 0.88 m/s^2 as the pressure increases from 75 to 120 psi, the percentage of increase is thus 8.37%, as illustrated in Table 3.7.

For the SAP road, the percentage of increase is 6.06%, as illustrated in Table 3.8, the value of acceleration increases from 0.62 to 0.65 m/s^2 as pressure increases from 75 to 120 psi, while the percentage of increase of driver body vertical acceleration is 2.85 % since it increases from 0.4908 to 0.5048 m/s^2. Based on these results it is clearly evident that magnitudes of transmitted vibrations increases with tire pressure increase, and the percentage of increase is higher for rough road.

3.6 Validation of the Bus Model

The governing equations of motion of the vehicle model are solved under excitations arising from road profiles of different roads in Montreal. The roughness profiles of each road have been defined in the vicinity of left- and right-tracks [5]. The analyses are performed under different loading conditions, constant forward speeds and inflation pressures. The resulting responses are expressed in terms of PSD of accelerations of the sprung and unsprung masses. The model results are compared with reported field measurement data [5] to examine the model validity. Owing to variations in forward speed, road conditions and passenger load, the measured data, in most cases describe the ranges of acceleration PSD and mean values computed over a number of runs on a particular road. The model responses are evaluated at a forward speed of 50 km/h and nominal tire pressure.

Figure 3.8 (a) illustrates comparison of PSD of vertical bus body acceleration response of the model with the mean measured data, the simulations were performed

under a relatively rough road excitations (CDN: Cote-des-Neiges). The PSD of vertical acceleration response at the driver seat location is compared with the ranges of measured data in Figure 3.8 (b). Figure 3.9 illustrates comparisons of the vertical acceleration responses to excitations from a relatively smoother road (SAP: Saint-Patrick) with corresponding measured data. The comparisons in general show reasonably good agreement between the model and measured results. The model responses and measured data exhibit clear peaks in the vicinity of sprung and unsprung masses frequencies near 1 Hz and 8.5-9 Hz, apart from other peaks near the axle roll natural frequencies. The model responses at the driver seat, however, differ considerably from the measured data. The acceleration response at the seat peak near 1 Hz, while the measured data exhibits peaks near roll/pitch (0.5-0.9) and vertical mode frequencies (1.5 Hz) of the vehicle. Furthermore, the magnitudes of computed seat response are generally lower than the measured data, particularly at frequencies above 2 Hz. Such deviations between the measured and computed results could be attributed to many factors, including: (*i*) consideration of the simplified occupant-seat model with occupant represented by a rigid mass; (*ii*) lack of consideration of the particular suspension seat used in the test vehicle; (*iii*) possible differences in roughness characteristics of the test road and the road surfaces considered in the simulation; and (*iv*) variations of the forward speed of the test bus during measurements.

Figures 3.10 and 3.11 show comparisons of sprung mass pitch and roll acceleration PSD responses of the model with the range of measured data for relatively rough and smooth road excitations, respectively. The model responses exhibit trends are in reasonably good agreement with the measured data, although considerable deviations

are evident in the magnitudes. These deviations are attributable the above-stated factors. The lack of consideration of dynamic tire stiffness, which is a combined function of speed and inflation pressure, together with the flexural bending mode of the bus bending frame are also expected to contribute to errors. Figures 3.12 and 3.13 compare the vertical and roll acceleration PSD responses, respectively, of the unsprung masses of the vehicle model subject to rough road excitations (CDN) with the measured data. The comparison of vertical and roll unsprung masses responses to excitations due to SAP with the measured data are presented in Figures 3.14 and 3.15, respectively. The results again show reasonably good agreement between the model and responses, although considerable deviation can be observed between the two at higher frequencies above 30 Hz. These deviations are most likely attributed to flexibility of the bus frame and axle components, which are not considered in the model.

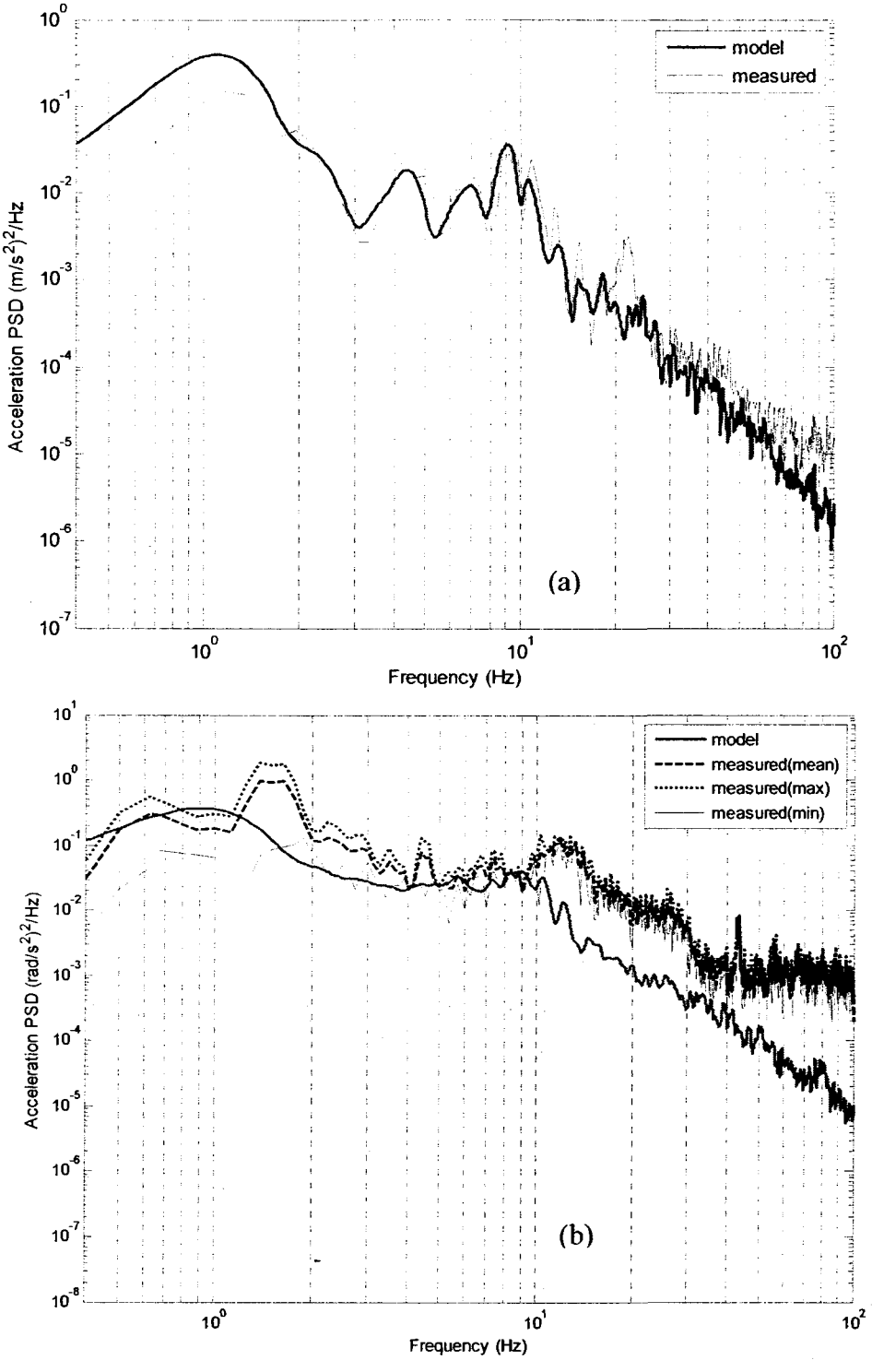

Figure 3.8: Comparison of vertical acceleration PSD responses of the model with the measured data bus body (CDN road, 50 km/h): (a) sprung mass vertical acceleration; and (b) vertical acceleration at the driver seat.

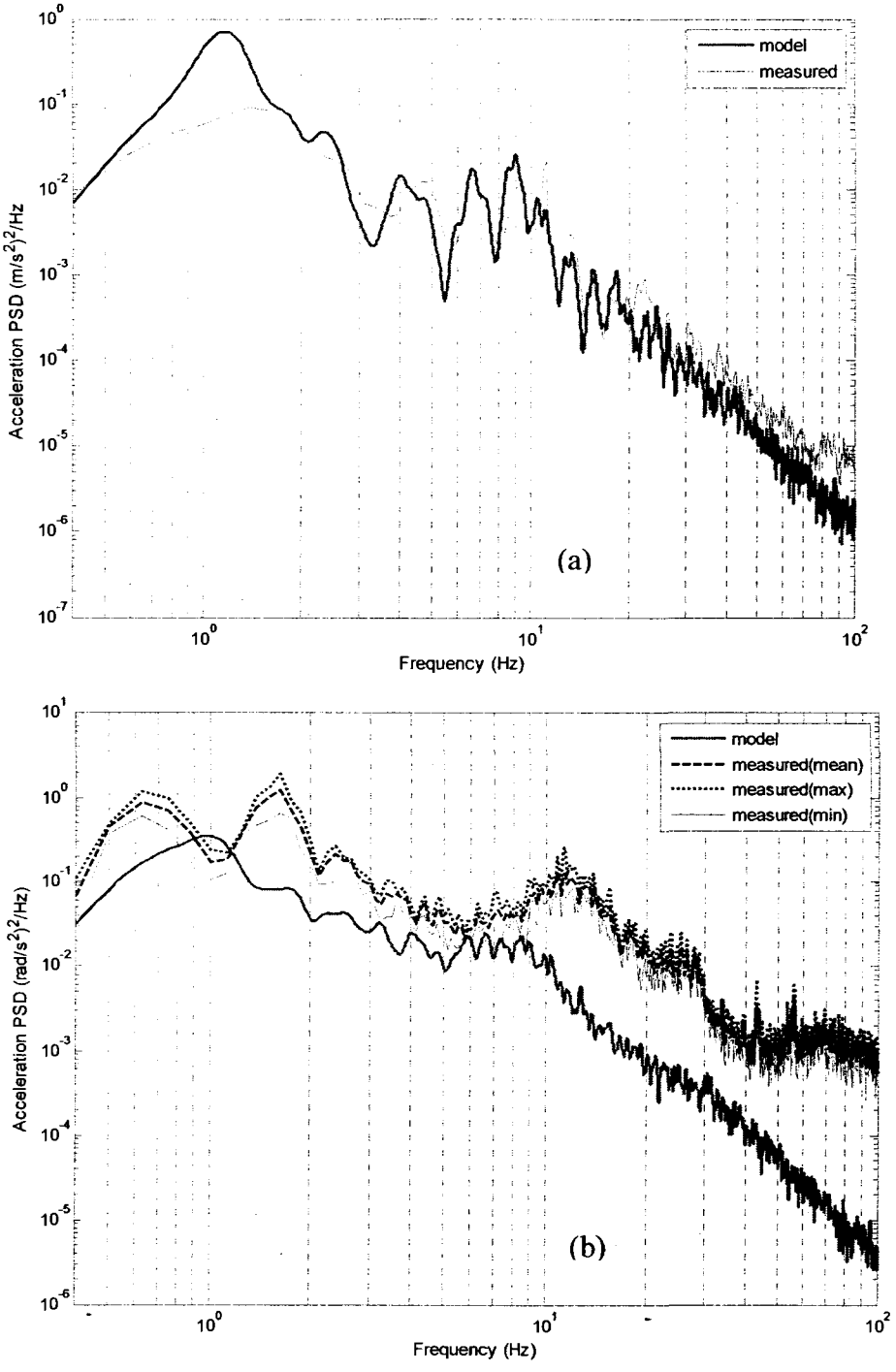

Figure 3.9: Comparison of vertical acceleration PSD responses of the model with the measured data bus body (SAP road, 50 km/h): (a) sprung mass vertical acceleration; and (b) vertical acceleration at the driver seat.

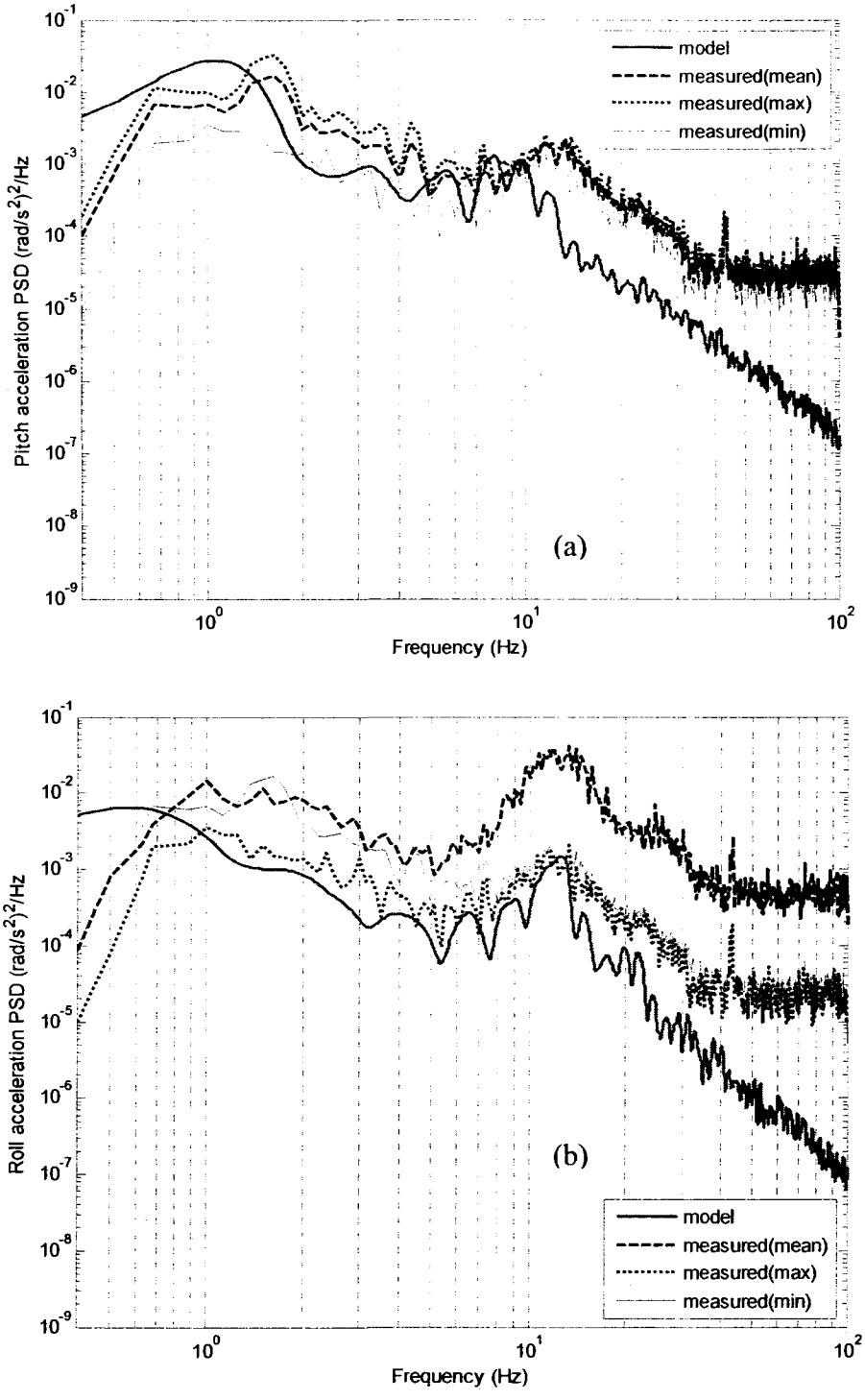

Figure 3.10: Comparison of PSD of bus body roll and pitch acceleration responses of the vehicle model with the ranges of measured data (CDN road, 50 km/h):(a) roll; and (b) pitch.

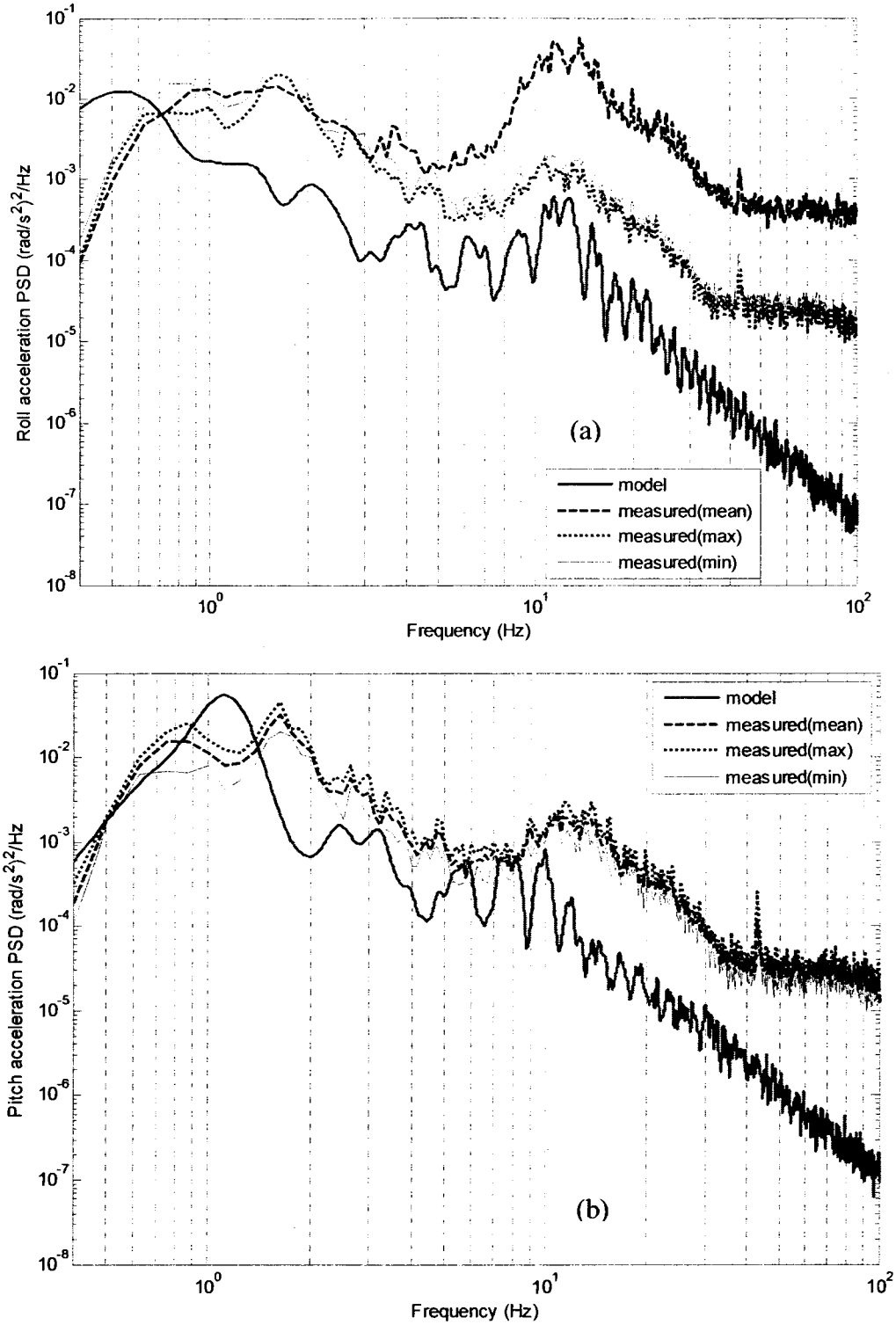

Figure 3.11: Comparison of PSD of bus body roll and pitch acceleration responses of the vehicle model with the ranges of measured data (SAP road, 50 km/h): (a) roll; and (b) pitch.

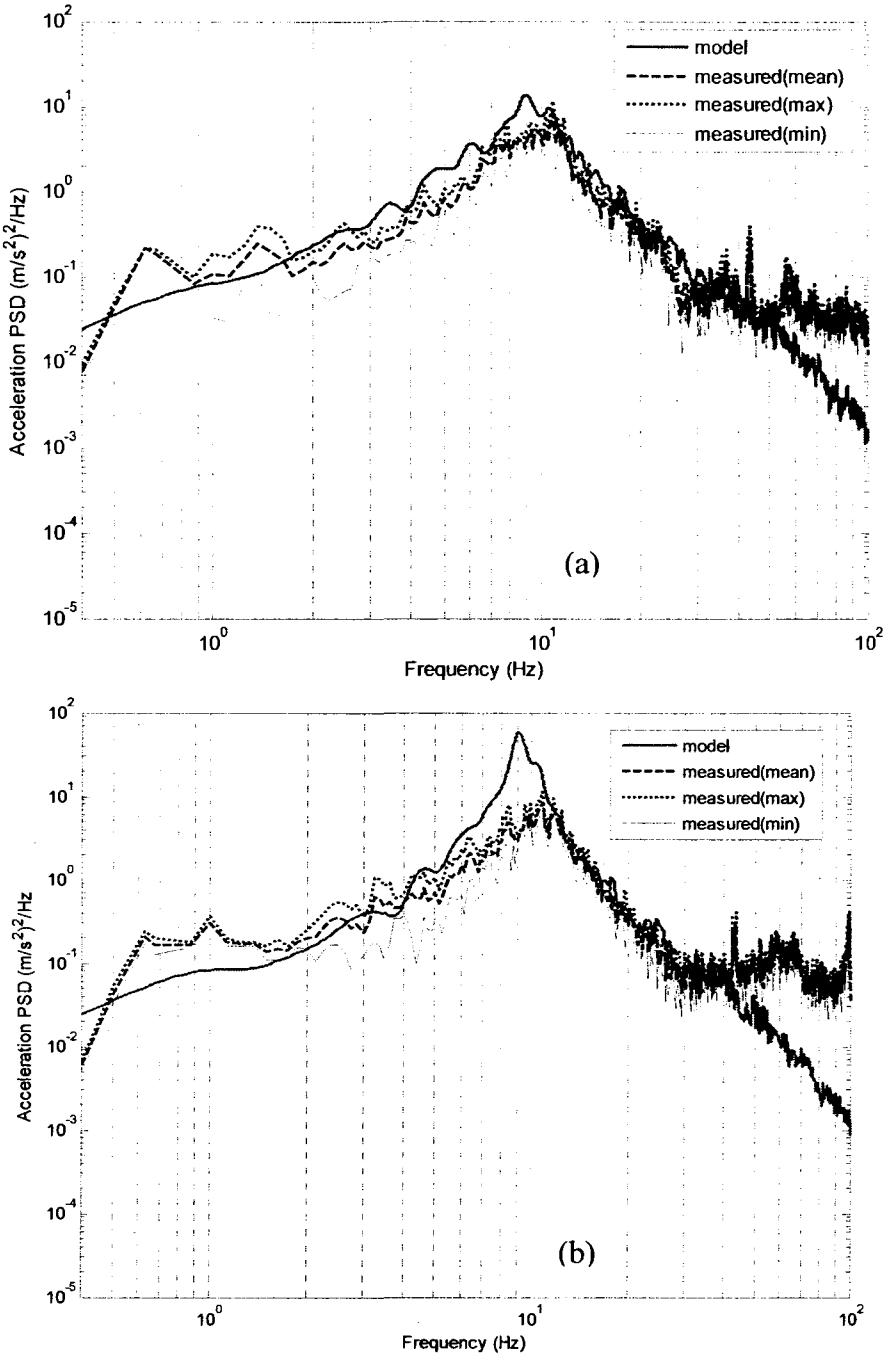

Figure 3.12: Comparison of vertical acceleration PSD responses of the unsprung masses with the range of measured data (CDN road, 50 km/h): (a) front-axle; and (b) rear-axle.

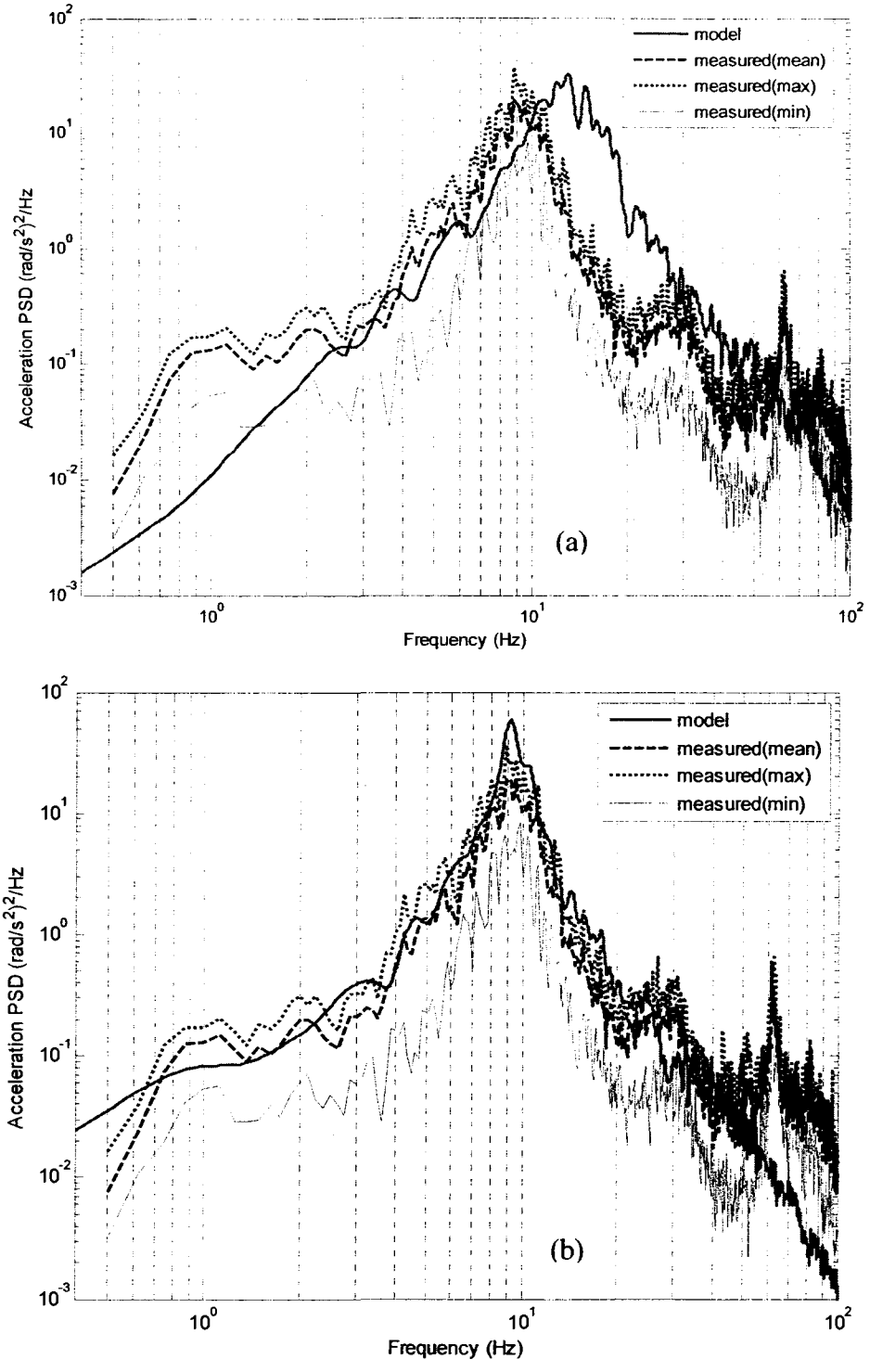

Figure 3.13: Comparison of roll acceleration PSD responses of the unsprung masses with the range of measured data (CDN road, 50 km/h): (a) front-axle; and (b) rear-axle.

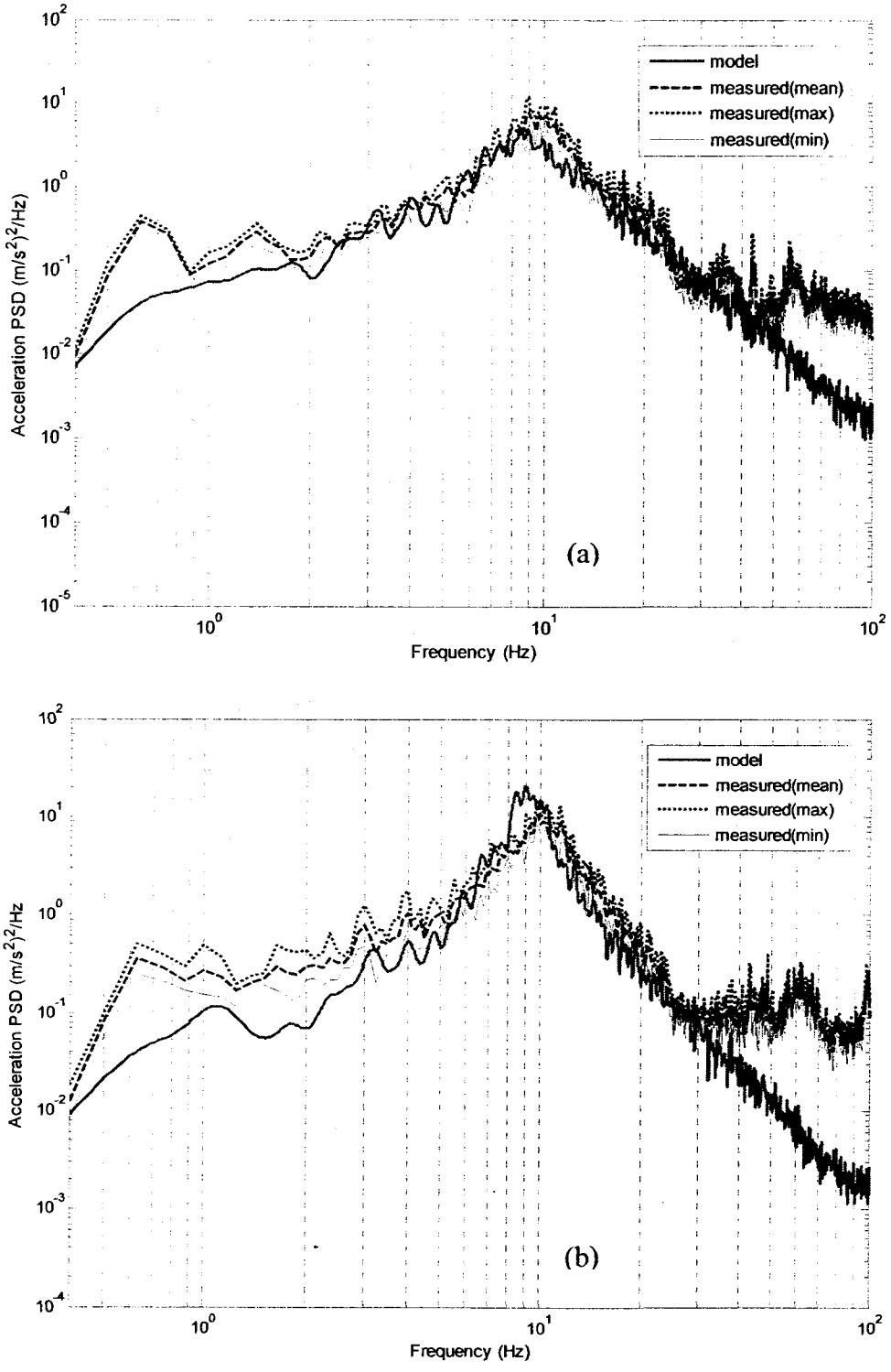

Figure 3.14: Comparison of vertical acceleration PSD responses of the unsprung masses with the range of measured data (SAP road, 50 km/h): (a) front-axle; and (b) rear-axle.

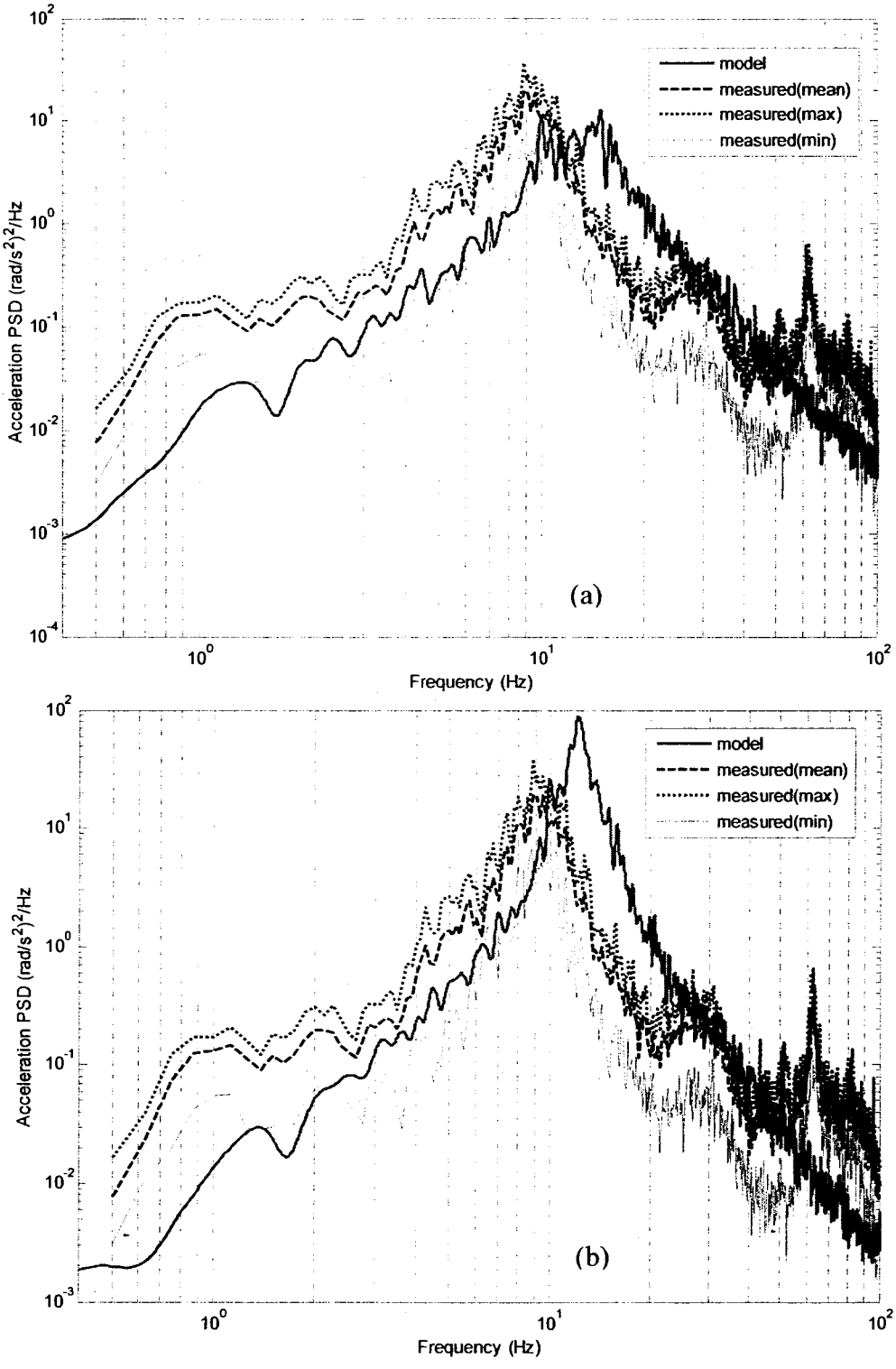

Figure 3.15: Comparison of roll acceleration PSD responses of the unsprung masses with the range of measured data (SAP road, 50 km/h): (a) front-axle; and (b) rear-axle.

CHAPTER 4

Cornering Properties and Handling Modeling

4.1 Introduction

The directional dynamic and stability limits of heavy vehicles during maneuvers are strongly related to handling characteristics and response arising from steering and/or braking inputs. Heavy vehicles experience considerable variations in operating conditions, namely load, speed and road conditions. Tire properties play a vital role in determining the vehicle handling performance since they influence the vertical and lateral forces generated at the vehicle-road interface, which control the vehicle motions during maneuvers. The implementation of a CTIS may lead to vehicle operation with tires pressure lower than the recommended pressure, particularly at light loads. The reduced pressure would affect the cornering characteristics of tires and thus the handling properties, although minimal information exists in this regard.

As mentioned earlier in section 1.2, a vast number of one-, two- and three-dimensional analytical models of road vehicles have been developed for handling and directional dynamic analyses [22-24,32,33]. The one- and two-dimensional yaw-plane models are considered adequate for analyses of lateral dynamics and handling properties of vehicles, when the contribution due to roll dynamics is considered negligible [6,31]. Three-dimensional analytical models are applied in the presence of vehicle roll motions [32,33]. Such models, however, have not been applied to study the effect of tire pressure on handling responses, although the effect of tire inflation pressure could be evaluated,

provided that the cornering properties are characterized for the chosen inflation pressure and the load. The cornering properties of different heavy vehicle tires have been measured under different loads and inflation pressures [30], which may be applied to characterize the tire cornering properties.

In this chapter, two-dimensional and three-dimensional models of the vehicle are formulated to investigate the handling properties under steering inputs. The reported tire data are used to propose a nonlinear regression model in cornering properties as a function of inflation pressure and normal load. The nonlinear vertical properties of tire and suspension components, presented in Chapter 2, are also incorporated in the three-dimensional model for transient handling analysis.

4.2 Two-Dimensional Handling Model

The handling properties of road vehicles are mostly evaluated in the yaw-plane using a two-dimensional model [40]. The two-dimensional yaw-plane model is adapted in this study, as shown in Figure 4.1. The handling model is subject to steering inputs at front-left and right wheels δ_{fi} and δ_{fo}. The governing equations are formulated by considering a body-fixed coordinate system (x,y) and an inertial coordinate system (X,Y). The contributions due to roll and pitch dynamics to the lateral motions are assumed to be small and thus neglected, while the vehicle is assumed to travel at a constant forward speed. The degrees-of-freedom in this model are limited to lateral and yaw motions in the horizontal plane, while unsprung masses are rigidly attached to the sprung mass. There are no significant tire forces present in the longitudinal direction. Furthermore, the steering system dynamics is also ignored in the model and the steering input is assumed

to be given directly to the front wheels [31,40]. The lateral load transfers attributed to lateral acceleration are computed quasi-statically.

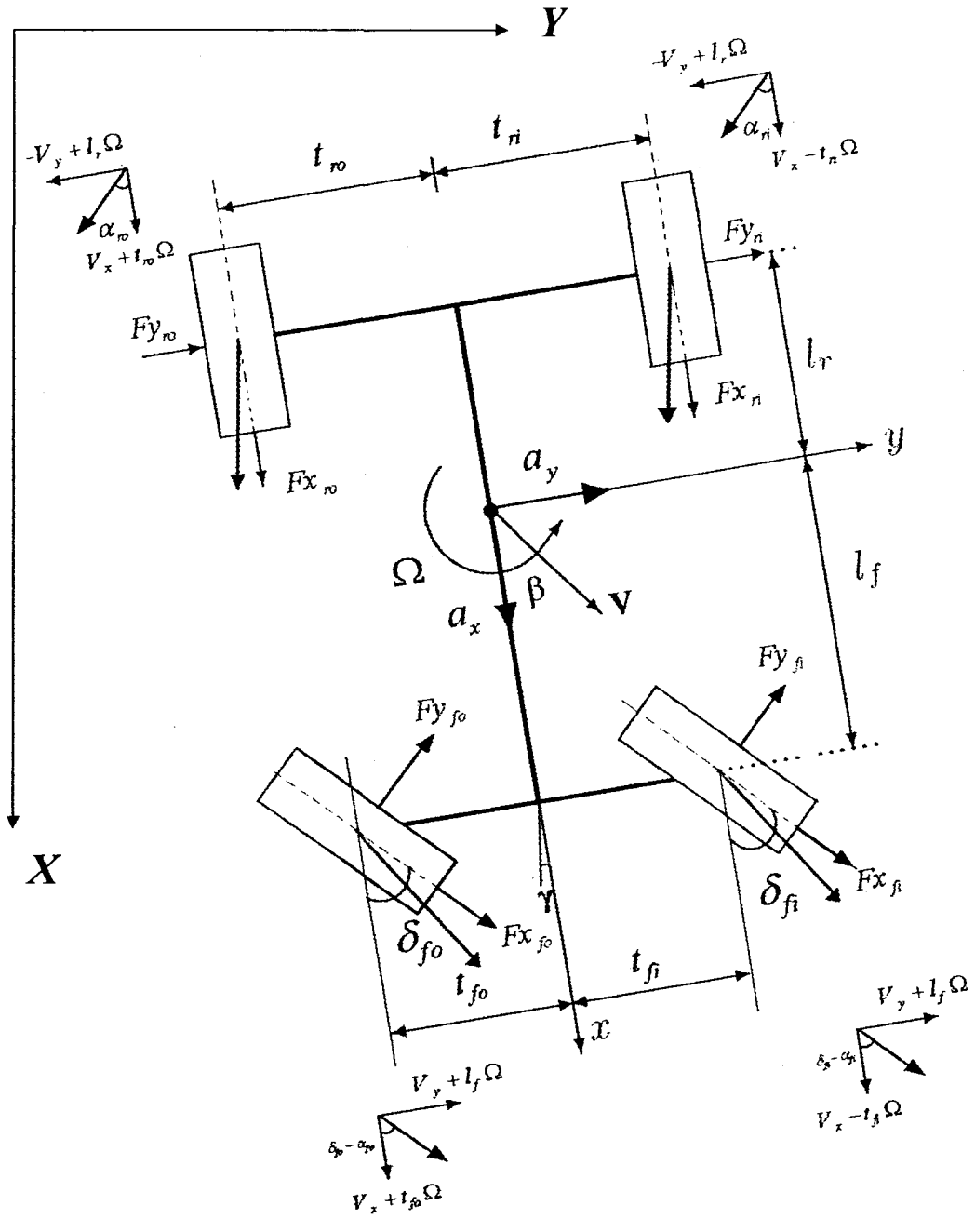

Figure 4.1: Two-dimensional yaw-plane vehicle handling model.

4.2.1 EQUATIONS OF MOTION

The equations of motions of the three-DOF yaw plane model are formulated in the inertial coordinate system and expressed below

$$ma_x = Fx_{fo}\cos(\delta_{fo}) + Fx_{fi}\cos(\delta_{fi}) + Fx_{ri} + Fx_{ro} - Fy_{fi}\sin(\delta_{fi}) - Fy_{fo}\sin(\delta_{fo}) \quad (4.1)$$

$$ma_y = Fx_{fi}\sin(\delta_{fi}) + Fx_{fo}\sin(\delta_{fo}) + Fy_{fi}\cos(\delta_{fi}) + Fy_{fo}\cos(\delta_{fo}) + Fy_{ri} + Fy_{ro} \quad (4.2)$$

$$I_z\Omega = \left[Fx_{fi}\sin(\delta_{fi}) + Fy_{fi}\cos(\delta_{fi}) + Fx_{fo}\sin(\delta_{fo}) + Fy_{fo}\cos(\delta_{fo})\right]l_f - [Fy_{ro} + Fy_{ro}]l_r + \left[Fy_{fi}\sin(\delta_{fi}) - Fx_{fi}\cos(\delta_{fi})\right]t_{fi} + \left[Fx_{fo}\cos(\delta_{fo}) - Fy_{fo}\sin(\delta_{fo})\right]t_{fo} + Fx_{ri}t_{ri} + Fx_{ro}t_{ro} \quad (4.3)$$

Where m is the vehicle mass, and F_{xfo} and F_{xfi} are longitudinal forces developed by the outside and inside tires on the front axle, respectively. F_{xri} and F_{xro} are the respective longitudinal forces due to rear axle inside and outside tires. F_{yfi} and F_{yfo} are the cornering forces developed by the inside and outside front axle tires, respectively, and F_{yri} and F_{yro} are the respective forces due to rear axle tires. I_z is yaw mass moment of inertia of the total bus mass about the z-axis and Ω is its yaw rate. l_f and l_r are the distance form bus c.g to the front and rear axles, respectively. t_{fi} and t_{fo} are the lateral distance between the front axle c.g and inner and outer front tire contact points, respectively, and t_{ri} and t_{ro} are respective lateral coordinates of the inner and outer rear tire contact points from the rear axle c.g. α_{fi}, α_{fo}, α_{ri} and α_{ro} are the inner-front, outer-front, inner- rear and outer-rear tire slip angles, respectively. The longitudinal (a_x) and lateral (a_y) accelerations are related to vehicle velocities V_x and V_y through coordinate transformation [6]:

$$a_x = \dot{V}_x - V_y\Omega$$
$$a_y = \dot{V}_y + V_x\Omega \tag{4.4}$$

Where V_x and V_y are the longitudinal and lateral vehicle velocities, respectively. Furthermore, following kinematic relations are used to compute the resultant vehicle heading and path trajectory:

$$\dot{X} = V_x \cos(\gamma) - V_y \sin(\gamma)$$
$$\dot{Y} = V_x \sin(\gamma) + V_y \cos(\gamma) \tag{4.5}$$
$$\dot{\gamma} = \Omega$$

Where γ is the yaw angle of the vehicle.

4.2.2 TIRE NORMAL LOADS

A road vehicle experiences load transfer to/from inner and the outer tires during a steady-turn, which instantaneously alter tire forces during the maneuver. The instantaneous tire forces can be derived from quasi-static equilibrium, considering the effect of lateral acceleration, as shown in the Figure 4.2 for the two axles, such that:

$$Ft_{fi} = \frac{m_f g t_{fo} - m_{sbf} a_y h_{scg} - m_{uf} a_y h_{uf}}{t_{fi} + t_{fo}}$$
$$Ft_{fo} = \frac{m_f g t_{fi} + m_{sbf} a_y h_{scg} + m_{uf} a_y h_{uf}}{t_{fi} + t_{fo}}$$
$$Ft_{ri} = \frac{m_r g t_{ro} - m_{sbr} a_y h_{scg_s} - m_{ur} a_y h_{ur}}{t_{ri} + t_{ro}} \tag{4.6}$$
$$Ft_{ro} = \frac{m_r g t_{ri} + m_{sbr} a_y h_{scg} + m_{ur} a_y h_{ur}}{t_{ri} + t_{ro}}$$

Where h_{uf} and h_{ur} are the heights of the front and rear axle roll centers, respectively, which are assumed to be fixed, h_{scg} is the sprung mass c.g height with respect to ground. m_{sbf} and m_{sbr} are the proportions of the sprung mass supported by the front and rear axles,

respectively, as described in Eq. (2.22). The above instantaneous loads are subsequently applied to determine the cornering properties of tires in section 4.3.2.

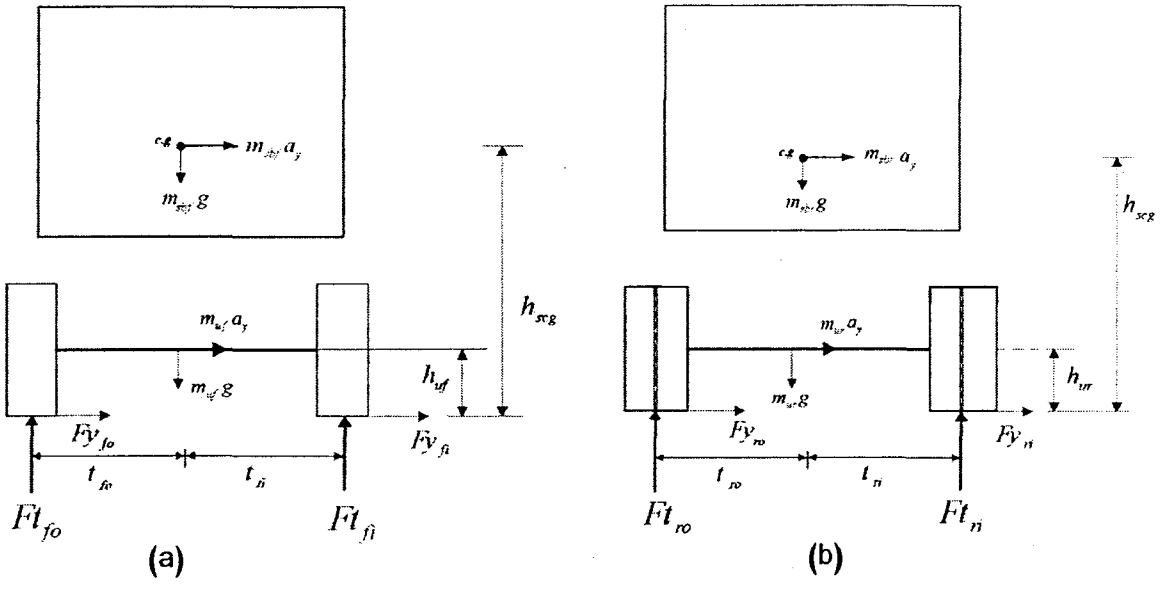

Figure 4.2: Instantaneous tire forces: (a) front-axle tires; and (b) rear-axle tires.

4.3 Three-Dimensional Handling Model

Urban buses are designed with soft air suspension to provide better attenuation of vibration cause by relatively rough urban roads. Furthermore, the steering axle is designed without an anti-roll bar due to lack of adequate space. The soft air suspension coupled together with a single roll bar at the rear axle alone, would yield relatively low roll stiffness and considerable roll motion of the sprung mass. This is also evident from the measured roll vibration reported in [1]. The two-dimensional yaw-plane model presented in the previous section may not yield adequate prediction of handling response in presence of appreciable roll motion. Consequently, a three-dimensional vehicle model

is formulated to incorporate both yaw and roll motions of the sprung mass together with nonlinear suspension and tire properties.

The model considers a total of five-DOF attributed to lateral, yaw and roll motions of the sprung mass, and roll motions of the two unsprung masses. The road surface is assumed perfectly flat. The suspension deflection is thus entirely attributed to lateral load transfer and roll deflection of the sprung and unsprung masses. A constant forward speed is assumed with negligible pitch motion, while the vertical motion arises only from the roll motion about the roll center. Furthermore, the air resistance, and tractive or braking inputs are ignored [24,32,33]. The axles are treated as beam axles, which are free to roll and bounce with respect to the sprung mass to which they are attached. A schematic of the model in the roll plane is illustrated in Figure 4.4, while the three-dimensional model is shown in Figure 4.3. The roll and yaw deflections are assumed to be small and the products of inertia are assumed to be negligible in the (x,y,z) coordinate system [24].

The roll motion of the sprung mass is assumed to takes place about the sprung mass roll center (RC), as shown in Figure 4.4. The unsprung masses (axles) roll centers are assumed to be located in their respective mass centers. The nonlinear suspension component models, described in Chapter 2, are incorporated in the model. The cornering force produced by a given tire is considered to be a nonlinear function of the slip angle, vertical load and inflation pressure. The influence of wheel camber on the lateral force generation has been neglected.

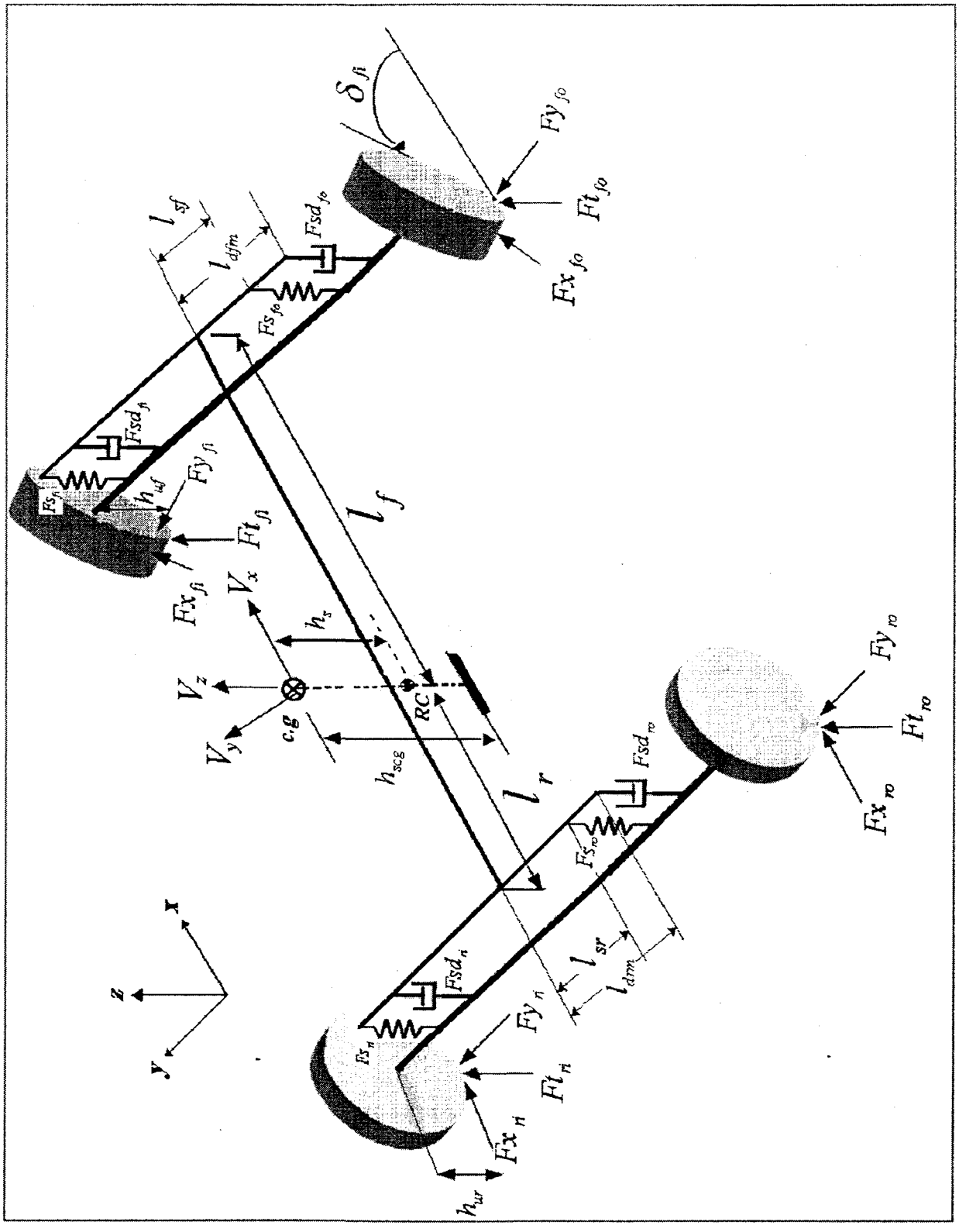

Figure 4.1: Three-dimensional yaw/roll plane model of the vehicle.

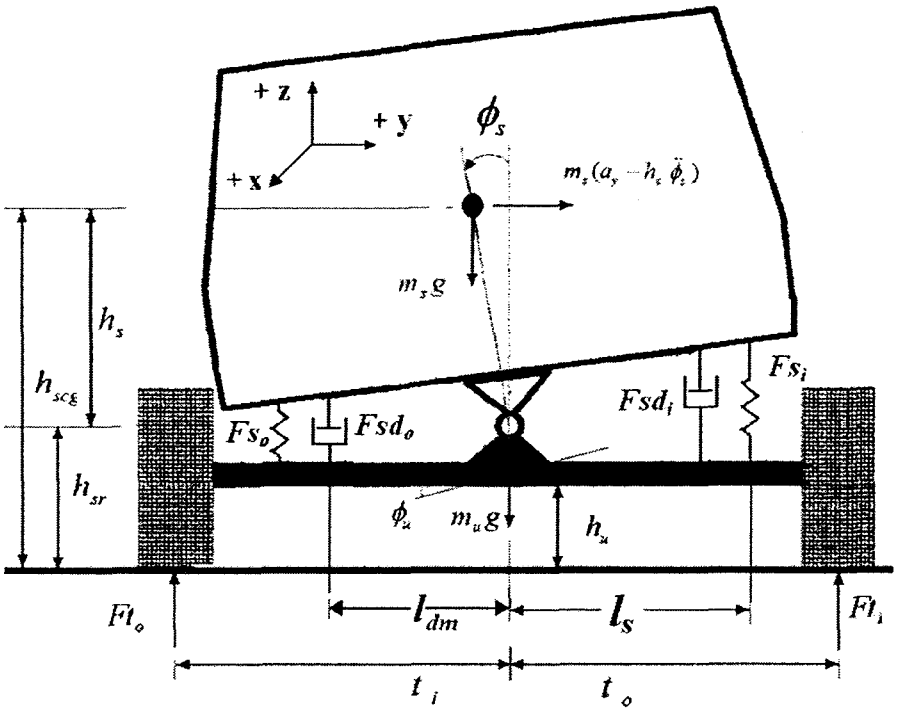

Figure 4.4: Roll plane representation of the three-dimensional yaw/roll-plane handling model.

4.3.1 EQUATIONS OF MOTION

Assuming negligible effect of bounce and pitch dynamics and the aligning moment of the vehicle tires, the three-dimensional model of the vehicle is represented by 5 DOF systems comprising lateral, roll and yaw motions due to the sprung mass, and roll motions of the unsprung masses. The equations of motion are derived upon considering the nonlinear force-deflection relationships for the air springs and force–velocity characteristics of shock absorbers, described in Chapter 2. The equations of motion governing the motions of the sprung and unsprung masses are expressed below [24,32,33]:

Lateral vehicle motion:

$$ma_y - m_s\left(h_s\ddot{\phi}_s\right) = Fx_{fi}\sin\left(\delta_{fi}\right) + Fx_{fo}\sin(\delta_{fo}) + Fy_{fi}\cos(\delta_{fi}) + Fy_{fo}\cos\left(\delta_{fo}\right) + Fy_{ri} + Fy_{ro} \tag{4.7}$$

Sprung mass roll motion:

$$I_{s\phi}\ddot{\phi}_s - m_s\left(a_y - h_s\ddot{\phi}_s\right)h_s = \left(Fsd_{fo} - Fsd_{fi}\right)l_{dfm} + \left(Fs_{fi} - Fs_{fo}\right)l_{sf} + \left(Fsd_{ro} - Fsd_{ri}\right)l_{drm} + \left(Fs_{ri} - Fs_{ro}\right)l_{sr} + m_{sb}gh_s\phi_s + K_\phi(\phi_{ur} - \phi_s) \tag{4.8}$$

Front axle roll motion:

$$I_{uf}\ddot{\phi}_{uf} = -\left(Fsd_{fo} - Fsd_{fi}\right)l_{dfm} - \left(Fs_{fi} - Fs_{fo}\right)l_{sf} + Ft_{fi}t_{fi} - Ft_{fo}t_{fo} + \left(Fy_{fi} + Fy_{fo}\right)\left(h_{scg} - h_{uf}\right) - m_{uf}a_y\left(h_{scg} - h_s - h_{uf}\right) \tag{4.9}$$

Rear axle roll motion:

$$I_{ur}\ddot{\phi}_{ur} = -\left(Fsd_{ro} - Fsd_{ri}\right)l_{drm} - \left(Fs_{ri} - Fs_{ro}\right)l_{sr} + Ft_{ri}t_{ri} - Ft_{ro}t_{ro} + \left(Fy_{ri} + Fy_{ro}\right)\left(h_{scg} - h_{ur}\right) - m_{ur}a_y\left(h_{scg} - h_s - h_{uf}\right) - K_\phi(\phi_{ur} - \phi_s) \tag{4.10}$$

Vehicle yaw motion:

$$I_z\Omega = \left(m_{ur}l_r - m_{uf}l_f\right)a_y - \left[Fy_{ro} + Fy_{ro}\right]l_r + \left[\,Fx_{fi}\sin\left(\delta_{fi}\right) + Fy_{fi}\cos\left(\delta_{fi}\right) + Fx_{fo}\sin(\delta_{fo}) + Fy_{fo}\cos\left(\delta_{fo}\right)\right]l_f + \left[Fy_{fi}\sin(\delta_{fi}) - Fx_{fi}\cos(\delta_{fi})\right]t_{fi} + \left[Fx_{fo}\cos(\delta_{fo}) - Fy_{fo}\sin(\delta_{fo})\right]t_{fo} + Fx_{ri}t_{ri} + Fx_{ro}t_{ro} \tag{4.11}$$

Where a_x and a_y are the longitudinal and lateral accelerations, respectively, of the vehicle mass obtained from Eq. (4.4). φ_s, φ_{uf} and φ_{ur} are the roll angles of bus body, and front and rear axles, respectively. $I_{sb\varphi}$ and I_z are the roll and yaw mass moments of inertia of the bus body (sprung mass), respectively about its mass center (c.g), and I_{uf} and I_{ur} are the roll mass moments of inertia of the front and rear axles assemblies, respectively, about their respective mass centers. K_φ is anti-roll bar roll stiffness, and F_s and F_{sd} represent the air spring and damper forces, respectively, while the subscripts *i*, o, *f* and *r* refer to inner side, outer side, front axle and rear axle geometrical positions of the suspension forces, and vertical and lateral tire forces, respectively. The suspension forces and tire vertical forces are derived from formulations presented in Chapter 2.

4.3.2 TIRE CORNERING PROPERTIES

The reported measured data on cornering properties of tires [30] are analyzed to derive a regression base model for characterizing tire cornering stiffness properties as a function of vertical load and inflation pressure. Although the data reported for different tires lacked definite trends with changes in inflation pressure, the data reported for heavy vehicle tires generally revealed some consistent trends. Figure 4.5 shows the variations in cornering stiffness of three different heavy vehicle tires under different inflation pressures and two different normal loads (17.79 kN and 26.69 kN) [30]. Data reveals an increase in cornering stiffness with increase in inflation pressure at the higher load. A further increase in inflation pressure causes the cornering stiffness to decrease for two of three tires considered in the reported study. The cornering stiffness, however, decreased with an increase in pressure at the lighter load. The data for 12R22.5 tire used in the bus considered in this study also exhibits low cornering stiffness at the light load, while at relatively lager load cornering stiffness increases as pressure reaches near 75-80 psi. The cornering stiffness then decreases as the pressure increases beyond 75 psi, as shown in the Figure 4.5. The cornering force developed by a tire is known to be a nonlinear function of the side-slip angle. Figure 4.6 further shows the effect of vertical load on lateral force-slip angle characteristics of 12R22.5 tire at an inflation pressure of 100 psi. It is evident that the lateral force of a tire increases with increasing normal load and is a nonlinear function of side-slip angle. The available measured data in cornering stiffness and lateral force under different normal loads and inflation pressures are utilized to formulate a relation between cornering stiffness and the tire vertical load at different

inflation pressures. A regression analysis has thus been performed to fit the available measured data using a cubic polynomial of the form:

$$C_\alpha(F_t) = p_1 F_t^3 + p_2 F_t^2 + p_3 F_t + p_4 \quad (4.12)$$

Where C_α is tire cornering stiffness (N/rad), F_t is the vertical tire load (N), and p_1 to p_4 are constants. The measured data are used to identify the regression model coefficients corresponding to five different tire pressures (50, 75, 90, 100 and 120 psi). The computed constants are summarized in Table 4.1.

Table 4.1: Coefficients of the 3rd order polynomial for the cornering stiffness.

Pressure, kPa (psi)	p_1	p_2	p_3	p_4
344.74 (50)	3.39×10^{-9}	-465.38×10^{-6}	16.87	120.22
517.11 (75)	5.36×10^{-10}	-255.42×10^{-6}	14.00	-950.65
620.53 (90)	-4.02×10^{-10}	-155.98×10^{-6}	11.85	303.29
689.48 (100)	-1.36×10^{-9}	-52.32×10^{-6}	9.52	58.44
827.37 (120)	-6.37×10^{-10}	-51.24×10^{-6}	8.40	161.81

Figure 4.7 illustrates the variations in cornering stiffness of the tire as a function of normal load function corresponding to different inflation pressures. The cornering properties derived from the regression model are compared with available measured data corresponding to two different loads at 50, 75 and 100 psi pressures. The model results at 100 psi are compared with data reported over a wider range of normal loads. The results suggest that the cornering stiffness increases with increasing normal load. The peak cornering stiffness occurs at a relatively higher normal load at higher pressure compared to that at a lower pressure.

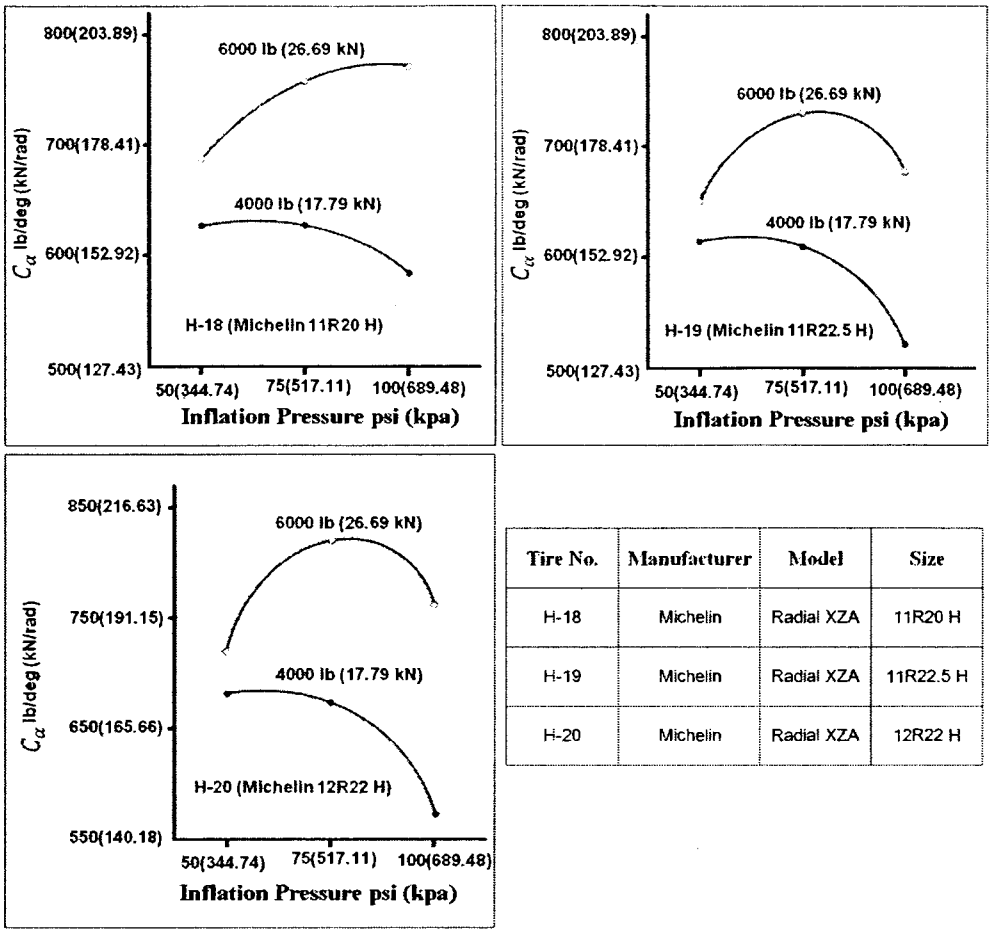

Tire No.	Manufacturer	Model	Size
H-18	Michelin	Radial XZA	11R20 H
H-19	Michelin	Radial XZA	11R22.5 H
H-20	Michelin	Radial XZA	12R22 H

Figure 4.5: Measured data displaying the effect of inflation pressure on cornering stiffness of heavy vehicle tires under two different normal loads [30].

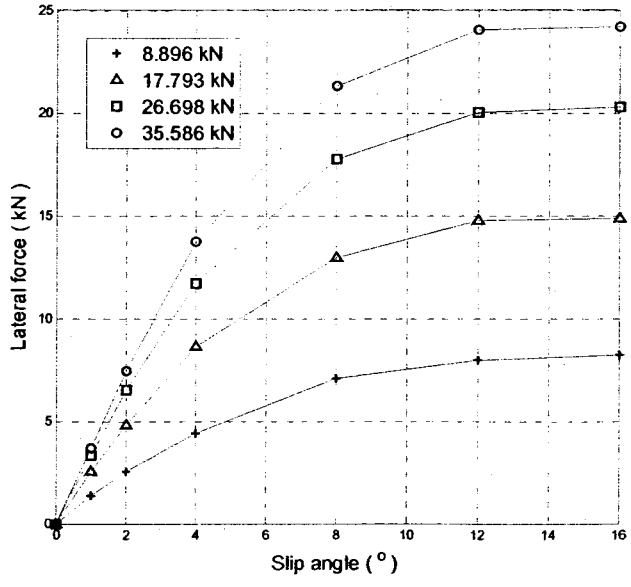

Figure 4.6: Effect of tire load on lateral force (measured data for Michelin 12 R22.5 at 689.48 kPa (100 psi) [30].

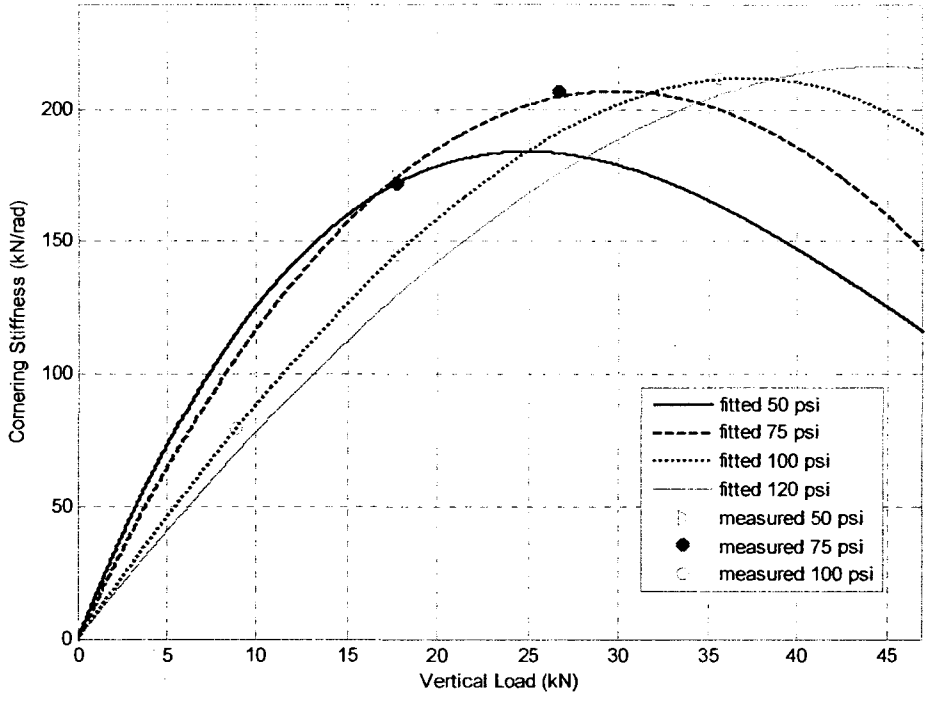

Figure 4.7: Effect of load on cornering stiffness at specific inflation pressures.

4.3.3 STEERING ANGLES

It assumed the steering input is applied directly to the front tires, while the steering angles of the inner and outer tires of the front axle are derived using the Ackerman steering geometry, such that [10]:

$$\delta_{fi} = \frac{L}{R - \frac{t_f}{2}}; \text{ and } \delta_{fo} = \frac{L}{R + \frac{t_f}{2}} \tag{4.13}$$

Where δ_{fi} and δ_{fo} are the inner and outer wheel steer angles, respectively. $t_f = t_{fi} + t_{fo}$ is the front-axle track width, and R is turn radius. Assuming $R \gg t_f/2$, average steer angle can be approximated as L/R. The inside and outside wheels angles are then related to average steer angles δ_f, as:

$$\delta_{fi} = \frac{2L\delta_f}{2L - t_f\,\delta_f}; \text{and } \delta_{fo} = \frac{2L\delta_f}{2L + t_f\,\delta_f} \tag{4.14}$$

4.3.4 SLIP ANGLES AND TIRE LATERAL FORCES

Referring to the Figure 4.1, the slip angles of the vehicle tires can be derived using the kinematic relations. Assuming small steering and slip angles, the slip angles are derived from:

$$\begin{aligned}
\delta_{fi} - \alpha_{fi} &= \frac{V_{y+} l_f \Omega}{V_x - t_{fi}\,\Omega} \\
\delta_{fo} - \alpha_{fo} &= \frac{V_{y+} l_f \Omega}{V_x + t_{fo}\,\Omega} \\
\alpha_{ri} &= \frac{-V_{y+} l_r \Omega}{V_x - t_{ri}\,\Omega} \\
\alpha_{ro} &= \frac{-V_{y+} l_r \Omega}{V_x - t_{ro}\,\Omega}
\end{aligned} \tag{4.15}$$

For pure cornering analysis the lateral force F_y could be computed using the *Magic Tire Formula* [21] as a function of slip angle α and instant vertical load. The estimated cornering force may be considered valid for a specific inflation pressure. The application of regression model, defined in Eq. (4.12), could yield the related force at different inflation pressures. The general form of the magic tire formula used in the model is given by [21]:

$$F_y = D \sin[C \tan^{-1}\{B\alpha - E(B\alpha - \tan^{-1}(B\alpha))\}] \tag{4.16}$$

Where C is the shape factor, D is peak value of the lateral force, B is stiffness factor, and E is the curvature factor. This empirical formula is capable of producing characteristics that closely match measured lateral force data as a function of the side-slip angle α [10]. For small slip angles, the lateral tire force relation between F_y and α can be approximated

by the linear relation, as stated earlier in Eq. (1.2). The quantity *BCD* represents the cornering stiffness C_α which can be determined from Eq. (4.12) corresponding to a specific slip angle and normal load defined for a given inflation pressure. The constants *B*, *C*, *D* and *E* in the magic formula are obtained using the measured data, which were identified as:

$$\begin{aligned} C &= 1.3 \\ D &= \mu_y F_t \\ B &= \frac{BCD}{CD} \\ E &= f(P, F_t) \\ \mu_y &= f(F_t) \end{aligned} \tag{4.17}$$

Where μ_y is the lateral tire-road adhesion coefficient, the value of μ_y depends on the road surface and is found to be inversely proportional to the tire vertical load, as shown in Figure 4.8 for the dry asphalt road surface. The curvature factor *E* is a function of inflation pressure and the vertical load. The results of the regression analysis performed revealed that this factor can be approximated by a linear relationship in vertical load at specified inflation pressures, such that:

$$E = a_1 F_t + a_2 \tag{4.18}$$

Where the values of constants a_1 and a_2 are listed in the Table 4.2,as a function of the inflation pressure. The variations in the curvature factor *E* are evaluated as a function of normal load and selected inflation pressures, as shown in Figure 4.9. The proposed model suggests that the magnitude of *E* decreases as the load increases for a given inflation pressure, while it tends to be higher at lower inflation pressure at a constant load.

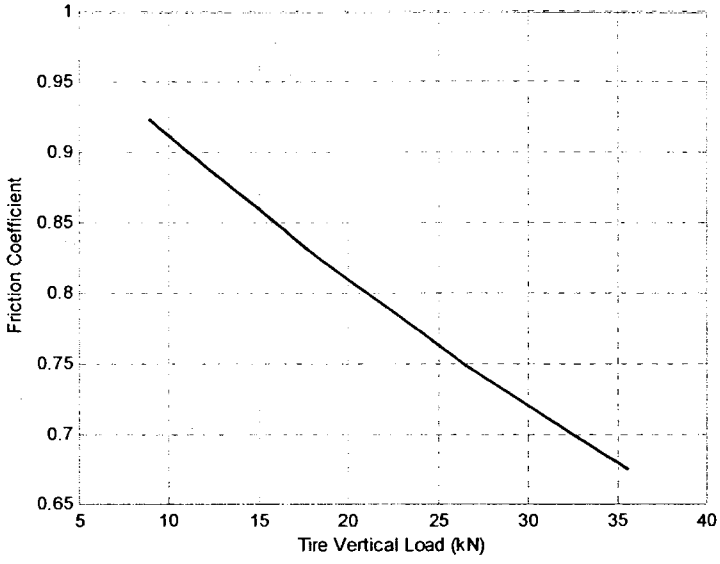

Figure 4.8: Variation in tire-road adhesion coefficient of a dry asphalt road with vertical load, calculated based on the measured data [30].

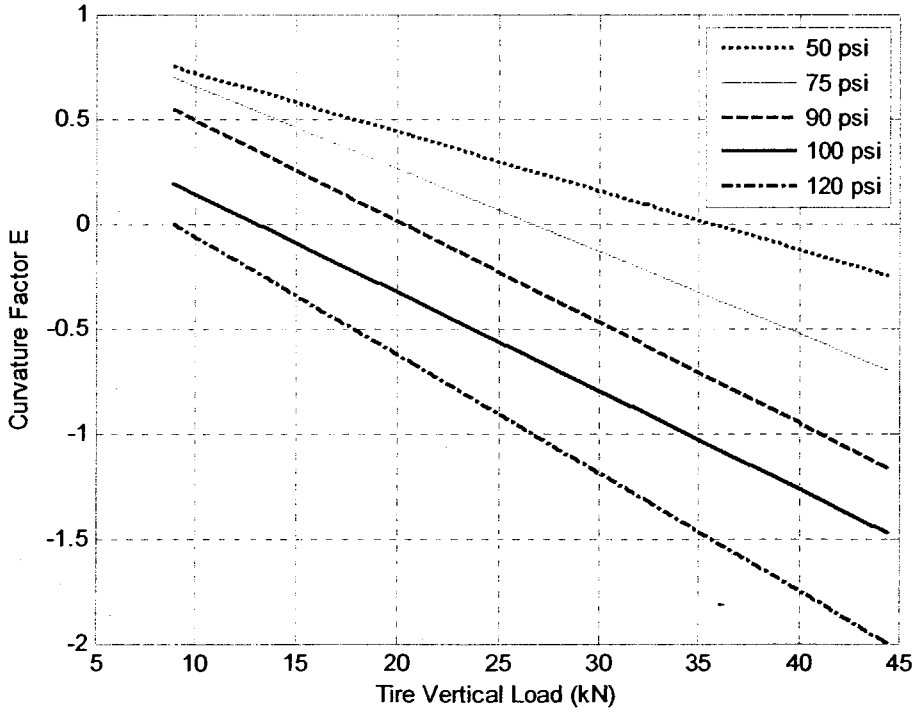

Figure 4.9: Relationship between the curvature factor E and tire vertical load at selected inflation pressures.

The Evaluation of friction coefficient $\mu_y(F_z)$ which is a function of vertical load, the curvature factor $E(P,F_z)$ and the cornering stiffness $C_\alpha(P,F_z)$ could yield estimation of tire lateral force characteristics as a function of normal load and inflation pressure.

The magic tire formula together with the curvature factor model is solved for two different loads (17.8 kN and 26.7 kN), where the measured data could be available. The computed lateral force-side slip relations for three different inflation pressures (50, 75 and 100 psi) are compared with the reported data in Figures 4.10 to 4.12, respectively.

The results show reasonably good agreements between the computed results and measured data for normal load and pressure conditions considered.

Table 4.2: Constant coefficients for estimating the curvature factor E in the tire magic formula.

Inflation Pressures (psi)	a_1	a_2
50	-2.81×10^{-5}	1
75	-3.93×10^{-5}	1.05
90	-4.82×10^{-5}	0.9286
100	-4.69×10^{-5}	0.61
120	-5.629×10^{-5}	0.5

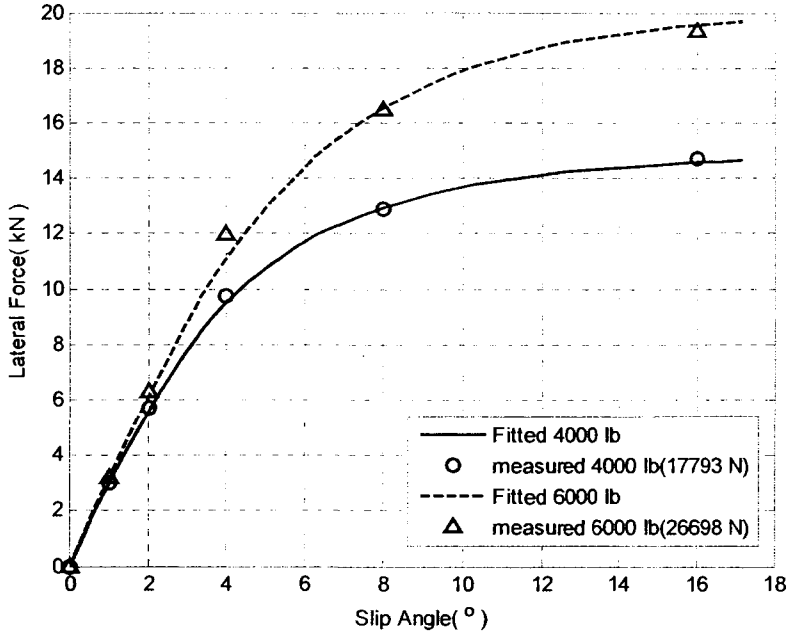

Figure 4.10: Comparison of lateral force-slip angle characteristics of tire computed from modified magic formula with measured data at an inflation pressure of 50 psi.

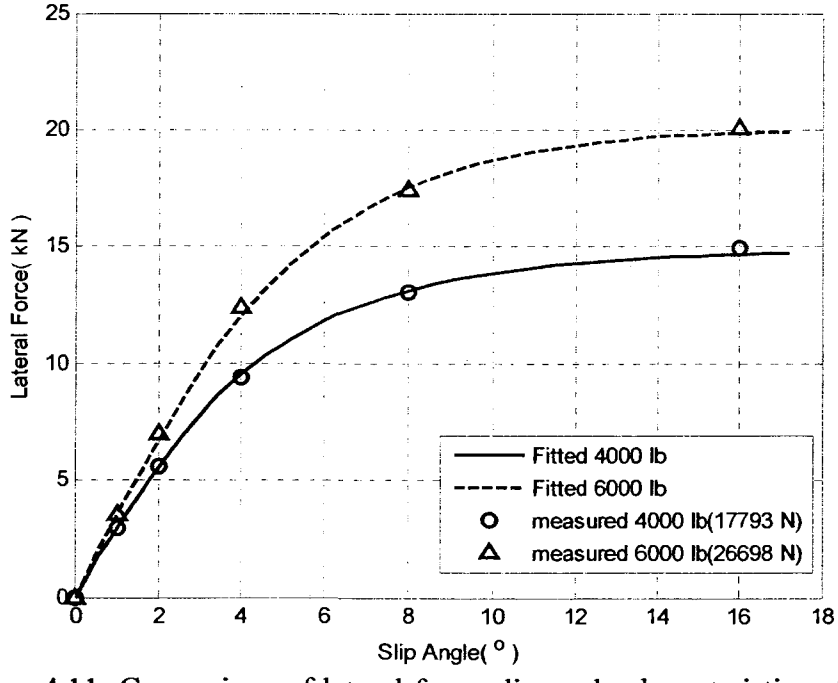

Figure 4.11: Comparison of lateral force-slip angle characteristics of tire computed from modified magic formula with measured data at an inflation pressure of 75 psi.

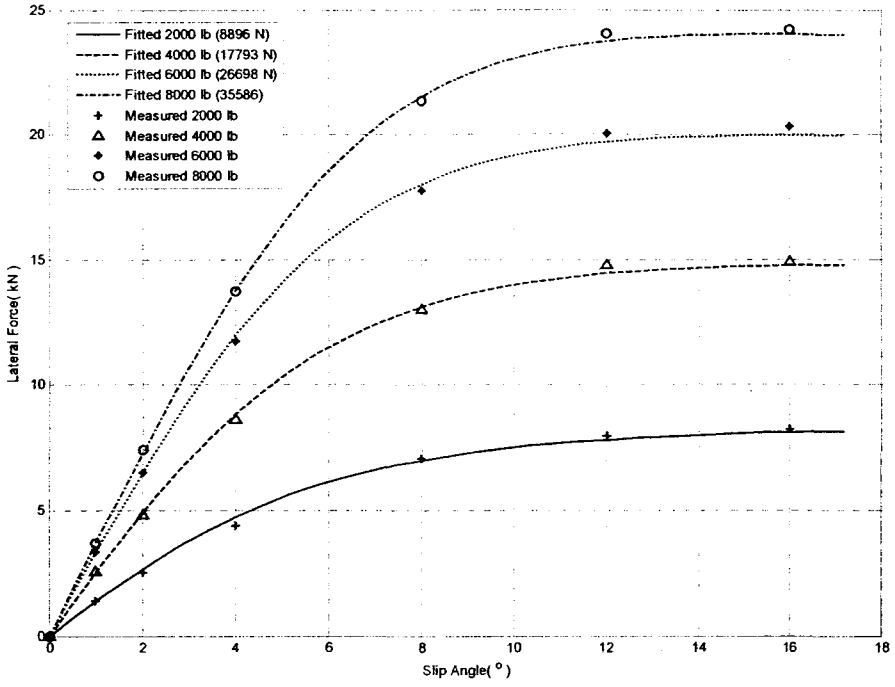

Figure 4.12: Comparison of lateral force-slip angle characteristics of tire computed from modified magic formula with measured data at an inflation pressure of 100 psi.

4.4 Summary

The two- and three-dimensional handling models of the urban bus are developed in this chapter to investigate to the effect of inflation pressure on the direction dynamics of the vehicle thereafter. The cornering properties of vehicle tire are characterized through formulation of modified magic tire formula using the available measured data. The regression models are proposed to characterize the cornering force as a function of normal load, slip angle and inflation pressure. The resulting model is applied to determine the handling properties of the vehicle under different loads and inflation pressures.

4.5 Simulation Parameters

The mass and inertial parameters required to analyze the two- and three-dimensional handling models of the *Low Floor bus*, developed in this chapter are summarized in Table 4.3. The geometrical parameters for the two-dimensional and the three-dimensional handling models are listed in the Tables 4.4 and 4.5, respectively.

Table 4.3: Urban bus mass and inertial parameters according to empty, half and full loading conditions.

Parameter	Empty	Half	Full
m_{sb} (kg)	10575	13403	16231
I_z ($kg.m^2$)	140120	165950	190960
$I_{s\varphi}$ ($kg.m^2$)	41370	42820	44163
m_{uf} (kg)	575		
m_{ur} (kg)	1200		
I_{uf} ($kg.m^2$)	315		
I_{ur} ($kg.m^2$)	657		

Table 4.4: Two-dimensional model geometrical parameters.

Parameter	Description	Value
t_{fi}, t_{fo}	Half front track width (m)	1.0933
t_{ri}, t_{ro}	Half rear track width (m)	0.9710
l_f	Longitudinal distance from body c.g to the front axle	4.105
l_r	Longitudinal distance from body c.g to the rear axle	2.095
h_s	Vertical distance from body c.g to body roll center (m)	0.6645
h_{scg}	Vertical distance from body c.g to the ground (m)	1.1725
h_{uf}	Vertical distance front axle c.g to the ground (m)	0.502
h_{ur}	Vertical distance from rear axle c.g to the ground (m)	0.502

Table 4.5: Three-dimensional model geometrical parameters.

Parameter	Description	Value
t_{fi}, t_{fo}	Half front track width (m)	1.0933
t_{ri}, t_{ro}	Half rear track width (m)	0.9710
l_f	Longitudinal distance from body c.g to the front axle (m)	4.105
l_r	Longitudinal distance from body c.g to the rear axle (m)	2.095
l_{dfm}	Lateral distance from front axle c.g to its damper mount (m)	0.7930
l_{drm}	Lateral distance from rear axle c.g to its damper mount (m)	0.6425
l_{sf}	Lateral distance from front axle c.g to its air spring mount (m)	0.6630
l_{sr}	Lateral distance rear axle body c.g to its air spring mount (m)	0.8600
h_s	Vertical distance from body c.g to body roll center (m)	0.6645
h_{uf}	Vertical distance front axle c.g to the ground (m)	0.508
h_{ur}	Vertical distance from rear axle c.g to the ground (m)	0.508

CHAPTER 5

Effect of Tire Inflation Pressure on Handling Performance

5.1 Introduction

A number of studies have experimentally investigated influences of tire pressure on the ride and pavement loading performances of heavy road and off-road vehicles [11,41]. reduced tire pressure could affect the roll and lateral dynamic performance of the vehicle in a adverse manner, which has not been addressed thus far. The handling dynamics model of the bus together with the cornering force model for the tires, developed in previous chapter are applied to determine the influences of tire pressure on selected handling properties of the vehicle. The handling dynamic responses are obtained under two types of steering inputs, step and sinusoidal, representing steady turning and path change type of maneuvers, respectively. The responses are evaluated under different tire pressures and discussed to highlight the effects of inflation pressures on various directional response measures such as yaw and roll rates, lateral acceleration, load transfer, lateral forces, slip angles, cornering stiffness, and sprung and unsprung masses roll angles. The influence of inflation pressure and loading conditions on the understeer coefficient, which represents an important measure for steady state handling characteristics, is also discussed.

5.2 Comparison of Two- and Three-Dimensional Handling Models

The steering response characteristics of the two- and three-dimensional models, presented in Chapter 4 are obtained under selected steering inputs and the results are compared for the two models. The comparisons are discussed to highlight relative merits of the models for their application in the handling analysis for different tire pressures.

5.2.1 RESPONSES TO A STEP STEER INPUT

The response characteristics of the handling models are evaluated under 2^{o} ramp-step steer input, as shown in Figure 5.1, while the forward speed is kept constant at 15 m/s. Figures 5.2 and 5.3 illustrate variations in the yaw rate, lateral acceleration, front and rear-axle load transfers, and slip angles, lateral force and cornering stiffness. The figures compare the responses of the two-dimensional (2D) and three-dimensional (yaw/roll) models. The simulation results were obtained using nominal tire pressure (100 psi). Figure 5.2 compares the yaw rate, lateral acceleration, and variations in normal loads and side slip angles of the front and rear axle tires responses of the two models. The responses in terms of lateral forces and cornering stiffness are presented in Figure 5.3, while Figure 5.2 compares the side slip angles responses.

The results show similar steady state values of the yaw rate and lateral acceleration responses of the two models, while the 2D model tends to suppress oscillations in the lateral acceleration response, as shown in Figure 5.2 (b). This is attributed to roll motion of the bus body, which is not considered in the 2D model. The two-dimensional model also yields considerably higher load transfer at the front wheels but lower for the rear wheels compared with the three-dimensional model responses, as

seen in Figures 5.2 (c) and 5.2 (d). This is attributed to lack of consideration of the unsprung mass roll and the suspension roll stiffness in the two-dimensional model. This is also evident from the load transfer relationships derived in the previous chapter. Referring to the Eq. (4.6), the load transfer of the front and rear axles tires, denoted by LTR_f and LTR_r, are expressed as:

$$LTR_f = \frac{m_{sbf} a_y h_{scg} + m_{uf} a_y h_{uf}}{t_{fi} + t_{fo}}$$
$$LTR_r = \frac{m_{sbr} a_y h_{scg_s} + m_{ur} a_y h_{ur}}{t_{ri} + t_{ro}} \quad (5.1)$$

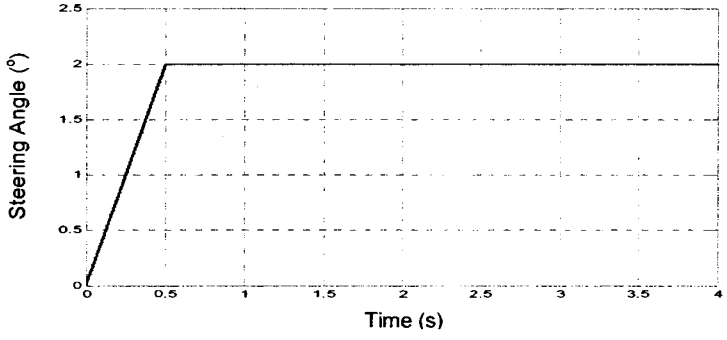

Figure 5.1: Step steer input

The load transfer of the front and rear axle wheels, derived for the three-dimensional are expressed as [34]:

$$LTR_f = \frac{m_{sbf} a_y h_{sg} + m_{uf} a_y h_{uf} + K_f \phi_s}{t_{fi} + t_{fo}}$$
$$LTR_r = \frac{m_{sbr} a_y h_{sg} + m_{ur} a_y h_{ur} + K_r \phi_s}{t_{ri} + t_{ro}} \quad (5.2)$$

Where K_f and K_r are the roll stiffness coefficients of the front- and rear-axle suspension, respectively, and h_{sg} is the roll center height with respect to ground. Referring to the Eq. (5.2), the load transfer distribution due to the three-dimensional model is strongly dependent on the roll stiffness of the axles, while that of two-dimensional model is

distributed in accordance with the static axle loads. Furthermore, the roll stiffness of the rear axle is significantly larger than that of the front axle due to additional anti-roll bar employed in the rear axle suspension. The greater load on the rear axle, however, causes considerably larger load transfer of the rear axle. The results also show oscillations in the normal load responses of the yaw/roll model, as observed in the lateral acceleration response, which is attributed to the roll-DOF of the sprung mass. Furthermore, the load transfer of the inner and outer tires of the same axle are nearly identical for the 2-D model, while slightly differences could be observed in case of the three-dimensional model, as shown in Figures 5.2 (c) and (d). This slight difference can be attributed to nonlinear vertical force-deflection characteristics of the tires.

The results further show good agreement between the 2D and three-dimensional models in terms of the slip angle and lateral tire force response, as seen in Figures 5.2 and 5.3. The yaw-roll model responses, however, exhibit oscillations attributed to sprung mass roll motion. The cornering stiffness responses (Figure 5.3) of the three-dimensional model tend to be lower for the front wheels but higher for the rear wheels, when compared to those of the 2-D model. This behavior is identical to that observed in the normal tire loads in Figure 5.2. Considering that a tire cornering force is directly related to its normal load, the observed differences can be attributed to the differences in normal load responses of the two models. It should be noticed that all the responses of the three-dimensional model oscillate at a frequency close to 0.5 Hz prior to approaching their steady state values. This frequency corresponds to the sprung mass roll mode natural frequency.

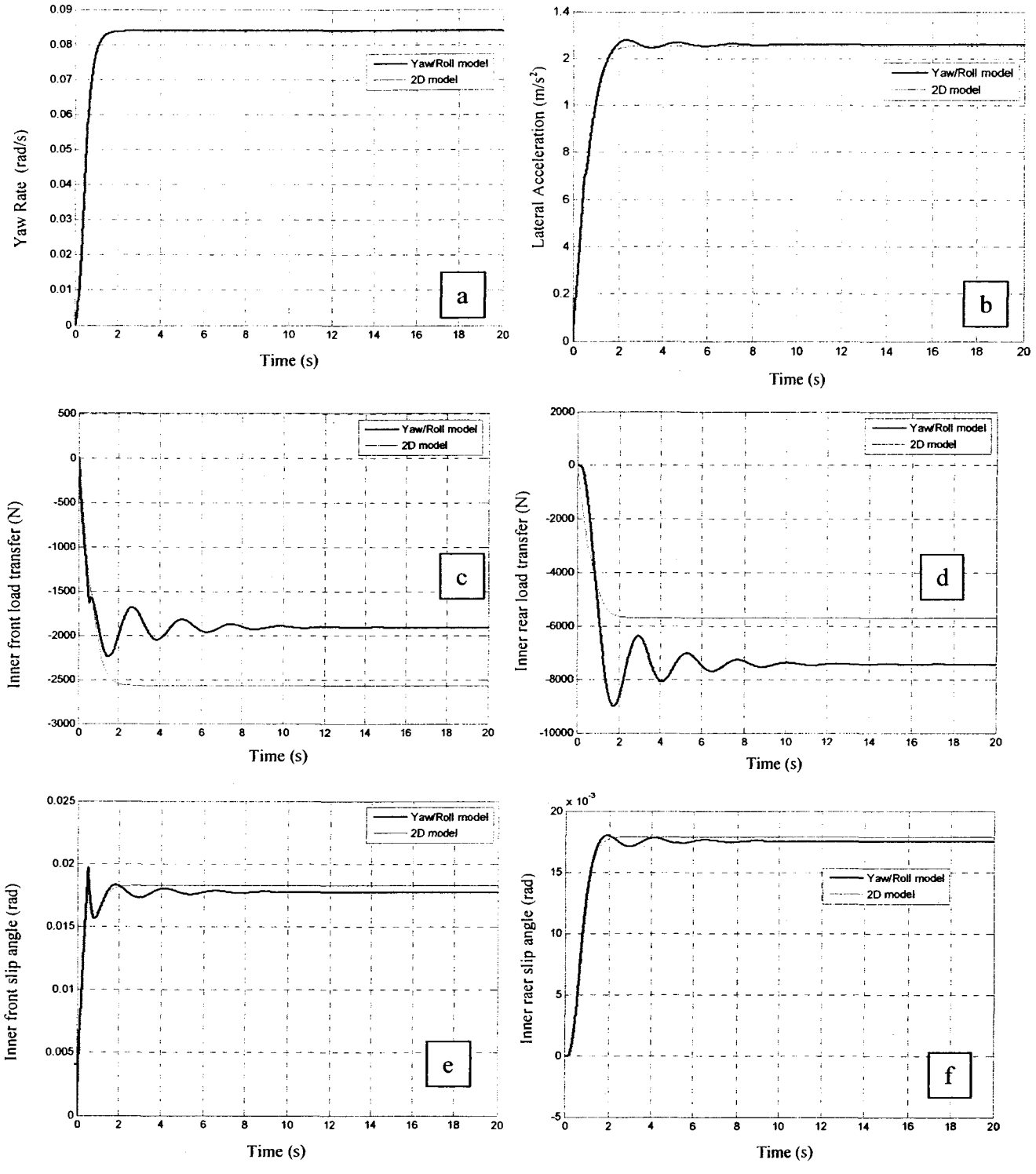

Figure 5.2: Comparisons of steering response characteristics of two- (2D) and three-(yaw/roll) dimensional handling dynamic models: (a) yaw rate; (b) lateral acceleration; (c) inner front wheel load transfer; (d) inner rear wheel load transfer; (e) inner front wheel slip angle and (f)) inner rear wheel slip angle

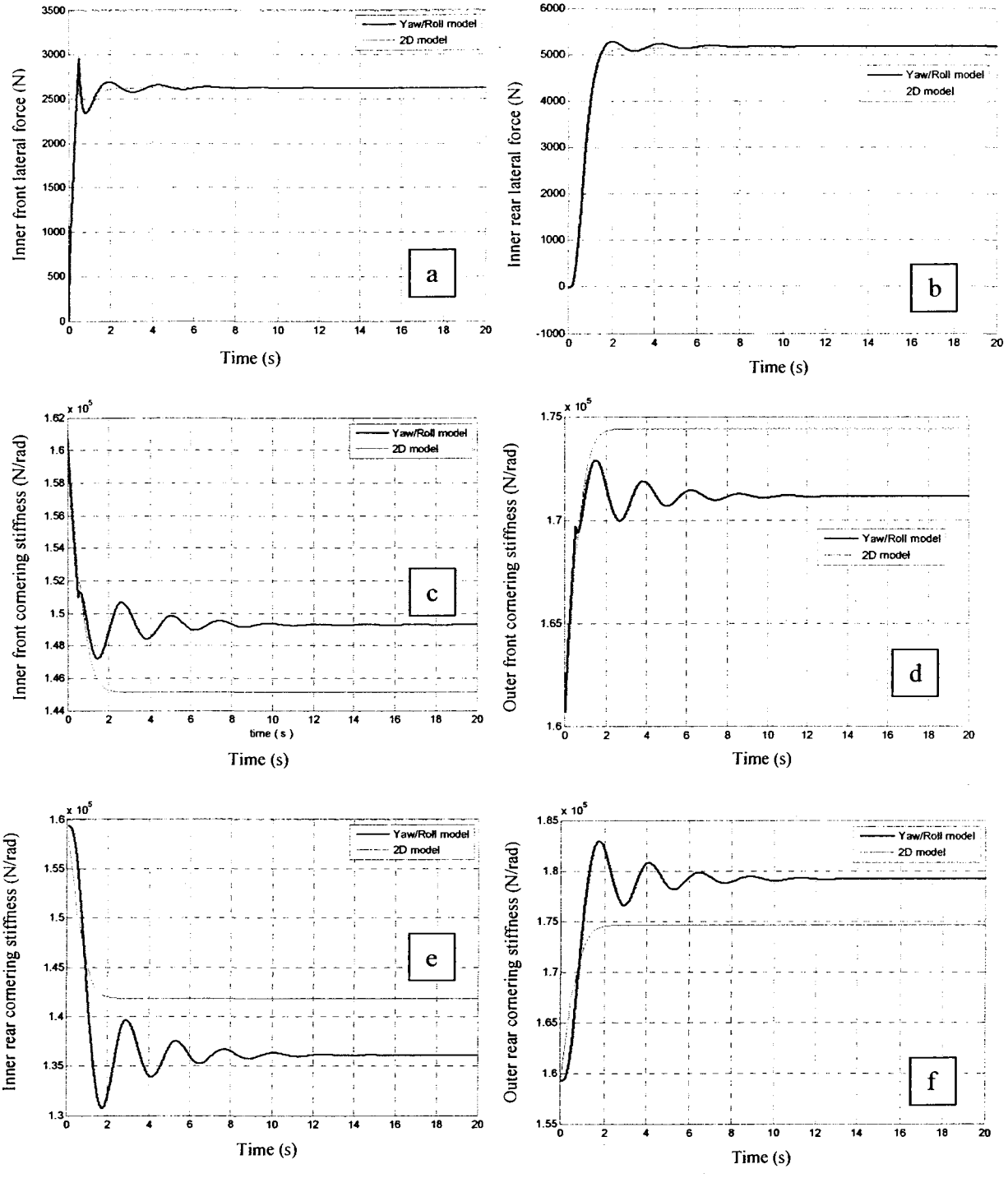

Figure 5.3: Comparisons of steering response characteristics of two- (2D) and three-(yaw/roll) dimensional handling dynamic models: (a) inner front wheel lateral force; (b) inner rear wheel lateral force; (c) inner front wheel cornering stiffness; (d) outer front cornering stiffness; (e) inner rear wheel cornering stiffness and (f) outer rear wheel cornering stiffness

Figure 5.4 compares the path trajectory responses of the two models under the selected ramp-step steer input. The results suggest that the 2-D model yields a slightly larger turn radius compared to the three-dimensional model. This difference is attributed to slightly lower value of the yaw rate response of the 2-D model, and coupling between the yaw and roll responses of the three-dimensional model.

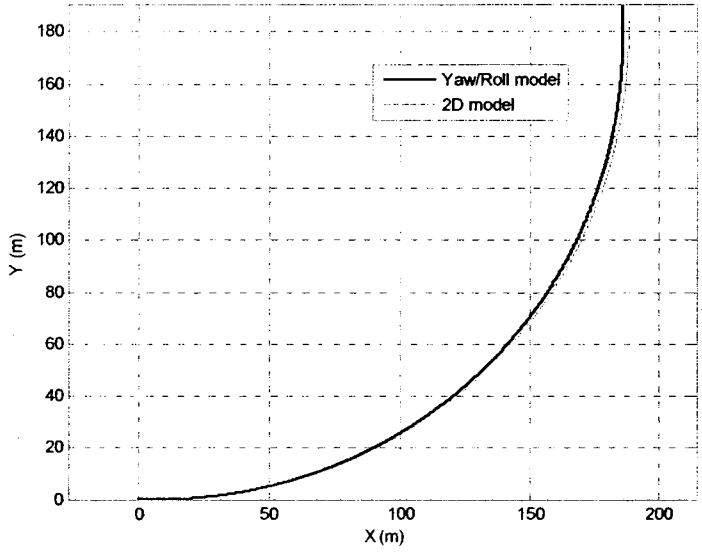

Figure 5.4: Path trajectory responses of two- and three-dimensional models under a ramp-step steer input.

5.2.2 RESPONSES TO A SINE STEER INPUT

The transient responses of the handling models are evaluated under a lane-change type of steering maneuver, which can be idealized by a 0.4 Hz single cycle sinusoidal steer input [31]. Figure 5.5 illustrates variations in the steering angle considering 2^{o} amplitude. Figures 5.6 and 5.7 compare the responses of the two- and three-dimensional models under sinusoidal steer input at a forward speed of 20 m/s, while the tire pressure is considered as 100 psi. The results, in-general, show good agreements in lateral acceleration and yaw rate responses of the two models, while the load transfer and tire

lateral responses differ considerably. Responses of the three dimensional model, in-general, exhibit oscillations, which are absent in the 2-D model responses. The oscillations are attributed to contributions due to roll motions of the sprung and unsprung masses in the 3-D model. Such oscillations also cause greater load transfer from the inner tires to the outer tires compared to those observed in the 2-D model responses, as seen in Figure 5.6. It should be noticed that normal loads on the outside tires increase, while the magnitude of the change is nearly identical to those of the inside tires. The rear-axle normal load transfer is considerably larger compared to the front axle tires, which is attributable to greater rear axle load. The side-slip angles and lateral force responses of the inside tires for the two models are somewhat comparable, as shown in the Figures 5.6 and 5.7. The responses of the 2-D model, however, exhibit rapid decay in the response oscillations, which is attributable to lack of consideration of the roll motion of the sprung and unsprung masses.

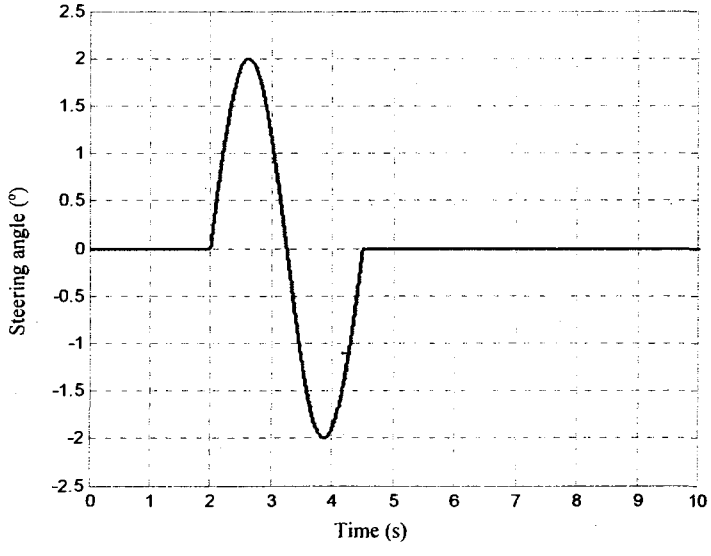

Figure 5.5: Sinusoidal steer input due to lane change maneuver.

The path change trajectory responses of the two modes are further compared in Figure 5.8. The results show that the two-dimensional model yields relatively greater steady-state lateral deviation compared with that of the three-dimensional model. This can be directly related slightly lower magnitude of yaw rate response of the 2-D model.

The results presented in Figures 5.2 to 5.8 suggest that the three-dimensional model is more reliable for predicting the handling performance of the heavy vehicle specially the transient handling properties, since the vehicle sprung and unsprung masses exhibit considerably roll motions. On the other hand, the two-dimensional model yields comparable steady-state handling responses under both steering input.

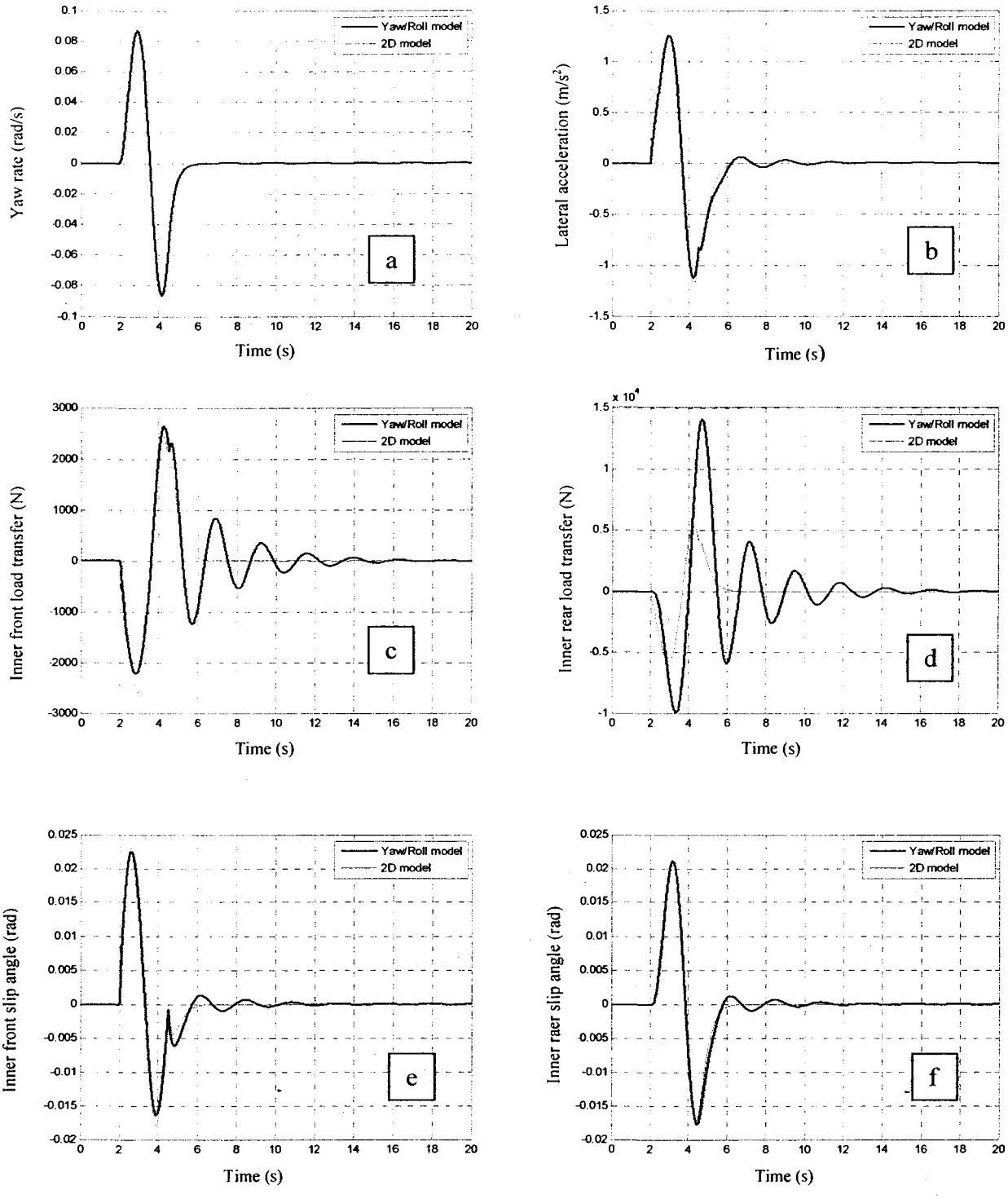

Figure 5.6 Comparisons of steering response characteristics of two- (2D) and three-(yaw/roll) dimensional handling dynamic models: (a) yaw rate; (b) lateral acceleration; (c) inner front wheel load transfer; (d) inner rear wheel load transfer; (e) inner front wheel slip angle and (f)) inner rear wheel slip angle

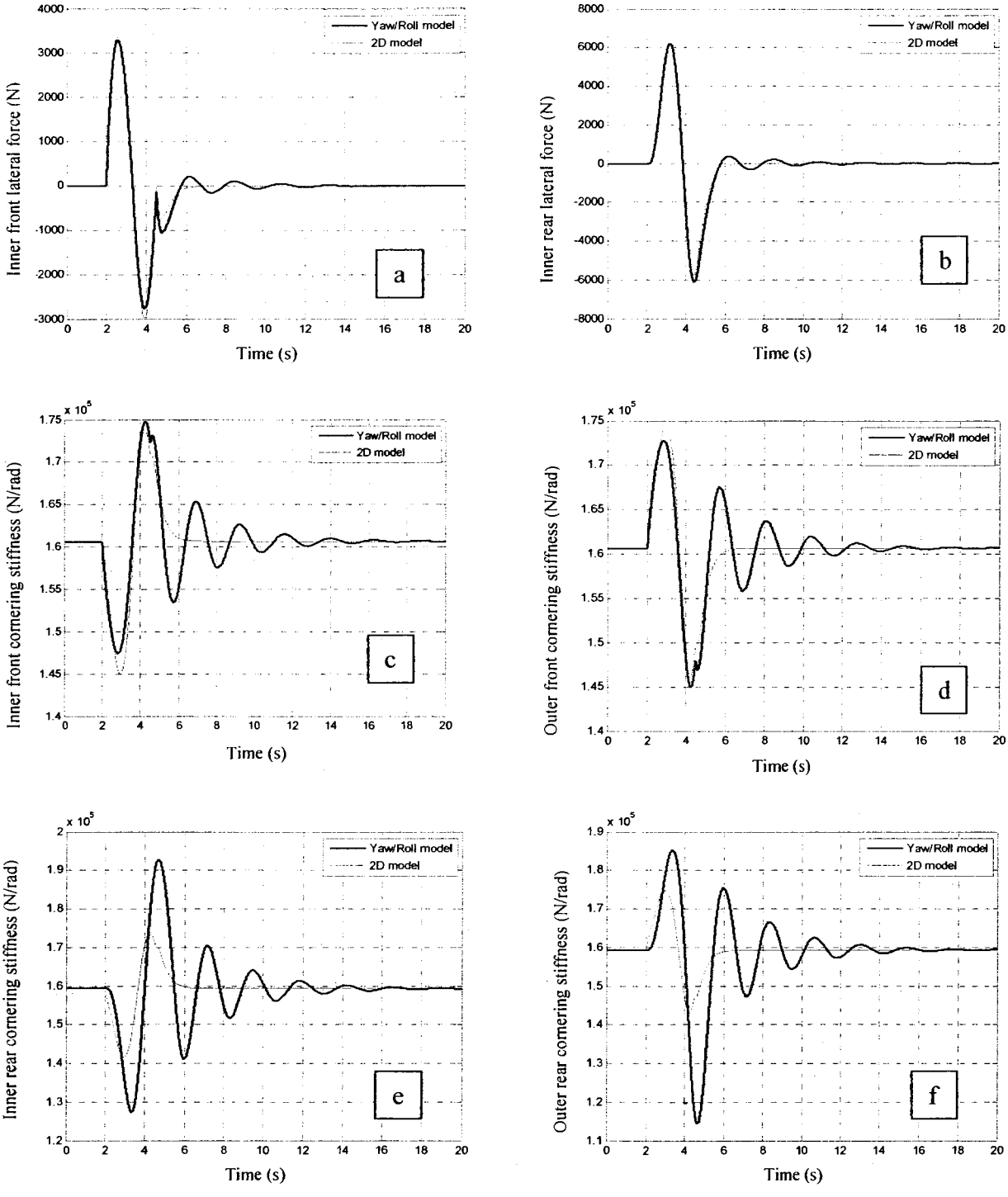

Figure 5.7: Comparisons of steering response characteristics of two- (2D) and three-(yaw/roll) dimensional handling dynamic models: (a) inner front wheel lateral force; (b) inner rear wheel lateral force; (c) inner front wheel cornering stiffness; (d) outer front cornering stiffness; (e) inner rear wheel cornering stiffness and (f) outer rear wheel cornering stiffness

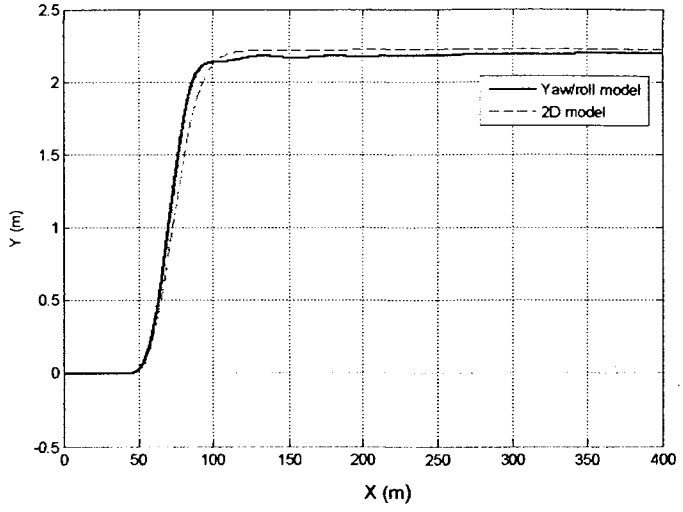

Figure 5.8: Comparison of the two- and three-dimensional models trajectory change to a sinusoidal steering input

5.3 Effect of Tire Inflation Pressure

From the reported measured data and the corresponding tire models presented in sections 2.2 and 4.3, it is apparent that vertical and cornering properties are strongly influenced by the tire inflation pressure. Consequently, the vertical and lateral tire forces that determine the vehicle handling properties are greatly affected by inflation pressure. This effect of inflation pressure on the urban bus handling dynamics is investigated under two types of steering inputs representing a steady-turning maneuver (Figure 5.1) and a path change type of maneuver (Figure 5.5).

5.3.1 SINUSOIDAL STEER INPUT

The effect of tire inflation pressure on the transient handling response characteristics is evaluated using the three-dimensional (yaw/roll) model subject to a 0.4 Hz single sinusoid steer input with 2^{o} amplitude (Figure 5.5), while the forward speed is kept constant at 20 m/s. The analyses are performed assuming half-full passenger load. The

tires inflation pressures are varied from 75 psi to 120 psi. The nonlinear cornering force properties of tires as a function of the inflation pressure, and instantaneous normal load and side slip angle are evaluated using the model described in section 4.3 and investigated in the three-dimensional model. The results are presented in the Figures 5.9 to 5.11 in terms of yaw rate, lateral acceleration, roll angle, roll rate, normal tire loads, a lateral force and side-slip angles in Figures 5.9 and 5.10.

The results show that the peak yaw rate and lateral acceleration responses increases with decreasing inflation pressure from 120 to 75 psi, as shown in Figure 5.9. This can be mostly attributed to reduced effective roll stiffness of the under-inflated tires. The increases in peak sprung and unsprung masses roll angles with decreasing pressure are clearly evident in Figures 5.9 (d) to 5.9 (f).

The peak sprung mass roll angle increases from 3.40^{o} to 4.25^{o} when the pressure is decreased from 120 to 75 psi. The peak rear axle roll angle is approximately three times that of the front axle, which is attributable to relatively greater load on the rear axle. The corresponding increases in unsprung masses roll angles are far more substantial. The lower effective roll stiffness of the under-inflated tires causes greater peak lateral load transfer, as seen in Figures 5.10 (a) and 5.10 (b). The lateral force developed by the softer tire, however, increases due to greater tire contact patch with ground, as seen in Figures 5.10 (e) and 5.10 (f). The peak side-slip angle responses of the tires however decrease only slightly, and cornering stiffness coefficient of the tires with low pressure tend to be higher, as seen in Figure 5.11. A Lower inflation pressure yields higher cornering stiffness under lower vertical load, as discussed in section 4.3. The inner and

outer tires on an axle exhibit nearly out-of-phase variations in the cornering stiffness predominantly occur at the excitation (steering) frequency.

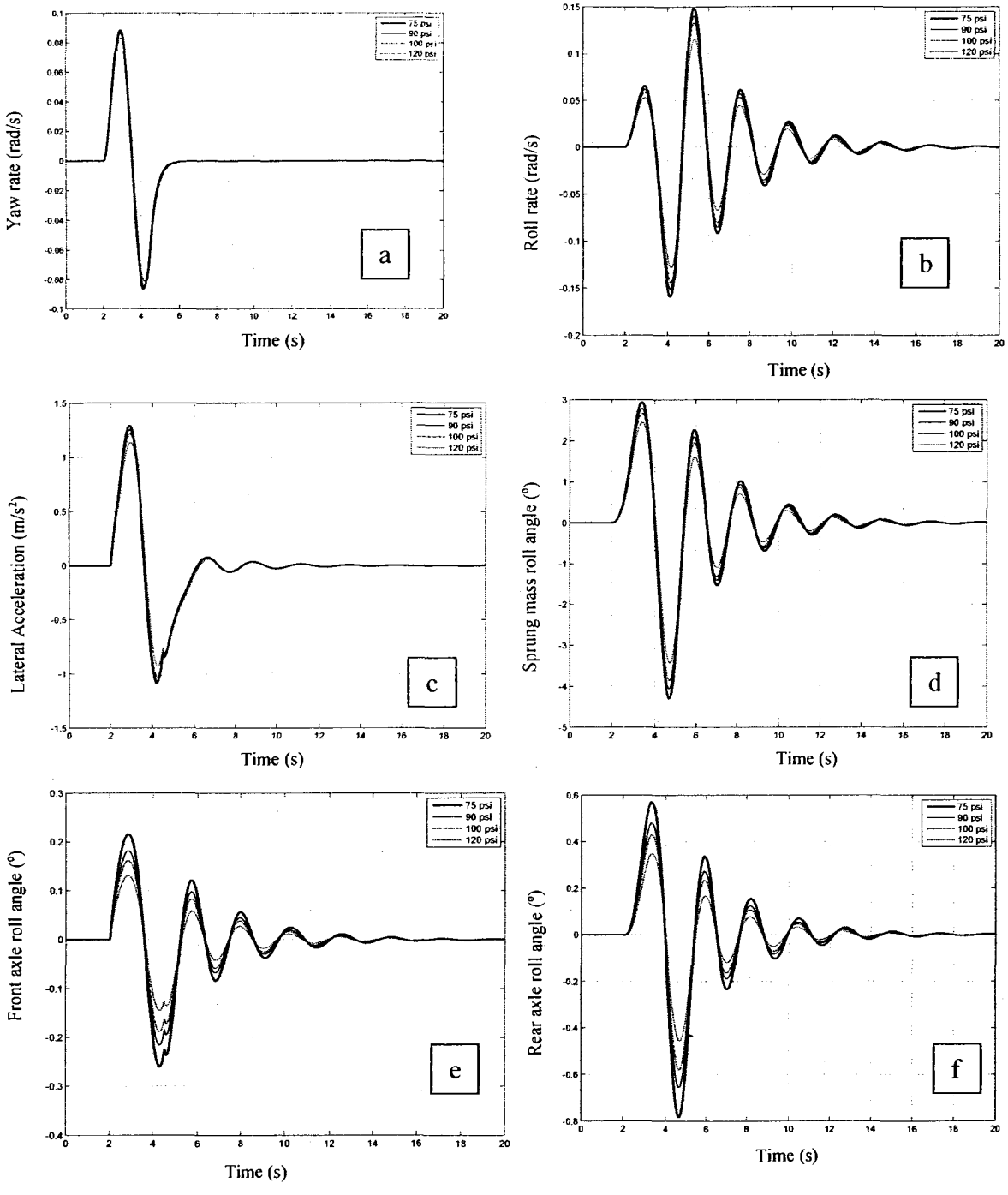

Figure 5.9: Effect of tire inflation pressure on the transient handling responses to a sinusoidal steer input: (a) yaw rate; (b) roll rate; (c) lateral acceleration; (d) sprung mass roll angle; (e) front-axle roll angle and (f) rear-axle roll angle.

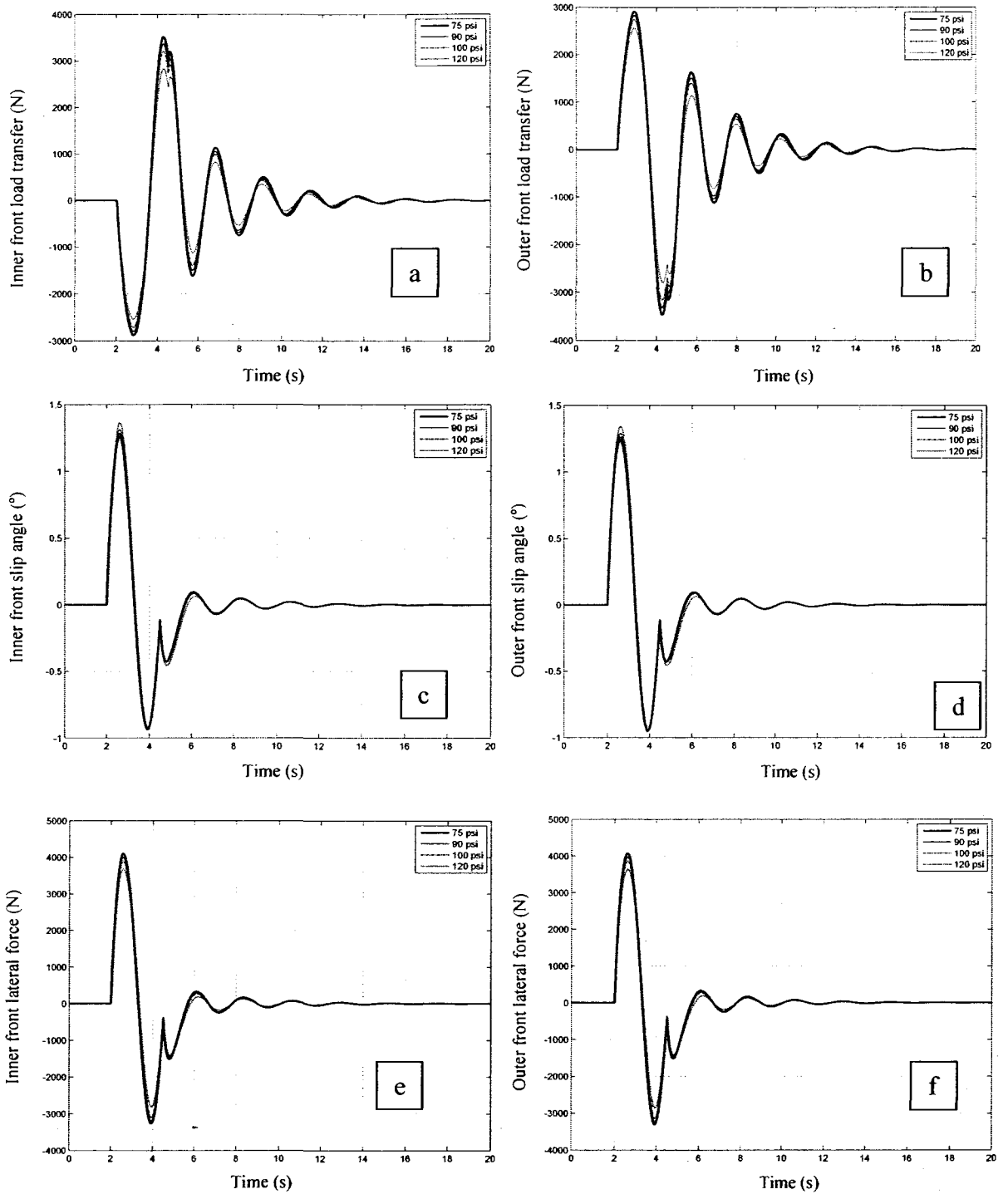

Figure 5.10: Effect of tire inflation pressure on the handling responses to a sinusoidal steer input: (a) inner-front wheel load transfer; (b) outer-front wheel load transfer; (c) inner-front wheel slip angle; (d) outer-front wheel slip angle; (e) inner-front wheel lateral force and (f) outer-front wheel lateral force.

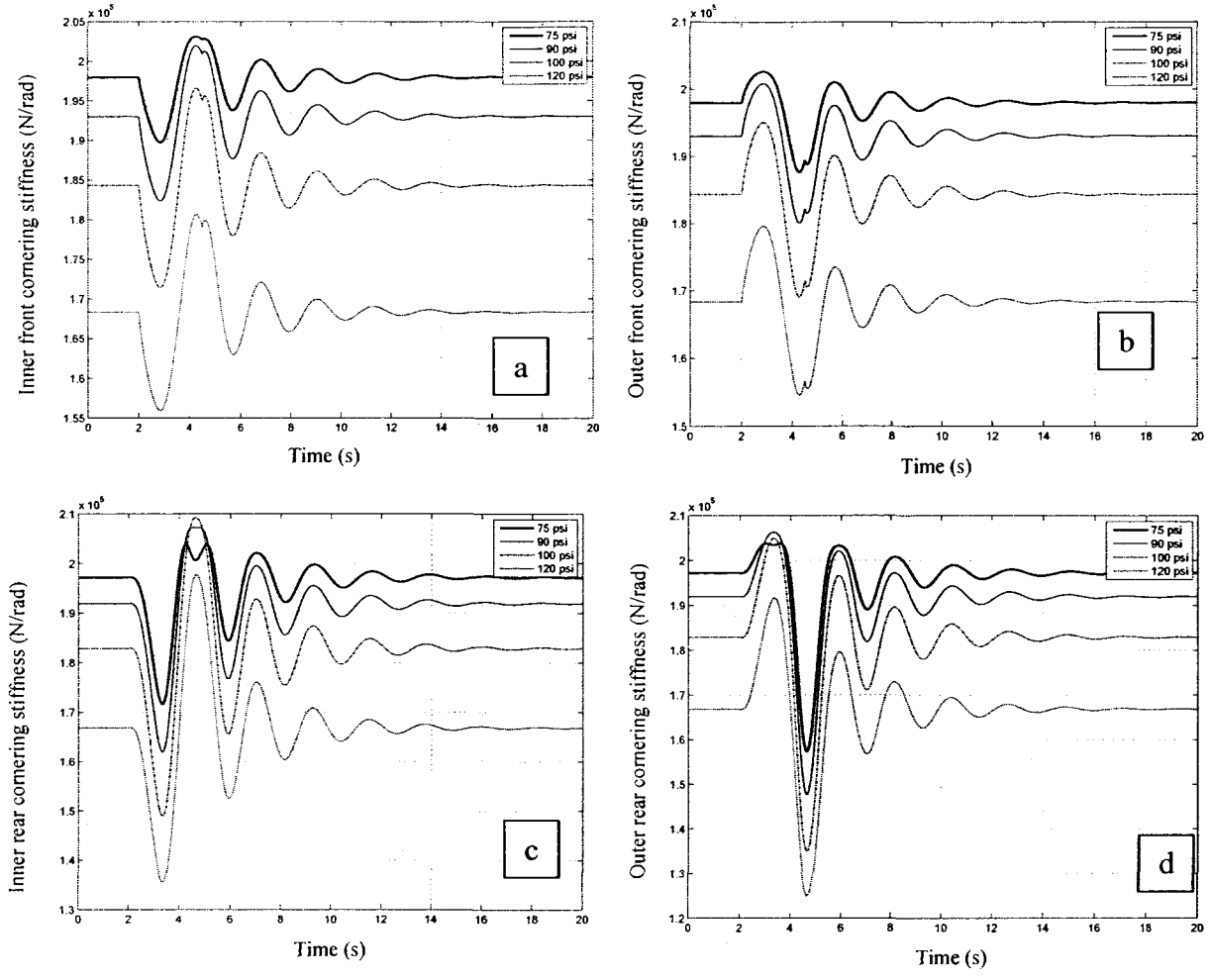

Figure 5.11: Effect of inflation pressure on cornering stiffness responses of the tires under a sinusoidal steer input: (a) inner-front wheel; (b) outer-front wheel (c) inner-rear wheel; and (d) outer-rear wheel.

5.3.2 STEP STEER INPUT

Figures 5.12 to 5.14 illustrate the transient responses to 2^{o} step steer input (Figure 5.1) as a function of inflation pressure. The results presented in Figure 5.12 show that the peak yaw rate and lateral acceleration tend to be higher for lower inflation pressure as observed under the sinusoidal steering input. The yaw rate and lateral acceleration responses, however, show negligible sensitivity to the inflation pressure. It can thus be concluded that a lower tire pressure affects the transient yaw rate and lateral acceleration

responses in an adverse manner, while steady-state responses are only minimally influenced by the inflation pressure. The reduced roll stiffness of under-inflated tires yields higher peak roll rate of the sprung mass, as shown in Figure 5.12 (b). Considerably higher magnitudes of peak as well as steady-state roll deflections of the sprung and sprung masses are also apparent for lower inflation pressures, as seen in Figures 5.12 (d) to 5.12 (f). Increased roll deflections under lower inflation pressures produce higher load transfer, as shown to Figures 5.13 (a) to 5.13 (b). While under-inflated tires generate slightly larger lateral tire force, as it was seen in responses to a sinusoidal steer, the corresponding side-slip angles are considerably smaller, as seen in Figures 5.13 (c) to 5.13 (d). The influence of tire pressure on the steady-state tire lateral force is very small, as it was observed for the yaw rate and lateral acceleration responses. The greater lateral force under a higher inflation pressure is associated with considerably higher side-slip angle but lower cornering stiffness, as shown in Figure 5.14. It should be noted that the steady-state vertical loads on the inner-front and rear tires would be less than their respective static load, which causes the cornering stiffness to increase at a lower inflation pressure. The load transferred to the outer tires increases their vertical loads and if this load is sufficiently high a higher inflation would yield higher cornering stiffness. The highest cornering stiffness occurs at 90 psi and 100 psi inflation pressures for the outer-front and rear tires, as shown in the Figure 5.14.

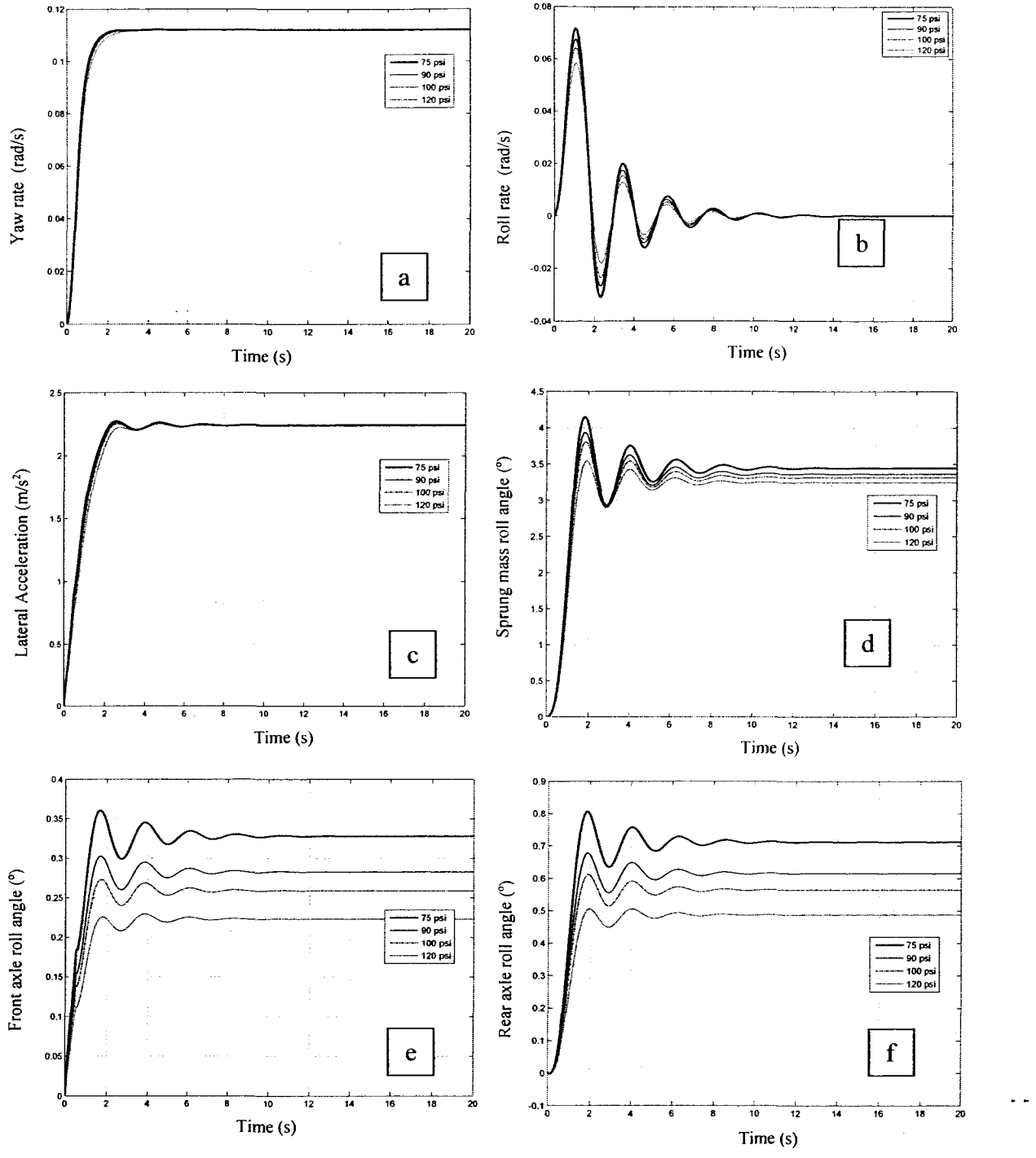

Figure 5.12: Effect of inflation pressure on the transient handling responses to a step steer input: (a) yaw rate; (b) roll rate; (c) lateral acceleration; (d) sprung mass roll angle; (e) front-axle roll angle; and (f) rear-axle roll angle.

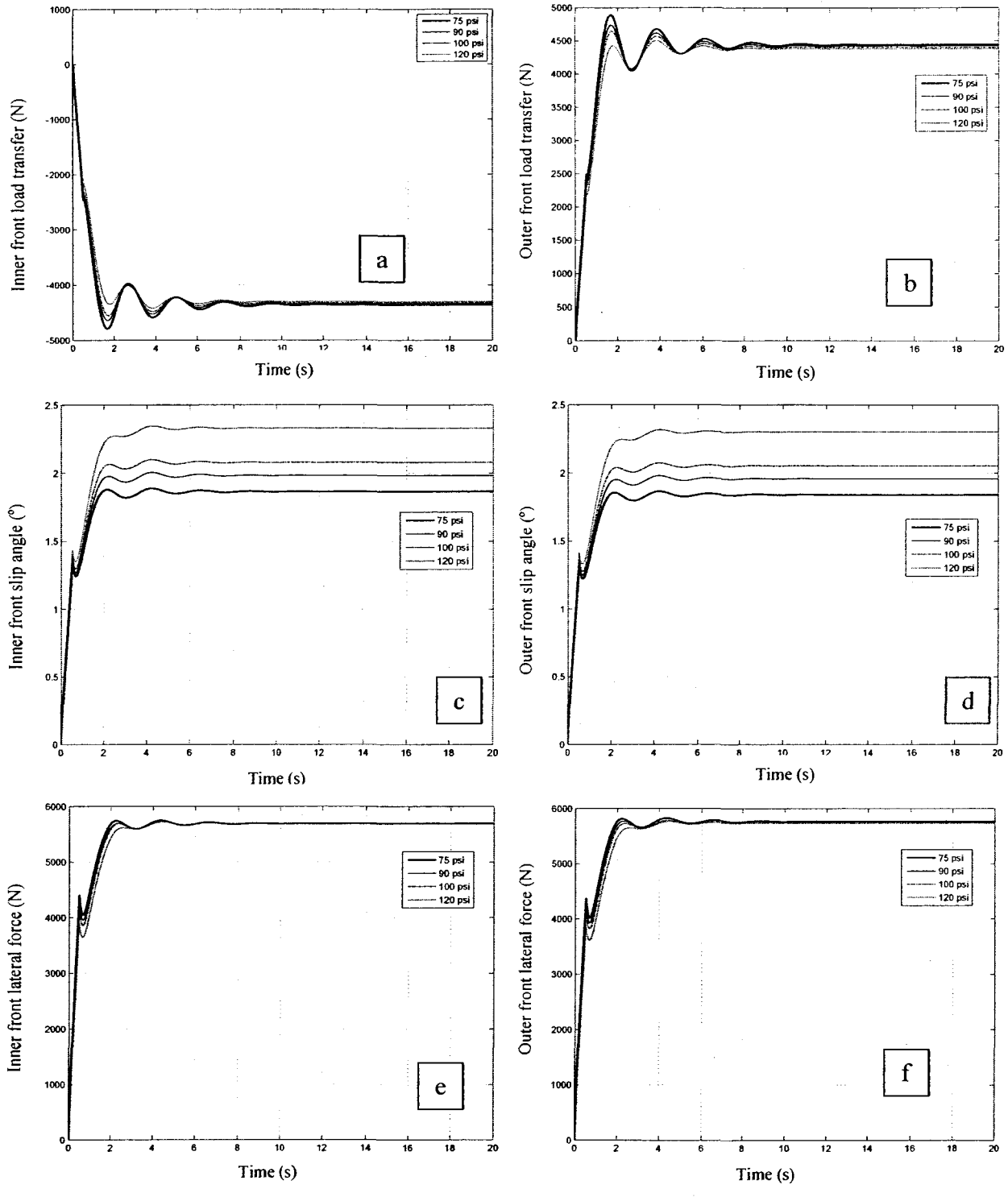

Figure 5.13: Effect of inflation pressure on the transient handling responses to a step steer input for the responses of: (a) inner-front wheel load transfer; (b) outer-front wheel load transfer; (c) inner-front wheel slip angle; (d) outer-front wheel slip angle; (e) inner-front wheel lateral force; and (f) outer-front wheel lateral force.

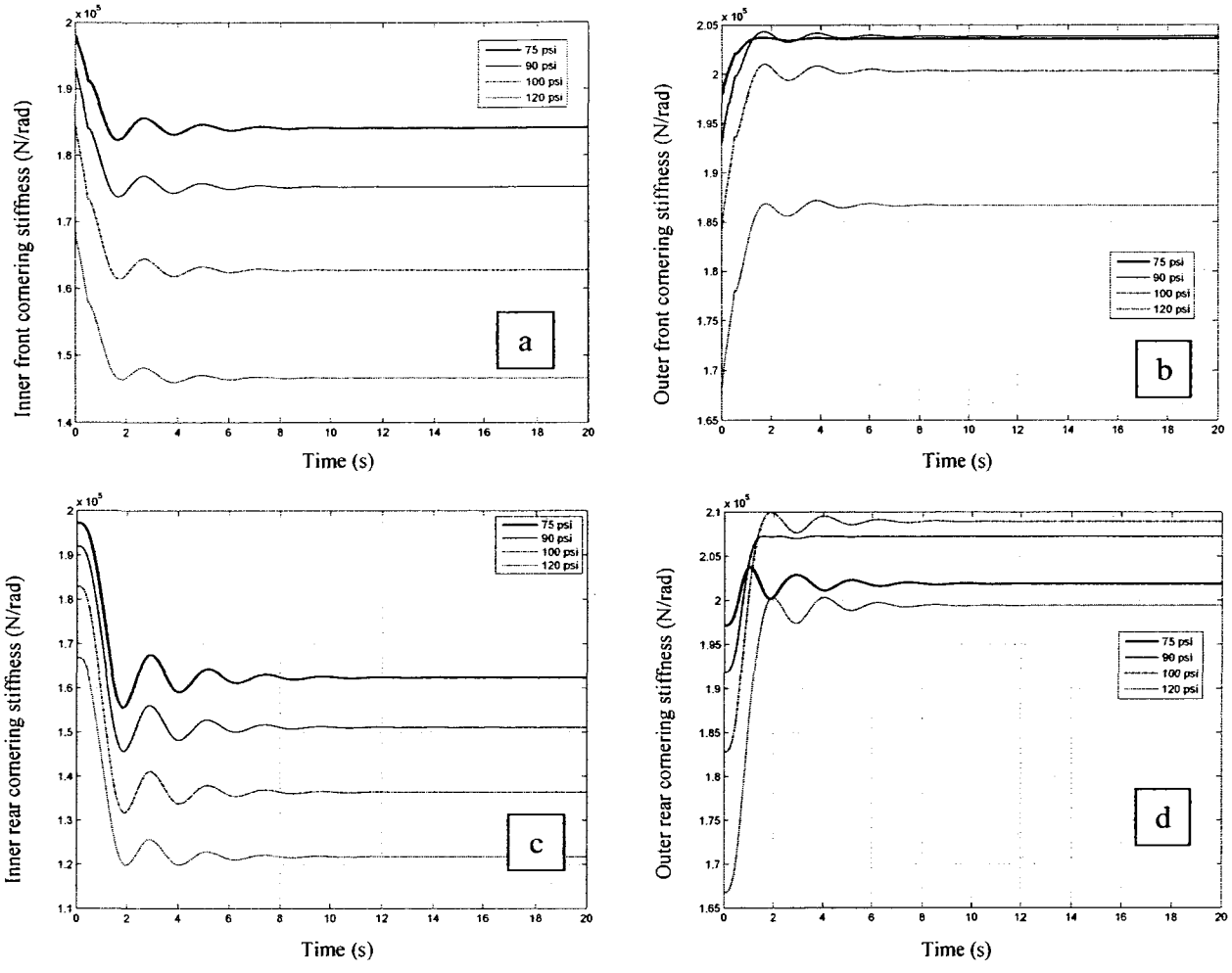

Figure 5.14: Effect of inflation pressure on the transient cornering stiffness response to a step steer input: (a) inner-front wheel cornering stiffness; (b) outer-front wheel cornering stiffness (c) inner-rear wheel cornering stiffness; and (d) outer-rear wheel cornering stiffness.

Figure 5.15 illustrate the influence of inflation pressure on the trajectory of the path followed by the vehicle mass center under a step-steer input and different tire pressures. The results show that a higher tire inflation pressure yields slightly larger turning radius. This is simply attributed to slightly larger yaw response attained with lower tire inflation, as seen in Figure 5.12.

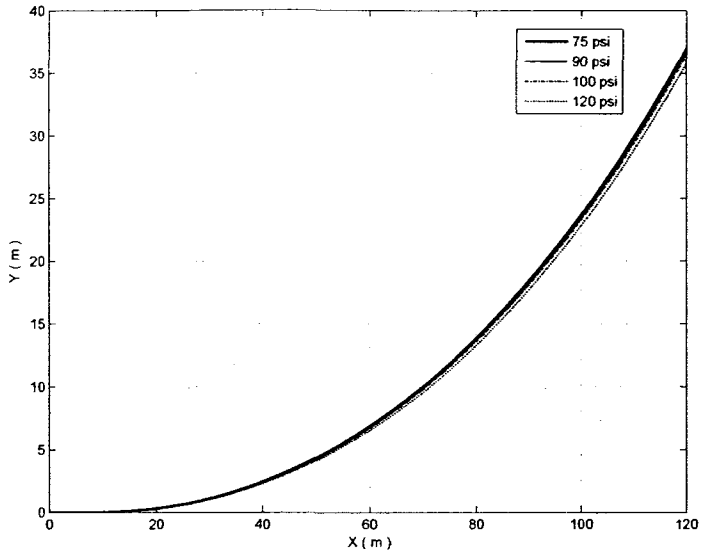

Figure 5.15: Effect of inflation pressure on bus trajectory due to step steer input.

5.4 Steady State Handling

The steady-state handling properties of a road vehicle are widely characterized by the understeer coefficient, K_{us}, the understeer coefficient relates to the distribution of normal load on the wheels and cornering properties of the tires [6]:

$$K_{us} = \left(\frac{W_f}{C_f} - \frac{W_r}{C_r}\right) \tag{5.3}$$

Where C_f and C_r are the effective cornering stiffnesses of the front and rear axle tires, respectively, and W_f and W_r are the vertical load supported by the front and rear axle tires, respectively. Apart from the normal load and cornering stiffness, the steady-state handling and the understeer coefficient are strongly influenced by a number of operating parameters such as speed, tire inflation pressure and acceleration/braking. It should be noted that the K_{us} in Eq. (5.3) is derived assuming linear cornering properties of tires, which can be considered valid for side-slip angles up to 3°. The steady-state handling

properties of road-vehicles are often derived assuming parallel front wheels steering angles, such that:

$$\delta_{av} = \frac{L}{R} + k_{us}\frac{a_y}{g} \tag{5.4}$$

Where δ_{av} is the average front wheels steering angle, L is the vehicle wheel base, R is turning radius and a_y is vehicle lateral acceleration. The average front wheels steering angle can also be related to average side-slip angles of the inside-and outside-tires, as:

$$\delta_{fav} = \frac{L}{R} + [\overline{\alpha_f} - \overline{\alpha_r}] \tag{5.5}$$

Where $\overline{\alpha_f}$ and $\overline{\alpha_r}$ are average side-slip angles of the inside and outside tires of the front and rear wheels, respectively. The understeer coefficient may thus be estimated from the changes in steer and slip angles with respect to the lateral acceleration, such that:

$$k_{us} = g\frac{d\delta_{fav}}{da_y} = g\frac{d(\alpha_{fav} - \alpha_{rav})}{da_y} \tag{5.6}$$

The above formulation can provide a direct estimate of K_{us} under different tire inflation pressure and operating conditions. Furthermore, estimates of lateral acceration and turning radius nay obtained from: $a_y = V_x^2/R$; and $R = V_x/\Omega$.

5.4.1 EFFECT OF INFLATION PRESSURE ON STEADY STATE HANDLING

The influence of variations in the inflation pressure on the understeer coefficient is investigated over a wide range of forward speeds and operating loads. At low and medium speeds the vehicle generally exhibits understeer behavior, where the K_{us} may lie in the order of 0.1°. Figures 5.16 to 5.18 illustrate variations in K_{us} with forward speed ranging from 4 to 23 m/s under different tire inflation pressures for three different vehicle loads representing none, half-full and full passengers load, respectively.

A road vehicle may experience oversteer tendencies at higher speeds. The observed variations in K_{us} with vehicle speed are typical for heavy vehicles [43]. The results show that a higher inflation pressure produces slightly more understeer tendency at low and medium forward speeds less than 18 m/s (65km/h). A lower inflation pressure could yield greater oversteer tendency at a higher speed.

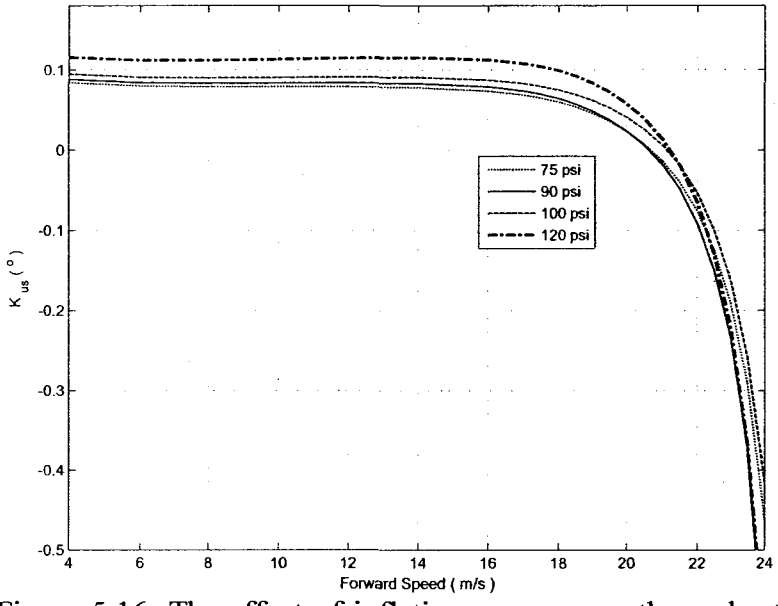

Figure 5.16: The effect of inflation pressure on the understeer coefficient with forward speed (zero passenger load).

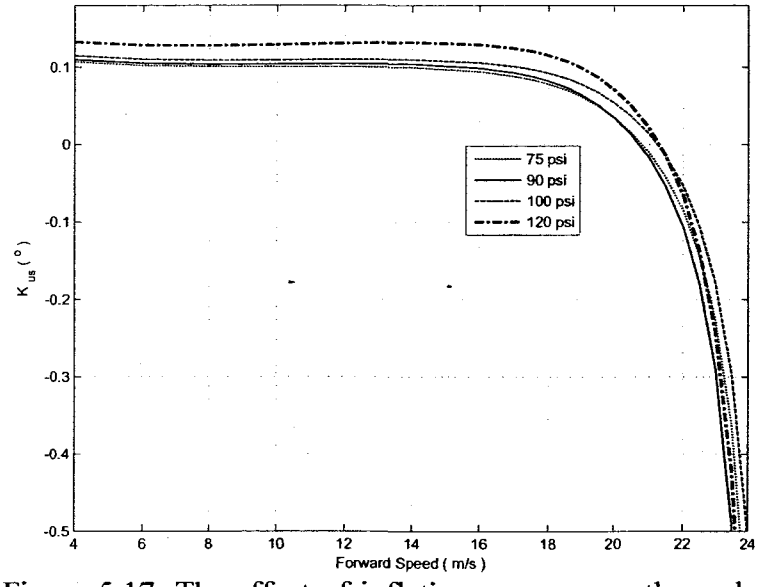

Figure 5.17: The effect of inflation pressure on the understeer coefficient with forward speed (half-full passenger load).

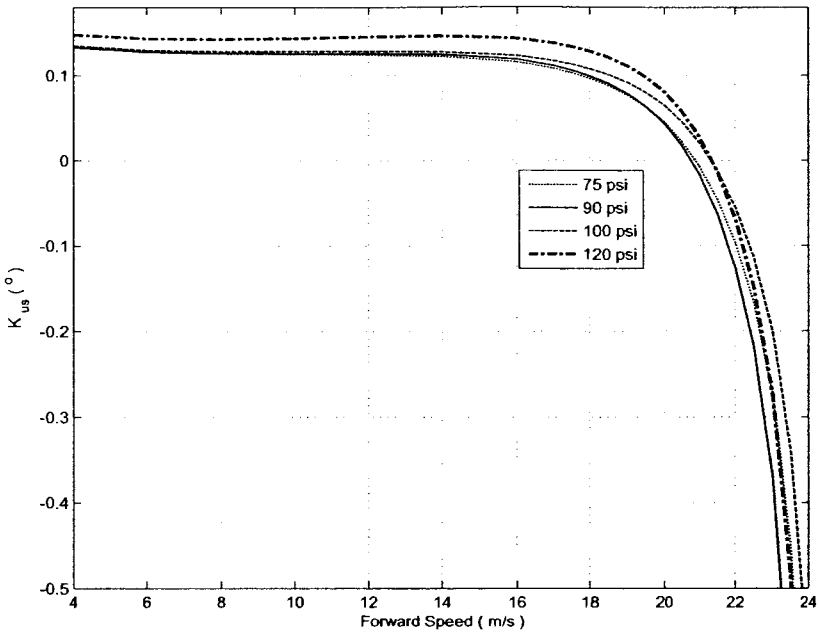

Figure 5.18: The effect of inflation pressure on the understeer coefficient with forward speed (full passenger load).

5.4.2 EFFECT OF LOADING

The results presented in Figures 5.19 to 5.22 further suggest greater understeer tendency with increasing load. This is attributable to larger rear axle load and higher cornering stiffness of rear tires under half-full and full passenger load conditions. The variations in passenger load, however, cause complex variations in the tire cornering properties and vehicle handling properties. The variations in number of passengers tend to vary coordinates of center of gravity, vertical load distribution, air suspension stiffness, tire vertical and cornering stiffness, and the yaw and roll mass moment of inertia in a highly complex manner, which would directly influence the vehicle handling dynamics. Further analyses are thus performed under three typical loading conditions, assuming uniform distribution of passengers in the bus. Owing to the suspension height valves, the vertical distances between the mass centers of the axles and the bus body are considered

to remain constant, while decrease in unsprung masses c.g heights is estimated from the force-deflection properties of tires.

Figures 5.19 to 5.22 illustrate the effect of loading condition on the vehicle understeer coefficient under different speeds ranging from 4 to 24 m/s, and different inflation pressures (75,90,100 and 120 psi). The results show that the understeer coefficient at lower speeds is proportional to the load, irrespective of the inflation pressure. At higher speeds the vehicle exhibit oversteer tendency and a higher load yields higher oversteer tendency.

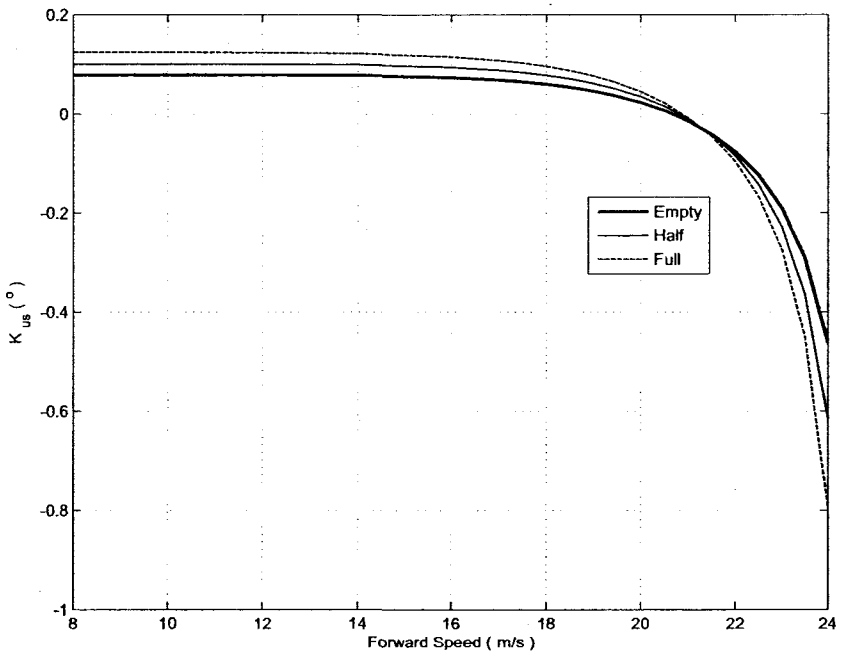

Figure 5.19: The effect of vehicle load on the understeer coefficient at different speeds (tire pressure: 75 psi).

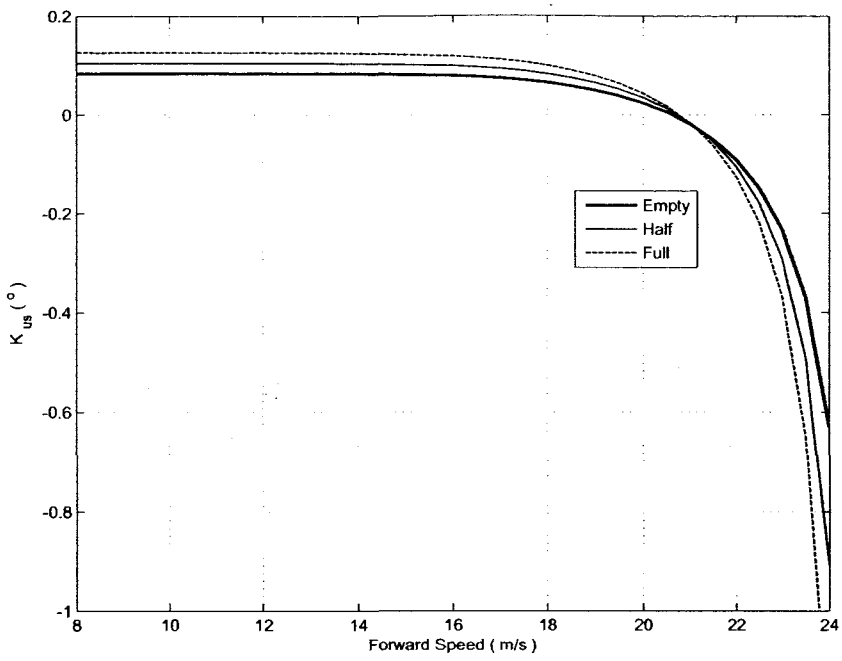

Figure 5.20: The effect of vehicle load on the understeer coefficient at different speeds (tire pressure: 90 psi)

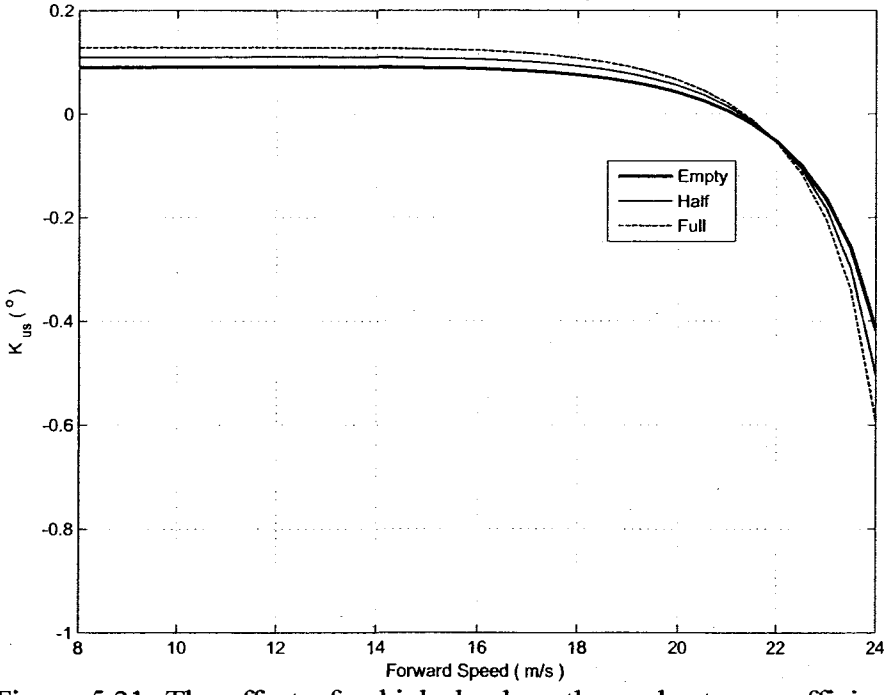

Figure 5.21: The effect of vehicle load on the understeer coefficient at different speeds (tire pressure: 100 psi).

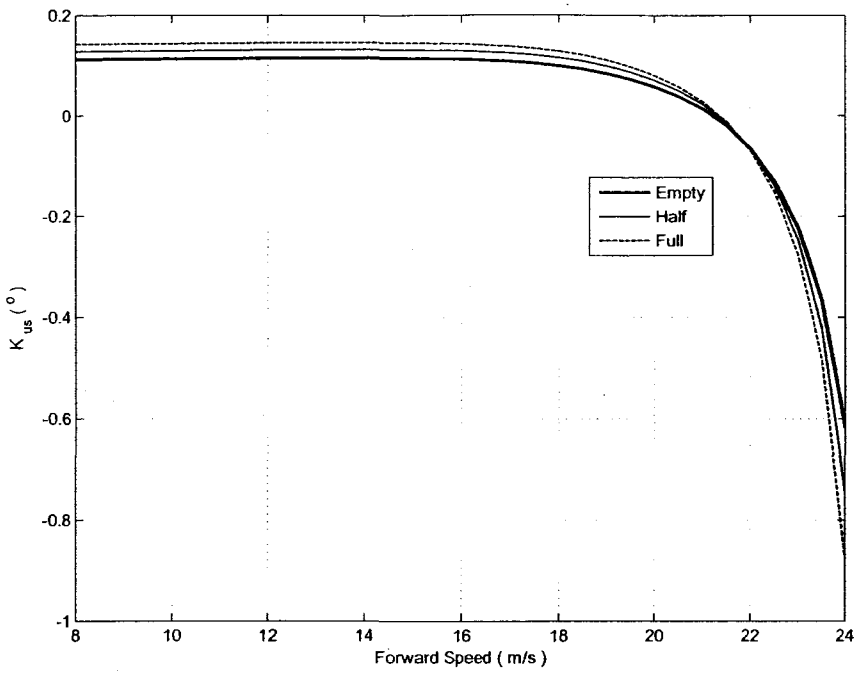

Figure 5.22: The effect of vehicle load on the understeer coefficient at different speeds (tire pressure: 120 psi).

5.5 Summary

In this chapter, transient and steady-steady handling responses of the two- and three-dimensional models are compared under two different types of steering inputs. The influence of tire inflation pressure on the transient and steady-state handling responses of the respective steering inputs is investigated. Furthermore, the influences of tire inflation pressure and passenger load on the understeer and oversteer tendencies of the vehicle at different speeds are also investigated.

CHAPTER 6

Conclusions and Future Work

6.1 Major Contributions

The present dissertation research presents an analytical framework to determine the effect of inflation pressure on the ride, pavement loading and handling properties of the vehicle. A few studies have investigated the effect of the inflation pressure on the ride dynamics wheel loads experimentally in the context of central tire inflation system. An analytical study on the effects of tire pressure on ride and pavement loading could not be found in the literature. Moreover, the effects of tire pressure on the steady-state and transient handling properties have not been addressed in the reported studies, which is most likely attributed to lack of cornering force model of tire as a function of the inflation pressure. The cornering force model of the tire as a function of the inflation pressure is thus considered the major contribution of this work together with the analytical ride and handling models that permit the study of effects of tire pressure. It needs to be emphasized that the proposed tire model represents a preliminary effort and for more tire data are desirable to develop cornering force tire model.

6.2 Conclusions

This dissertation work presents analytical ride and handling dynamic models of an urban bus and analyses on the influences of variations in tire inflation pressure passenger loads on the dynamic performance of urban bus, particularly the ride vibration, pavement

loading and the handling characteristics, my conclusions drawn from the study are summarized below:

- Reducing tire pressure yields lower vertical stiffness of tires, and a greater contact between the tire and the road.
- A higher tire inflation pressure strongly affects the vehicle ride performance and yields greater magnitudes of vibration transmitted to the passengers and the driver, and a higher dynamic tire loads transmitted to the pavement that may lead to rapid pavement fatigue.
- The peak cornering stiffness occurs at a lower vertical load as the inflation pressures decreases.
- Low inflation pressure yields higher cornering stiffness at lower vertical loads, while higher vertical load yields higher cornering stiffness at higher inflation pressures.
- The peak lateral force of (F_y vs α) response that obtained at a certain vertical tire load and inflation pressure is not influenced by tire pressure and is only function of the vertical load.
- Shape factor E in Magic Formula is strongly dependent on the tire inflation pressure and vertical load and exhibit almost linear relation with the vertical load, the value of E decreases as load or tire pressure increases.
- *Magic Tire Formula* is efficient to compute the lateral tire force as a function of side-slip angle, vertical load and inflation pressure and show excellent correlation with measured data.

- The simplified two-dimensional handling model can yield reasonably good predictions of the steady-state handling properties of the vehicle. A three-dimensional model, however, is essential for analyses of transient handling responses of the vehicle, since a softer tire can yield greater sprung and unsprung mass roll.
- Urban buses often operate with very light passengers load, particularly during off-peak hours. The light passengers load coupled with relatively high nominal tire pressures yield considerably higher magnitudes of sprung mass vibration and thus poor ride quality.
- The dynamic tire loads transmitted to the pavement are significantly higher with higher tire pressure.
- The higher tire pressure also yields higher magnitudes of dynamic forces transmitted to the chassis structural components fatigue.
- The ride quality, pavement loading and chassis loads are further influenced by the road roughness in an adverse manner.
- Lower tire inflation pressure reduces the magnitudes of transmitted vibration through attenuation by the softer tire.
- A lower inflation pressure also reduces the dynamic tire loads, which are distributed over a larger contact area. A lower inflation pressure under light passengers load is thus highly beneficial in enhancing the ride and pavement loading performance of the vehicle.
- An increase in forward speed, in-general yields greater oversteer tendency for heavy vehicles.

- Low inflation pressure causes higher yaw and roll rates, and lateral acceleration of the sprung mass and greater roll deflections of the unsprung masses leading to higher load transfer.
- A higher inflation pressure increases the understeer coefficient at low and medium forward speeds, but yields more oversteer tendency at higher speeds.

6.3 Future Work

This dissertation research represents a preliminary effort to characterize the role of tire pressure in context of vehicle handling properties. For more efforts are desirable to fully characterize the cornering properties of tires as a function of the inflation pressure. More specifically, it is suggested to undertake following studies to enhance the model quality and develop a more effective central tire inflation system.

- Incorporate a distributed contact tire model instead of the point-contact in order to achieve more accurate description of the contact forces at the pavement surface and more reliable ride responses.
- A control algorithm needs to be developed on the basis of the passenger load so as to operate the tires under the optimum inflation pressure.
- Further studies are needed to determine the optimal tire pressure as a function of speed and road roughness conditions. These will allow the design of central tire inflation system for urban buses.
- Experimental studies should be undertaken to characterize cornering properties of tires as a function of pressure, load and side slip angle.

- Further efforts are desirable in developing reliable tire cornering and braking forces models as a function of inflation pressure

References

1 Rakheja, S. and Yang, X., "Urban Bus Optimal Passive Suspension Study, Phase I: Development of Optimal Suspension Characteristics Through Systematic Study of Reduced Model", Prepared By Concave Research Center, Concordia University, 1999.

2 Hewson, P., "Method for Estimating Tire Cornering Stiffness from Basic Tire Information", Journal of Automobile Engineering, Volume 219, Number 12, 2005.

3 Rhyne, T. B., "Development of A Vertical Stiffness Relationship For Belted Radial Tires", Tire Science and Technology, Vol. 33, 2005.

4 Collier, B. L. and Warchol, J. T., "The Effect of Inflation Pressure on Bias-Belted and Radial Tire Performance." SAE Technical Paper 800087, 1980.

5 Rakheja, S., Wang, Z. and Ahmed, A. K. W, "Enhancement of Road- and Driver-Friendliness of Urban Bus through Optimal Suspension Damping", Urban Bus Optimal Passive Suspension Study, Phase II, Concave Research Center, Concordia University, 2000.

6 Wong, J.Y, "Theory of Ground Vehicles", Third Edition, John Wiley & Sons, Inc, New York, 2001.

7 Eisenmann, J., "Dynamic Wheel Load Fluctuations - Road Stress", Strasse und Autobahn, 4: 127-128, 1975.

8 Sweatman, P.F., "A Study of Dynamic Wheel Forces in Axle Group Suspensions for Heavy Vehicles", ARRB Special Report, 127, 1987.

9 Rakheja, S., Yang, X. and Stiharu, I., "Urban Bus Optimal Passive Suspension Study", CONCAVE Research Centre, Transport Canada, TP 13787E, 2001.

10 Rajamani, R., "Vehicle Dynamics and Control", Springer Science + Business Media, Inc, New York, 2006.

11 Cebon, D., "Interaction between Heavy Vehicles and Roads." SAE Publication, SP–951, 1993.

12 El-Gindy, M., "An Overview of Performance Measures For Heavy Commercial Vehicles in North America", Int. J. of Vehicle Design, Vol. 16, 1995.

13 Saran, V.H. and Goel, V. K., "Rolling Dynamic Stiffness and Damping Characteristics of Small-Sized Pneumatic Tires", Journal of Automobile Engineering, Volume 214, Number 3, 2000.

14 Kao, B. G, "Tire Vibration Modes and Tire Stiffness", Tire Science and Technology, Vol. 30, No. 3, 2002.

15 Jianmin, G., Gall, R. and Zuomin, W., "Dynamic Damping And Stiffness Characteristics of The Rolling Tire", Tire Science and Technology, Vol. 29, No. 4, 2001.

16 Kasprzak, E. M., Lewis, K. E. and Milliken, D. L., "Inflation Pressure Effect in the Nondimensional Tire Model", SAE paper No. 2006-01-3607, 2006.

17 Kasprzak, E. M., Lewis, K. E. and Milliken, D. L., "Tire Asymmetries and Pressure Variations in the Radt/Milliken Nondimensional Tire Model", SAE paper No. 2006-01-1968, 2006.

18 Schmeitz, A.J.C., Besselink, I.J.M., Hoogh, J. D. and Nijmeijer, H., "Extending The Magic Formula and SWIFT Tire Models for Inflation Pressure Changes", VDI BERICHTE, Vol. 1912, 2005.

19 Nicholas, D. Smith, "Understanding Parameters Influencing Tire Modeling", Department of Mechanical Engineering, Colorado State University, Formula SAE Platform, 2004.

20 Brach, R. M., Brach, R. M., "Modeling Combined Braking and Steering Tire Forces", SAE Technical Paper No. 2000-01-0357, 2000.

21 Pacejka, H. B. and Bakker, E., "The Magic Formula Tire Model", Vehicle System Dynamics, Vol.21, Supplement, Tire Models for Vehicle Dynamics Analysis, 1993.

22 Stone, M.R., and Demetriou, M.A., "Modeling and Simulation of Vehicle Ride and Handling Performance", Proceedings of the 15th IEEE International Symposium on Intelligent Control, 2000.

23 Taehyun Shim, Yi Zhang, "Effects of Transient Powertrain Shift Dynamics on Vehicle Handling", International Journal of Vehicle Design, Vol. 40, 2006.

24 Jang, B. and Karnopp, D., "Simulation of Vehicle and Power Steering Dynamics Using Tire Model Parameters Matched to Whole Vehicle Experimental Results",

Vehicle System Dynamics, Vol. 33, 2000.

25 Lin, W. K., Chen, Y. C., Kulakowski, B. T. and Streit, D. A., "Dynamic Wheel/Pavement Force Sensitivity to Variations in Heavy Vehicle Parameters, Speed and Road Roughness", Heavy Vehicle Systems-Special Series of Intl Journal of Vehicle Design, Vol. 1, No. 2, 1994.

26 Cantieni, R., Krebs, W. and Heywood, R., "Dynamic Interaction between Vehicles and Iinfrastructure Experiment (DIVINE) : Technical Report", Organization for Economic Co-operation and Development.

27 Collop, A. and Cebon, D., "Effects of 'Road Friendly' Suspensions on Long-Term Flexible Pavement Performance", Proceedings of the Institution of Mechanical Engineers, Part C, Journal of Mechanical Engineering Science, Vol. 211, Issue 6, 1997.

28 Anon, A., "Dynamic Loading of Pavement." Road Transport Research, OECD, Paris, 1992.

29 Ahmed, A. K. W., "Ground Transportation System", Encyclopedia of Vibration, Elsevier Science & Technology Books, 2001.

30 Fancher, P. S., "Descriptive Parameters Used in Analyzing the Braking and Handling of Heavy Trucks - Measurements of the Longitudinal and Lateral Traction Properties of Truck Tires", Volume 3, Data volume III (notebook III), Final report, Transportation Research Institute (UMTRI), 1981.

31 Wong, J.Y. and El-Gindy, M., "Technical Report of Vehicle Weights and

Dimensions Study", Vol. 16, Road and Transportation Association of Canada (RTAC), 1986.

32 Tsunashima, H. and Kaneko, T., "Performance Analysis of Lateral Guidance System for Dual Mode Truck", IEEE Conference on Intelligent Transportation Systems, 1997.

33 Wu, D. H., "A Theoretical Study of the Yaw/Roll Motions of a Multiple Steering Articulated Vehicle", Proceedings of the I MECH E Part D Journal of Automobile Engineering, Volume 215, Number 12, 2001.

34 Dixon, J. C., "Tires, Suspension and Handling", Cambridge University Press, 1991.

35 Afework, Y., "An Analytical and Experimental Study of Driver-Seat-Suspension Systems", Master Thesis, Concordia University, 1991.

36 Rao, K., Kumar, R., Mukhopadhyay, R. and Misra,V., "A Study of Relationship between Magic Formula Coefficients and Tyre Design Attributes through Finite Element Analysis", Vehicle Systems Dynamics, Vol. 44, 2006.

37 Zhu, Q. and Ishitobi, M., "Chaotic Vibration of a Nonlinear Full-Vehicle Model", International Journal of Solids and Structures, 2006.

38 Turkay, S. and Akcay, H., "A Study of Random Vibration Characteristics of the Quarter-Car Model", Journal of Sound and Vibration, 2005.

39 Lewis, F.L., Campos, J. and Davis, L., "Active Suspension Control of Ground

Vehicle based on a Full-Vehicle Model", Proceedings of the 2000 American Control Conference. ACC (IEEE Cat. No.00CH36334), Vol. 6, 2000.

40 Shim, T. and Ghike, C., "Understanding the Limitations of Different Vehicle Models for Roll Dynamics Studies", Vehicle System Dynamics, V 45, n 3, 2007.

41 "Central Tire Inflation Systems: Managing the Vehicle to Surface", SP-1061, Society of Automotive Engineers,1995.

42 Rakheja, S. and Z. Wang "Feasibility Assessment of a Central Tire Inflation Systeem (CTIS) For Urban Buses", Technical Report, CONCAVE Research Centre 2006.

43 Gillespie,T. D., "Fundamentals of Vehicle Dynamics", Society of Automotive Engineers (SAE) ,1992.